Graduate School ETD Form 9
(Revised 12/07)

PURDUE UNIVERSITY
GRADUATE SCHOOL
Thesis/Dissertation Acceptance

This is to certify that the thesis/dissertation prepared

By Jeffrey David Carvell

Entitled
Induced Magnetoelectric Coupling at a Ferroelectric-Ferromagnetic Interface

For the degree of Doctor of Philosophy

Is approved by the final examining committee:

Ruihua Cheng
Chair

Jiangping Hu

Yogesh Joglekar

Ricardo Decca

Horia Petrache

To the best of my knowledge and as understood by the student in the *Research Integrity and Copyright Disclaimer (Graduate School Form 20)*, this thesis/dissertation adheres to the provisions of Purdue University's "Policy on Integrity in Research" and the use of copyrighted material.

Approved by Major Professor(s): Ruihua Cheng

Approved by: Ricardo Decca 03/26/2013
Head of the Graduate Program Date

INDUCED MAGNETOELECTRIC COUPLING AT A FERROELECTRIC-FERROMAGNETIC INTERFACE

A Dissertation

Submitted to the Faculty

of

Purdue University

by

Jeffrey Carvell

In Partial Fulfillment of the

Requirements for the Degree

of

Doctor of Philosophy

May 2013

Purdue University

Indianapolis, Indiana

This work is dedicated to my parents, Debbie and Steve, who have given me the opportunity of this education and for their support, and to my family, Carly and our son James, who are with me always and ready to support me when needed.

ACKNOWLEDGEMENTS

I would like to show my gratitude to everybody who contributed and made this thesis and work possible. First of all I would like to thank my advisor, Dr. Ruihua Cheng, for her willingness to accept me as her PhD student and for her guidance, advice, warm encouragement, patience and frequent discussions during my studies. I learned many things from you, both scientifically and non-scientifically. You paid attention not only to my research work, but also to some problems that had nothing to do with my work and you were also concerned with my future career. I am extraordinarily fortunate to have an advisor like you. Thanks for everything Dr. Cheng, I will never forget it.

I would like to express my sincere appreciation to my committee members at IUPUI, Dr. Ricardo Decca, Dr. Yogesh Joglekar, and Dr. Horia Petrache for pushing me to be the best I can be. Your brilliant input, corrections, questions, and suggestions helped me to accelerate my research and produce the better results and analysis.

Dr. Jiangping Hu, my Purdue faculty committee member, I would like to thank you for helping out and participating on my committee. Thank you also for agreeing to video conference my defense in order to accommodate the schedule for this semester.

Thank you Dr. Marvin Kemple for your useful discussions about both physics and non-physics topics, helping me keep my sanity, and for proofreading all of my publications.

Thank you to Dr. Andy Gavrin for his help with explaining some of his lab equipment, for his useful discussions and points about my research, and for all your help in looking for future work.

I greatly appreciate everything Dr. Brian Woodahl and Dr. John Ross have done for me in regards to my teaching experience. You both helped me gain valuable experience and helped shape my teaching style going forward.

Thank you to all the people who have aided in my research through my time at IUPUI. Thanks to all of my fellow graduate students, especially Clint Thompson, Merell Johnson, Chris Jamell, and Prashant Srinivasan.

A special thank you to Dr. H. Marshall Dixon, who lent not only an ear to talk to about physics, but his home for over a year of my studies. I value the time I lived with you, and the conversations we had late at night and over dinner.

Thanks also to all the office staff in the IUPUI Department of Physics who have helped with forms, travel, and day-to-day operations. Thank you very much Juli Sutchaleo, Kimberly Wright, and Kelly Miholic.

My deep thanks are dedicated to my beloved family: to my parents and sister for their steady support and prayers. And to my grandparents, who helped make all of this possible with their support. Last but most beloved, I would like to thank my fiancé Carly Guest and our son, James, for always understanding me and sharing life together in happiness and sadness. Thank you for your love and everything that comes to my life with you. Being with you really makes my life more complete.

TABLE OF CONTENTS

Page

LIST OF FIGURES

Figure Page

Figure Page

Figure Page

Figure Page

Figure Page

Figure Page

Figure Page

Figure Page

Figure Page

Figure Page

LIST OF ABBREVIATIONS

AFM	Antiferromagnetic
AWFG	Arbitrary Waveform Generator
DOS	Density of states
FIM	Ferrimagnetic
FM	Ferromagnetic
LSMO	Lanthanum, Strontium, Manganese Oxide
MAE	Magnetocrystalline Anisotropy Energy
ME	Magnetoelectric Effect
MH	Magnetization versus applied magnetic field
ML	Monolayer
MOSFET	Metal–oxide–semiconductor field-effect transistor
MRAM	Magnetoresistive random-access memory
PE	Polarization versus applied electric field
PM	Paramagnetic
PVDF	Polyvinylidene Fluoride
PZT	Lead Zirconium Titanate, $Pb[Zr_xTi_{1-x}]O_3$
STT	Spin torque transfer
TrFE	trifluoroethylene

ABSTRACT

Carvell, Jeffrey David. Ph.D., Purdue University, May 2013. Induced Magnetoelectric Coupling at a Ferroelectric-Ferromagnetic Interface. Major Professor: Ruihua Cheng.

Preparation and characterization of multiferroic materials in which ferroelectricity and ferromagnetism coexist would be a milestone for functionalized materials and devices. First, electric properties of polyvinylidene (PVDF) films fabricated using the Langmuir-Schaefer method have been studied. Films of different thickness were deposited on silicon substrates and analyzed using several techniques. X-ray diffraction (XRD) data showed that PVDF films crystallize at an annealing temperature above 130 °C. Polarization versus electric field (PE) ferroelectric measurements were done for samples prepared with electrodes. PE measurements show that the coercivity of the films increases as the maximum applied electric field increases. The coercivity dependence on the frequency of the applied electric field can be fitted as $f^{0.6}$. The results also show that the coercivity decreases with increasing the thickness of PVDF film due to the pinning effect. Next, we have demonstrated that those PVDF properties can be controlled by applying an external magnetic field. Samples were created in a layered heterostructure, starting with a Fe thin film, PVDF above that, and followed by another thin film of Fe. Extended X-ray absorption fine structure (EXAFS) spectroscopy was used to study the interface between PVDF polymer films and ferromagnetic iron thin films. Conventional

EXAFS was applied to identify the structure of a Fe film sandwiched between two PVDF layers. An electric signal was then applied to the polymer to study the effects polarizing the polymer has on the Fe atoms at the interface. This shows that the Fe atoms diffuse into the PVDF layer at the interface between the two layers. Polarizing the film causes further diffusion of Fe atoms into the polymer. We also found that as the applied magnetic field is changed, the switching of electric polarization for the PVDF displayed a dependence on the external magnetic field. We also noticed that both the coercivity and polarization for the PVDF polymer display hysteretic features as the applied magnetic field is changed. We also found that the thickness of both the iron layers and the PVDF layer has an effect on the magnetoelectric coupling in our samples. The same strain applied to a thicker PVDF layer becomes tougher to flip the polarization compared to a thinner PVDF layer. As the iron film thickness increases, the strain also increases, and the polarization of the PVDF polymer is more easily flipped. We also found that the magnetoelectric sensitivity increases as both the PVDF and iron layers increase in thickness. We have shown that it is possible to control the ferroelectric properties of a PVDF film by tuning the magnetic field in a heterostructure. Our experiments show a coupling between the electric polarization and applied magnetic field in multiferroic heterostructures much larger than any previously reported values. Previous reports have used inorganic materials for the ferroelectric layer. Organic polymers have an electric dipole originating at the molecular level due to atoms with different electronegativity that are free to rotate. To flip the polarization, the chains must rotate and the position of the atoms must change. This increases the force felt locally by those chains. Using this polymer, we are able to increase the magnetoelectric coupling.

CHAPTER 1. INTRODUCTION

The development of new electronic devices, based not on the electric charge in a material but on the spin inherent in each electron, form the basis of spin-based electronics, or spintronics. These devices are intriguing due to their wide range of applications in areas such as energy resources [1,2,3,4], computer and information technology, and life sciences [5].

Magnetic nanostructures have recently shown much promise in many applications including giant [6,7] and tunneling [8,9] magnetoresistance, which are used in current and future computer memory applications respectively. Magnetic nanomaterials also have potential applications in fields involving magnetic targeting drug delivery, high-resolution magnetic resonance imaging (MRI) and hyperthermia generation agents [10].

Combining a ferroelectric polymer and ferromagnetic material, or magnetoelectric coupling, is one theory behind advancing next generation electronic devices [11,12]. Creating and classifying materials where the multiferroic effects exist is crucial in the advancement of microelectronics [11,13]. One advantage of using ferroic devices is the possibility that they can be easily manipulated by applying an external electric field and thereby controlling the magnetic properties of the device, and vice versa. Conventional devices make it difficult to retain both of those properties.

One of the most useful applications for these new devices is in flash memory. Current flash memory devices contain memory cells that resemble standard metal–oxide–semiconductor field-effect transistors (MOSFET), except in these devices the transistor has two gates instead of one. Figure 1.1 shows an example of a flash memory MOSFET. The control gate is the same as a standard MOSFET control gate. The added gate is the floating gate below it. This floating gate is insulated by an oxide layer.

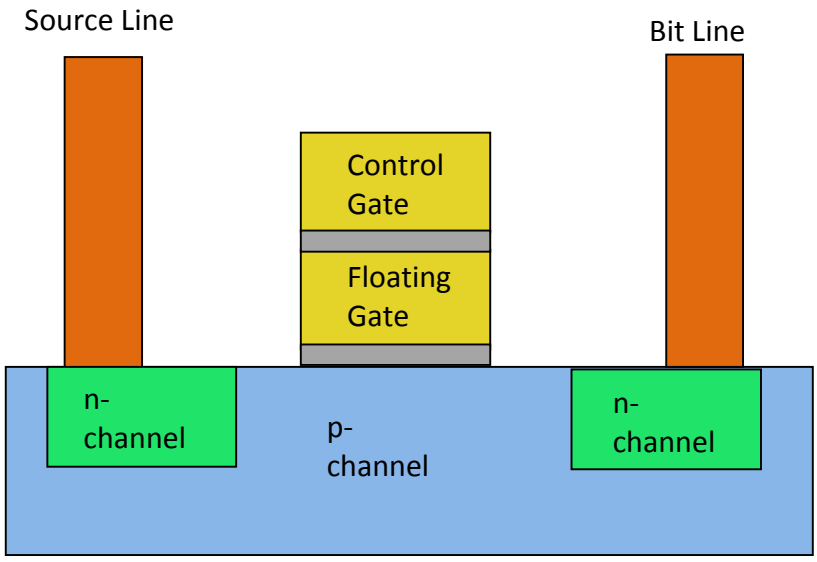

Figure 1.1: Typical flash memory MOSFET schematic. In this device, an extra, oxide-insulated floating gate is added, resulting in trapped charges. These charges screen an electric field in the device, which changes the threshold voltage, allowing for reading and writing bits.

The floating gate is placed between the control gate and the MOSFET n-channels. Due to the insulating oxide layer on the floating gate, it is electrically isolated, so any charges placed on that gate are trapped there. Under normal conditions, these charges, once trapped, will remain isolated and will not discharge for many years.

When charges are isolated in the floating gate, they partially screen the electric field from the control gate. This electric field screening changes the threshold voltage of the device, meaning more voltage has to be applied to the control to make the n-channels conduct.

To read such a device, a voltage is applied to the control gate and the n-channel conductivity is tested. The current flowing through the MOSFET channel is sensed, and this forms the binary code, thus reproducing stored data.

Such flash memory devices have both their advantages and disadvantages. They are advantageous because they are cheap to produce, they are non-volatile (i.e. they hold information for long periods of time), and they can be read quickly. The main disadvantage to flash memory is that it can only be written from binary 1 to 0, not from 0 to 1. So, if a binary 0 is written in the MOSFET, to change the bit back to a 1, the device has to be erased. But, individual bits cannot be erased; whole blocks of memory cells have to be completely erased and rewritten to save a change in one single bit. This makes the writing process much slower than the read cycle. Another disadvantage is that this write/rewrite cycle is limited in flash memory, and the device will fail after a number of write/rewrite cycles (typically about 100000).

In an effort to make more reliable, faster memory devices, a new type of flash memory is being used. These devices replace the standard MOSFET memory cells with magnetic tunneling junctions, and are called magnetoresistive random-access memory (MRAM). These devices have been found to be more reliable, and storage devices of this type are used as instant boot computers.

However, these devices are not without their disadvantages. In MRAM devices, two ferromagnetic layers are separated by an insulating spacer. The bottom layer is attached to a pinned antiferromagnetic layer, thus creating a pinned magnetic layer. The upper layer can be magnetized parallel or antiparallel to the lower layer. These two states represent the 1 and 0 state, and can be seen in Figure 1.2 [14]. When the magnetization directions are parallel, there is lower resistance for the tunneling current through the materials. When the magnetizations are antiparallel, there is a higher resistance.

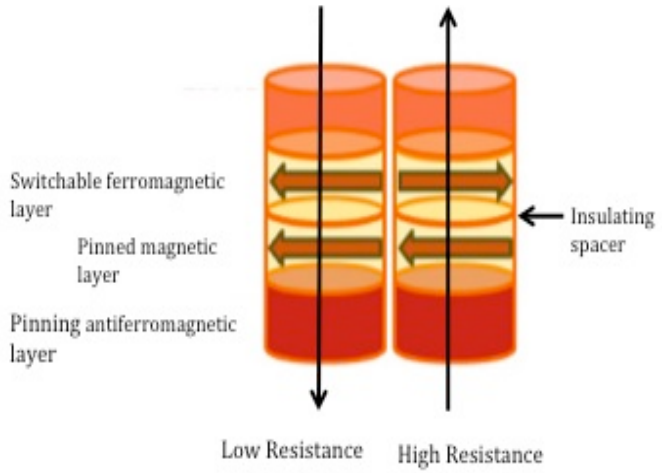

Figure 1.2: Example of low resistance and high resistance magnetizations in MRAM devices. The low resistance, or "0" bit, occurs when the pinned and free magnetic layers are magnetized parallel to each other. The high resistance, or "1" bit, occurs when the magnetizations are antiparallel [14].

To read and write this type of memory, these individual cells are connected to lines to send and receive current. The high resistance state is considered the "1" state, and the low resistance state is considered the "0" state. To write a bit, the top layer has to be

switched in some way. Figure 1.3 shows an example of these cells connected together, and how writing is done [15]. By applying a current to the word line and reading the tunneled current, the bit can be read.

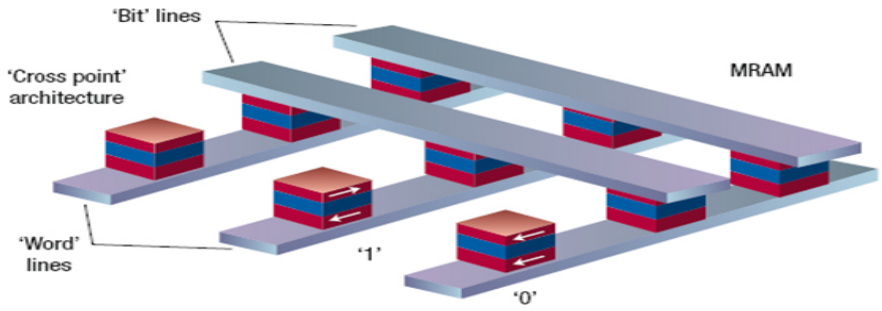

Figure 1.3: This is an example of many individual cells connected in an array to form an MRAM memory cell. The bit lines are used to switch the magnetization direction of the top layer. The word line reads the bits based on the resistance of the cells [15].

Currently, there are 2 ways to switch the top layer and write MRAM devices. The first involves using an external magnetic field to magnetize the top layer. In this method, a current is sent through the bit line, as shown above. This current passing through a wire produces a local magnetic field, either parallel or antiparallel to the magnetization direction in the pinned layer, depending on the direction of the current. An example of this can be seen in Figure 1.4 [16].

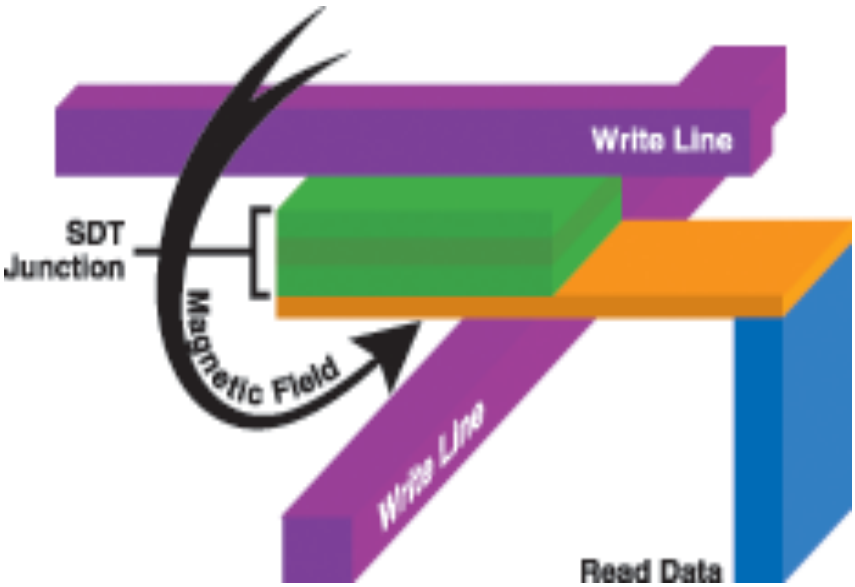

Figure 1.4: How to write MRAM cells using a magnetic field. The magnetic field can be flipped by reversing the direction of the current through a write line. This has the disadvantage of possible unwanted writing of neighboring bits [16].

This device has one major drawback. In a memory device that consists of many cells, the applied magnetic field can write any layer. If multiple cells are not spaced apart enough, there will be unwanted writing of neighboring bits. This also leads to the problem that since the cells have to be spaced some distance apart, there is a limit in the number of cells that can be used, and therefore a limit to the amount of storage in a given area.

The other way to magnetize or switch the top layer is by directly using current. This technique is called spin torque transfer (STT). This technique uses the property of spin in an electron. An electric current is generally unpolarized and consists of equal spin-up and spin-down electrons. A spin-polarized current is one that has more electrons of one spin. By passing a current through a thick magnetic layer, a spin-polarized current

can be produced. If this current is then directed into a ferromagnetic layer, the angular momentum from the electron spins can be transferred to the layer, thus changing the orientation or magnetization of the layer. These effects are only seen in nanometer scale devices. Figure 1.5 shows an example of a STT device.

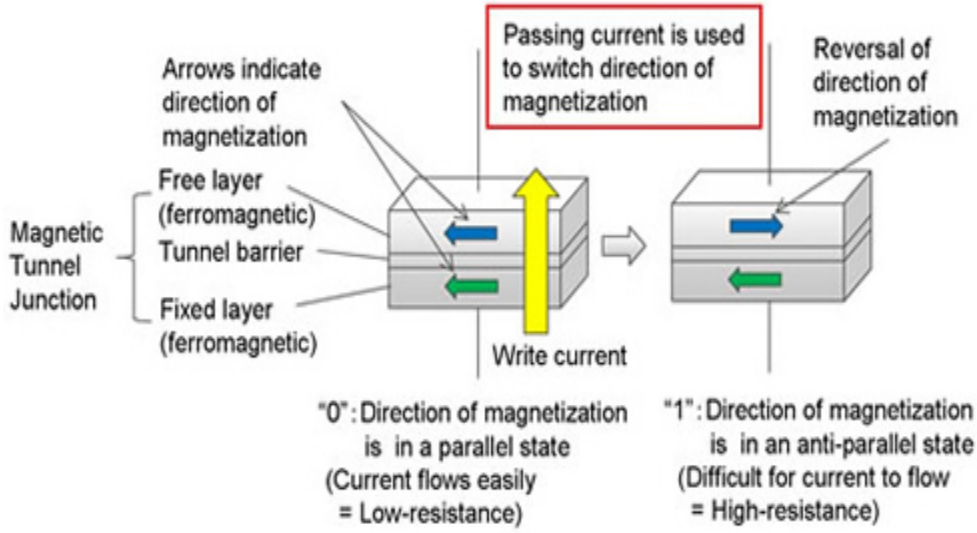

Figure 1.5: A diagram of a STT MRAM device. In these devices, a polarized current is directed through the cell, and this polarized current magnetizes the top layer. The drawback to this technique is that the current must be very large.

The polarized write current can be used to switch the top layer. This allows for single bits to be written/rewritten. The bits can be read in the same manner as other MRAM devices. The drawback to STT devices is the amount of current necessary to write the bits. To flip the magnetization of the entire top layer, a large amount of polarized current is needed. At present, this high current is unattainable in small devices. Also, with high currents, the unwanted magnetic fields can write neighboring bits, as described earlier. This could cause a loss of data and errors.

Research is now focusing on creating devices that electrically control the magnetization with voltage rather than current. By using voltage and having very little current flow, devices will have very low power consumption. One way to achieve this technique is by creating ferromagnetic/ferroelectric/ferromagnetic devices. In these devices, a ferroelectric layer would replace the insulating layer. Using these devices and utilizing magnetoelectric coupling, the devices can be switched much quicker, maintaining the advantage of MRAM devices.

Current research has been exploring using functional organic materials as opposed to conventional inorganic materials for the ferroelectric layer. Compared with inorganic materials [17,18,19], ferroelectric organic materials are promising candidates for electronic device applications due to their intrinsic low-cost and flexible features [20,21]. One ferroelectric film that is drawing wide interest in studies is polyvinylidene fluoride (PVDF), as well as its' copolymers with trifluoroethylene (TrFE). PVDF is a type of ferroelectric polymer that shows strong piezoelectric and pyroelectric properties. These materials have shown potential for use in electronic devices and memory applications [22,23].

These polymers are important because they possess a high phase transition temperature of 80°C [24] that indicates the two-dimensional nature of the ferroelectricity, and because the ferroelectric properties can be controlled by varying different properties of the films [25,26,27]. It has also been seen that when these films are embedded with inorganic materials such as graphite nanoplatelets [28] and alumina nanoparticles, properties such as the thermal conductivity of the polymers is enhanced [29].

New approaches are being taken to study the interface between the polymers and the embedded materials. For useful microelectronic devices, the interface that is of the most importance is that between the ferroelectric polymer and ferromagnetic materials.

The outline of this thesis is as follows. In Chapter 2, we will discuss the background and theory of ferroic devices. Before creating multilayer heterostructures using different ferroic materials, we will first discuss the individual properties of these layers. We will then further analyze the properties of multiferroic materials and specifically magnetoelectric coupling. In Chapter 3, we will discuss the experimental techniques used in to analyze the layered heterostructures. First, the sample creation process will be explained in detail. Several different deposition techniques were needed to create the ferroic layers, as well as electrical leads. In this section, the conditions of deposition as well as deposition rates will be explained as well. Next, the main experiments used in this thesis will be explained. We will look at the process of analyzing the ferroelectric properties of a material using a ferroelectric tester. In the final part of this chapter, the process of X-ray absorption fine structure (XAFS) will be described both theoretically and using analysis software. In Chapter 4, we will discuss the results of the experimental methods described in Chapter 3. The ferroelectric properties of the PVDF polymer were studied before it was used in the heterostructures. Then, after creating the layered samples, they were studied using XAFS and ferroelectric testing. Chapter 5 will present a short summary of the work presented in this thesis. Finally, Chapter 6 will introduce plans for furthering the study of multiferroic heterostructures.

CHAPTER 2. BACKGROUND

When a material exhibits spontaneous polarization, magnetization, or strain, it is referred to as a ferroic material. Materials that possess such properties are very useful in technological and information storage devices. For example, ferroelectric materials used in memory applications are prevalent in smart card technology. Similarly, arrays of a ferromagnetic material can be used in non-volatile hard disk drives. Ferroelastic materials have biomedical applications, such as minimally invasive stents that widen narrow blood vessels.

Several crystals will undergo phase transitions if external parameters such as pressure or temperature are changed. When this transition is accompanied by a spontaneous change in directional symmetry, the crystal is called ferroic. When the symmetry is spontaneously broken by a phase transition and is caused by some order parameter η, it is referred to as a second-order phase transition. In the case of ferroic materials, the order parameter is polarization, magnetization, or strain. The definition of spontaneous breaks means that these changes must occur even in the absence of an external field.

When an external field is not present, thermodynamic equilibrium is achieved by minimizing the Helmholtz free energy, $F(T,\eta)$, with respect to the order parameter. Therefore, the necessary equilibrium condition is:

$$\frac{\partial F}{\partial \eta} = 0 \tag{2.1}$$

If an external field ξ (either electric field E, magnetic field H, or mechanical stress σ) is applied to a system, the total energy is described by the Gibbs energy relation:

$$G(\eta, \xi, T) = F(\eta, T) - \eta * \xi \tag{2.2}$$

Analyzing that equation, an adjustment must be made to the equilibrium condition to take into account the external field. To reach thermal equilibrium, the following must be true:

$$\frac{\partial G}{\partial \eta} = 0 \quad , \quad \frac{\partial^2 G}{\partial^2 \eta} > 0 \tag{2.3}$$

$$\frac{\partial F}{\partial \eta} = \xi \quad , \quad \frac{\partial^2 F}{\partial^2 \eta} > 0$$

These equations lead to the spontaneous condition on the order parameter. η(T) undergoes a transition, from zero to a non-zero value, at some temperature. This transition temperature is referred to as the Curie temperature, T_C.

If we look at the region when the temperature is below the Curie temperature and the material is in a ferroic state, the breaking of symmetry leads to a spontaneous ordering even without an applied field. Without this applied field, any orientation for the order parameters is equally favorable. This leads to the formation of domains enclosing regions of equally oriented order parameters. These domains, when taken together for a whole material, result in a macroscopic orientation of zero.

When the Gibbs energy is plotted as a function of the order parameter at a temperature below the Curie temperature, the result is a double well potential. The order

parameter will stay in this well unless an applied field is large enough to allow it to overcome the potential barrier. This leads to the concept of hysteresis in ferroic materials.

The previous paragraphs describe three common properties of all ferroic materials: Curie temperature, hysteresis, and domains. The following sections will microscopically analyze the order parameters for each type of ferroic material, and will describe these common properties in more detail.

2.1 Ferroelectricity

2.1.1 Definition and Properties

Ferroelectric materials are defined as those materials that contain an axis along which a spontaneous polarization can be established below a critical, or Curie, temperature. By applying an electric field to the material, the direction of the polarization can be changed. The alignment of positive and negative charges within unit cells of the material gives rise to dipole moments within each unit cell. The polarization of the material due to these dipole moments can be measured by analyzing the surface current through the material. One distinguishing characteristic of ferroelectrics is the hysteretic behavior of the polarization as a function of an applied electric field. Figure 2.1 shows an example of a ferroelectric polarization vs. electric field (PE) curve [30]. In Figure 2.1, it can be seen that a net polarization in the material continues to exist after the external electric field is removed. When a ferroelectric material is above its' Curie temperature, it exists in a paraelectric phase, and functions as a dielectric with no hysteresis and higher symmetry. In these cases, the material possesses no spontaneous polarization when the applied electric field is removed. Some ferroelectric materials have additional transitions

below the Curie temperature, at which point they transition back to a paraelectric state. “Rochelle salts” (potassium hydrogen tartrate) exhibit this dual transition with upper and lower Curie temperatures, and was the first material in which ferroelectricity was observed [31].

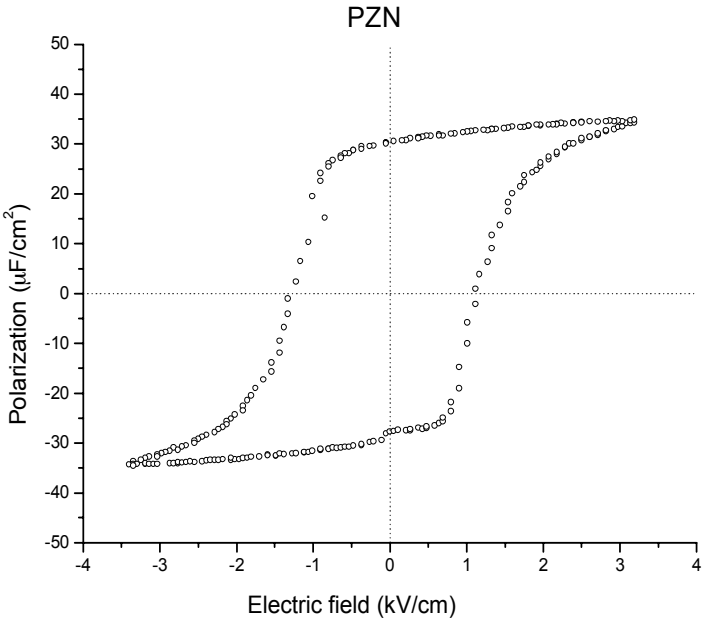

Figure 2.1: Typical hysteresis loop for a ferroelectric material. An applied external electric field aligns dipole moments inside the material along the field direction, resulting in a net polarization, which is preserved even after the field is removed [30].

Ferroelectric materials commonly have a large piezoelectric effect, or strain produced in response to an applied external electric field. The direct piezoelectric effect is the development of strain in a crystal when an external electric field is applied to a material and it becomes polarized. Polarization of a material can also arise when strain is

applied, the opposite effect. This manifestation of electrostriction is a piezoelectric effect of the second order in which the strain is proportional to the square of the applied electric field. Piezoelectric tensors describe the material's performance as an electric field is applied. Typically, the piezoelectric effect is larger than the electrostrictive effect. In some materials, this is not the case, and in such materials the hysteresis effects are reduced because the electrostrictive effect is preferred due to the strain direction being independent of field direction.

The capacity of ferroelectric materials to alter their atomic structure due to applied fields is a source, in some cases, of high values for permittivity and the dielectric constant. For example, ferroelectric magnesium niobate has a dielectric constant of approximately 30000 [32]. The discovery of barium titanate and similar ferroelectrics was the beginning of vigorous studies on the topic of ferroelectrics. Often, these ferroelectric materials were used for capacitors in integrated circuits. In ferroelectric materials, the most common and most useful property is the piezoelectric effect. Lead zirconate titanate (PZT, $Pb[Zr_xTi_{1-x}]O_3$) is the most commonly used ferroelectric, but new materials and new applications are always being developed.

Another important characteristic of ferroelectric materials is remnant polarization. As previously shown in Figure 2.1, the polarization of a material is hysteretic when an electric field is applied. At high electric fields, the material reaches a maximum polarization, called the saturation polarization. As the electric field returns to zero, the material is left with some remnant polarization, which can eventually be removed by applying a large enough field in the opposite direction. In contrast, dielectric materials retain no spontaneous polarization when an electric field is removed. There are no

hysteretic effects in these materials, and the PE curve is a straight line with a slope proportional to the electric susceptibility, or the dielectric constant minus one.

A ferroelectric domain is a collection of unit cells within a ferroelectric material in which the spontaneous polarization is uniformly polarized. For example, in Figure 2.2, there are 6 possible polarization directions at room temperature for PZT. Above the Curie temperature, all 6 directions are equivalent and indistinguishable. As the temperature drops below the Curie temperature, the spontaneous polarization can form along any of these possible directions. In a ferroelectric material, a domain can be spontaneously polarized in any of these directions, but the net polarization of the material, in a virgin state, will be zero.

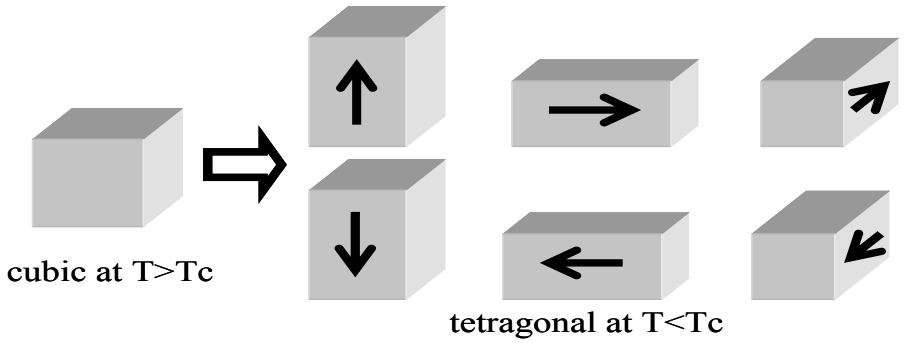

Figure 2.2: Schematic diagram of possible polarization directions in PZT. Below the Curie temperature, there are 6 possible polarization directions. Above the Curie temperature, all those directions are equivalent and indistinguishable2.

Ferroelectric materials contain many domains. Thus, a pattern in bulk materials is unavoidable. These patterns can be influenced by defects, thermal history of the material, strain, and the applied field. Ideal crystals would still exhibit these patterns because of the

minimization of the energy of the domains. In these crystals, domains are introduced so that the polarization is parallel to the surface.

Since bulk materials contain many domains, there will be an interface between any two domains. This interface is referred to as the domain wall, and the width of these walls is very small, generally on the nanometer scale or smaller [33]. In a cubic crystal structure, the angles between two domains are either 90° or 180°. Of the two, 180° domain walls are more widely studied because the domains can be reversed with minimal structural strains.

When oppositely oriented polarizations are separated by a wall, they are called *c* or 180° domain walls, while perpendicularly oriented domains are separated by *a* or 90° domain walls. Figure 2.3 shows a schematic of the domain wall types. Understanding the microscopic picture of these domains is crucial for advancing better macroscopic devices that have these effects.

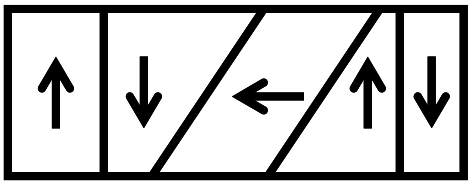

Figure 2.3: Diagram of 90° and 180° domain walls. The arrows indicate the polarization direction.

Domain walls are formed due to energy contributions from temperature, elasticity of the material, the location of the domain relative to the sample edge, the polarization switching, and electrostatic interactions, to name a few [34].

When the applied external electric field is applied opposite to the direction of a domain's polarization, the polarization will reorient in the direction of the applied field [35]. This is a reversible process referred to as polarization switching. When the polarization is parallel to an applied electric field, the switching is done.

The net polarization of an initially unpolarized ferroelectric material is very small. When an electric field is applied, there is a linear relationship between switchable polarization and the applied electric field. When this occurs, the polarization of each domain is aligning, and there is no polarization switching. As the electric field increases, however, domains with opposite aligned polarization start to align with the electric field, in a more energetically favorable direction. This switching process continues until all of the domains are aligned to the direction of the applied field. As mentioned earlier, as the electric field is reduced to zero, there remains a remnant polarization. If the electric field is then aligned opposite to the original direction, more of the domains flip to align to the applied field. The strength of the electric field required to return the polarization of the material to zero is called the coercive electric field, E_c. This process can be repeated as the direction of the electric field changes, giving rise to the PE loops and the hysteresis curve.

This polarization switching, and the energy required to switch the domains, is dependent on the volume of the material. The following is a simplified presentation of this relationship. The power in any electronic device, P, is expressed by the current in the device I and the electric potential U as:

$$P = I \cdot U \tag{2.4}$$

The energy E_{tot} supplied to the device is expressed as the time integral of the power:

$$E_{tot} = \int P(t)\, dt = \int U \cdot I\, dt \tag{2.5}$$

Using this expression for energy, it is possible to estimate the energy per volume necessary to switch the ferroelectric state of material with thickness *x*, area A and volume V, and can relate that expression to the charge q through the material, the applied electric field E, and the polarization P.

$$\frac{E_{tot}}{V} = \frac{\int U \cdot I dt}{x \cdot A} = \int \frac{U}{x} \frac{dq}{A} = \int E \cdot dP \tag{2.6}$$

Referring back to the example PE loop in Figure 2.1, we define a parameter called the polarizability, p, as the saturation polarization, P_S, divided by the electric coercive field E_c, or the slope of the ferroelectric characteristic linear regression. Equation 2.6 can now be rewritten as [36]:

$$\frac{E_{tot}}{V} = \frac{1}{2} \frac{P_S^2}{p} \tag{2.7}$$

Using the definition of permittivity of a material as the change in polarization divided by the change in applied field, equation 2.7 can be written as:

$$\frac{E_{tot}}{V} = \frac{1}{2} \frac{P_S^2}{\varepsilon_r \cdot \varepsilon_0} \tag{2.8}$$

Here, ε_r is the dielectric constant of the material. Equation 2.8 now relates the volume of the sample and the energy required to switch the polarization to the saturation polarization and the material's dielectric constant.

Several different theoretical models describe the phase transition in ferroelectric materials. A phenomenological model has been produced by Landau and Ginzburg that uses the polarization as an order parameter [37]. Cochran developed a soft mode approach involving optical vibration modes [38]. A shell model has been used to consider

the polarizability of oxygen in various ferroelectric oxides [39]. Other models currently being considered are analysis or orbital hybridization [40], electronic density mapping [41], and interfacial effects in ultra-thin films [42].

Here, the Landau-Ginzburg theory will be considered to describe the ferroelectric transition. This model is also used to describe superconductivity and magnetism. This model does not describe the microscopic mechanisms of the phase transition, but it is useful to macroscopically understand the polarization change near the phase transition and study the domain pattern formation [43,44,45]. Using this theory, the Gibbs free energy is expanded as a power series depending on temperature and polarization. Close to the transition, the Gibbs energy is given by [46]:

$$G = \frac{1}{2}\alpha(T - T_C)P^2 + \frac{1}{4}\beta P^4 + \frac{1}{6}\gamma P^6 + \cdots \quad (2.9)$$

The above is a simplified case with polarization along one of the domain axes with no applied electric field. The free energy is a double well potential with two energy minima at $P = +P_S$ and $P = -P_S$. The coefficients can be determined experimentally for different materials, and the signs determine the type of phase transition (first or second order). A graph of the free energy for different temperatures above and below the Curie temperature is shown in Figure 2.4 [47].

This figure also shows the double well potential. In most cases, materials show first order phase transition when the polarization drops to zero at the Curie temperature. Under the influence of an external electric field, a -P•E term must be added to the Gibbs energy.

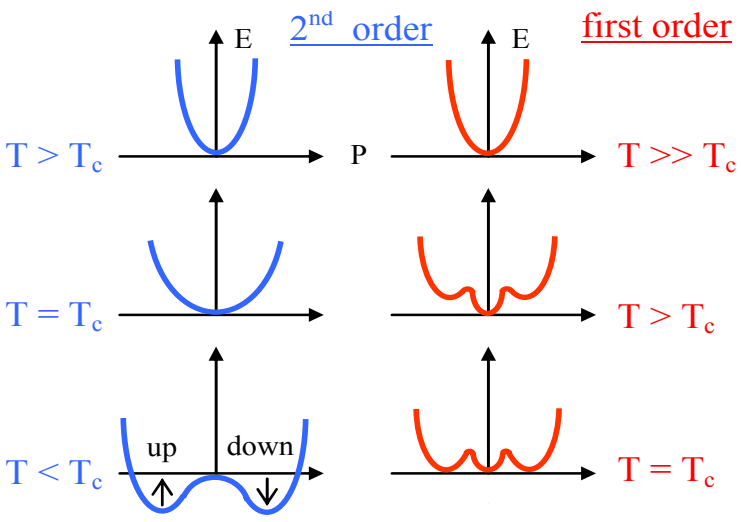

Figure 2.4: Free energy of a ferroelectric for first and second order phase transitions. The transition below T_C shows the double well for the polarization minima [47].

2.1.2 Ferroelectric PVDF Polymer

Compared with conventional inorganic materials, ferroelectric organic materials are promising candidates for electronic devices applications due to their intrinsic low-cost, lightweight, and flexible features. One ferroelectric film that is drawing wide interest in studies is polyvinylidene fluoride (PVDF). PVDF is a type of ferroelectric polymer that shows strong piezoelectric and pyroelectric properties [48,49]. The polarization of PVDF comes from the alignment of dipoles between F and H atoms when the film is in its crystalline form. PVDF is being widely used due to its cost and the fact it can be easily cut and molded into different shapes in addition to its ferroelectric properties. These properties have made PVDF polymers useful for many applications including transistors [50], sensors [51], and molecular electronics [52,53]. Different approaches have been taken in creating and characterizing PVDF films. Many studies have been done linking its

ferroelectric properties to the crystalline structure and different fabrication methods [54,55,56].

The atomic structure of PVDF is CH_2CF_2, as shown in Figure 2.5. PVDF is found to have four crystal phases named α, β, γ, and δ. The crystallization forms a chain conformation with two parallel unit cells [57]. The CH_2CF_2 units have net dipole moments due to the difference in electronegativity between the hydrogen and fluorine atoms. The chains of parallel unit cells are deposited monolayer by monolayer, and are 1.75 nm thick.

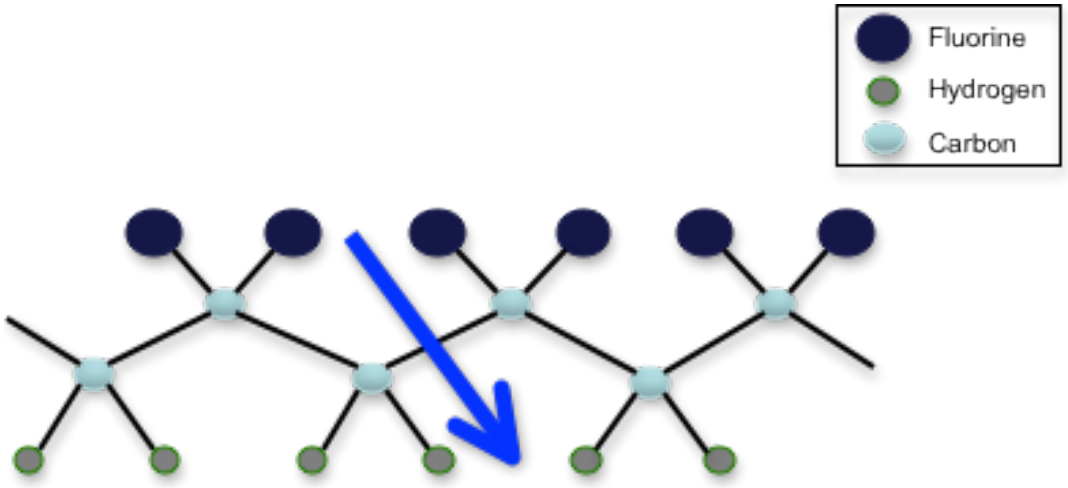

Figure 2.5: Schematic drawing of the molecular chain of PVDF polymer. The arrow indicates the dipole directions resulting from the difference in electronegativity between fluorine and hydrogen atoms. The thickness of the chain is 1.75 nm.

This work focuses on the β phase of PVDF. To get the β phase, the α phase must be annealed during deposition, causing the overall polarization to flip and produce spontaneous polarization in the crystallites. The β phase of PVDF shows the highest piezoelectric effect of the four crystal phases [58].

Not only are the dipole effects in the crystal important to the remnant polarization in PVDF, but trapped charges have an effect as well. Experiments have shown that decreasing the conductivity of PVDF with increasing pressure indicates ionic charge transport [56], and that charges can be injected into the PVDF through a cathode connection to form a poled polymer.

These poled polymer films show piezoelectric effects similar to other ferroelectric ceramics. The lasting polarization in polymers consists of both trapped charges and the oriented dipoles. The most common explanations for the origin of piezoelectricity in poled polymers are dimensional effects and intrinsic effects.

The dimensional effect can be explained as follows. If remnant polarization in the polymer is unchanged, the lateral stretching of the polymer decreases the film thickness, thereby increasing the induced charge in the electrodes [59]. From this theory, the piezoelectric constant e_{31} can be related to the polarization P and strain e by the Poisson ratio ν and the remnant polarization [60]:

$$e_{31} = \frac{P}{\varepsilon} = \nu \cdot P_r \tag{2.10}$$

The intrinsic effects can similarly be explained. The remnant polarization is changed by the applied stress to the crystal, which includes the oriented molecules during crystalline formation. The intrinsic effect is determined by the product of the remnant polarization times the electrostriction constant, a constant that relates a material's deformation to an applied electric field [61].

These properties, as well as the various applications, make PVDF polymers very interesting for advancing research.

2.2 Ferromagnetism

Mankind has known of the phenomenon of magnetism for thousands of years. The magnetism, and similarly the magnetic moments of atoms in a material, has three principal sources: 1) electron spin, 2) orbital angular momentum of the electron about the nucleus, and 3) a change in the orbital moment induced by an applied magnetic field. The first two result in paramagnetic contributions to the magnetism, and the third results in a diamagnetic contribution [62].

In a crystal, the overall magnetism depends on the magnetic response of each atom and the interaction between magnetic moments. When there are no unpaired electrons around a nucleus, there will be no net magnetic moments, and the material will exhibit diamagnetic behavior. When there are unpaired electrons, every atom has a net magnetic moment. Depending of the interaction of these moments, a material may be paramagnetic (PM), ferromagnetic (FM), antiferromagnetic (AFM), or ferrimagnetic (FIM). In a paramagnetic material, there is no alignment of adjacent magnetic moments. In ferromagnetic materials, adjacent moments are aligned parallel to one another. For an antiferromagnetic material, the alignment is antiparallel. Finally, in ferrimagnetic materials, the moments are antiparallel, but the net magnetization of the material is non-zero [63].

For a ferromagnetic material, the order parameter η previously described is the magnetization, M, and the applied field is the magnetic field, H. The physical characteristics describing ferromagnetic materials are comparable to ferroelectric materials. Magnetization is the net magnetic moments in unit volume.

The magnetic properties of an atom are decided by the electron configuration. The magnetic moments of an electron are separated into the orbital angular momentum magnetic moment and the spin magnetic moment. The orbital moment is defined as:

$$m_z = -\mu_B * l_Z \tag{2.11}$$

The spin moment is defined as:

$$m_s = -g_e * \mu_B * s_Z \tag{2.12}$$

In these equations, μ_B is the Bohr magneton, $\mu_B = e\hbar/2m_e$, $g_e = 2(1 + e^2/4\pi\varepsilon_0 hc) = 2.0023$, l_Z is the magnetic quantum number, and s_Z is the spin quantum number, ±1/2 [64].

The total magnetic moment is related to the total angular momentum quantum number (J_Z) by the expression:

$$m_Z = -g * \mu_B * J_Z \tag{2.13}$$

Here, g is called the Lande splitting factor or Lande g-factor, and is given by the expression:

$$g = \frac{3}{2} + \frac{S(S+1)-L(L+1)}{2J(J+1)}, \tag{2.14}$$

where S is the spin angular momentum, L is the orbital angular momentum, and J is the total electronic angular momentum.

The total electronic angular momentum is decided by of orbit-orbit, orbit-spin, and spin-spin couplings. For atoms where the orbit-spin interaction is weak, the coupling is described by Hund's Rule. Therefore, we can compare the magnetic moments of ions between experimental and calculated values.

As described earlier, these magnetic moment interactions lead to different types of magnetism. If J is equal to zero, the material is diamagnetic. The different alignments of

magnetic materials result in J being non-zero, leading to FM, AFM, and FIM. Figure 2.6 shows the different alignments and magnetic orders.

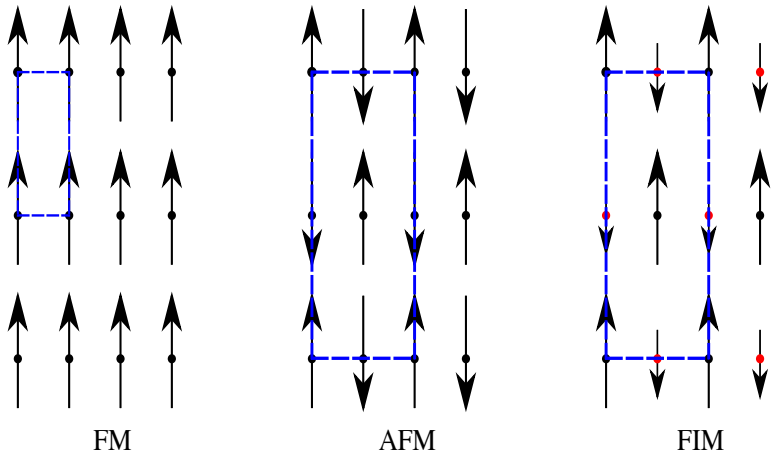

Figure 2.6: Magnetic moment alignments for simple ferromagnetic (FM), antiferromagnetic (AFM), and ferrimagnetic (FIM) magnetic orders.

These three structures are highly unstable at high temperatures because of thermal agitation effect. At these high temperatures (i.e. above the Curie temperature), the material is paramagnetic. The stability of the magnetic structure is related to the exchange interactions.

According to the Pauli Exclusion Principle, there is zero probability of finding two electrons with identical spins at the same point in space, but opposite spins can occupy the same point. The average separation of electrons, r, will be larger for parallel spins than for antiparallel spins. The inter-electron Coulomb repulsion energy, $e^2/4\pi\varepsilon_0 r$, is therefore smaller for parallel spins than it is for antiparallel spins. This effect is referred to as the exchange interaction. For the entire material, the exchange energy is expressed as [65]:

$$H = \sum_i \sum_{i \neq j} J_{ij} \cdot S_i \cdot S_j \quad (2.15)$$

The sign on the coupling constant J determines the magnetic order. If J is positive, the material is ferromagnetic, if J is negative, the material is antiferromagnetic. Very short distances between spins supports antiferromagnetism, then ferromagnetism, and long distances support paramagnetism. This is because the exchange interaction is a short-range interaction. Ferromagnetism can further be explained using a double exchange interaction.

For example, examine the interactions in manganites, MnO(OH) [66]. The double exchange interactions in this material can help explain the ferromagnetic properties in metallic materials. In these materials, there is an existence of a disordered mixture of Mn^{3+} and Mn^{4+}. The free electron in the material will hop from Mn^{3+} to O^{2-}, or from O^{2-} to Mn^{4+}, depending on the local spins of the manganese atoms. If the spins of the manganese ions are parallel, the free electron from Mn^{3+} hops to the spin site in the oxygen vacated when the electron moved to Mn^{4+}. If the spins of the manganese ions are antiparallel, the electron cannot hop to the oxygen because its spin is parallel to the spin that was vacated in the oxygen. According to this mechanism, the compound is ferromagnetic and has itinerant electron behavior [67]. These metallic ferromagnets behave like conductors.

There is another interaction that can also help explain ferromagnetic and antiferromagnetic behavior. Hendrik Kramers first proposed super exchange interaction in 1934 [68] and the theory was then further developed in the 1950's and 1960's [69,70,71,72]. The ferromagnetic and antiferromagnetic orders are explained by super exchange theory depending on orbital configurations.

To further explain, we look at two ions of a material X. Ion X has partially occupied outer orbitals. Ion X' has empty outer orbitals. These ions couple to one another through a third, intermediary, non-magnetic ion, similar to an oxygen atom. There are 5 cases of super exchange interaction that depend on the orbital coupling and magnetic ions: 1) strong AFM, 2) weak AFM, 3) weak FM, 4) FM, and 5) AFM. Examples of the orbital interactions can be seen in Figure 2.7 [73].

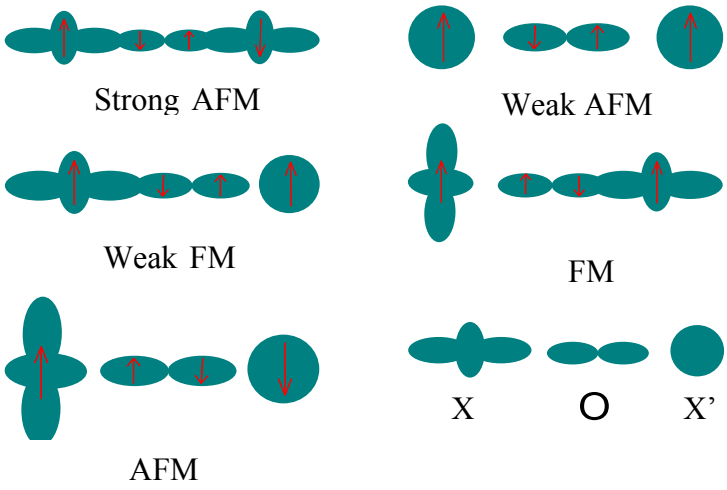

Figure 2.7: Orbital interactions for different magnetic structures. The different cases depend on orbital coupling and the magnetic ions in the different atoms.

Similar to ferroelectric materials, ferromagnetic materials also form domains. Ferromagnetic domains enclose regions of magnetic identical magnetic moment orientation. If the macroscopic magnetization is saturated at high applied external magnetic fields, then the ferromagnetic material is in a single domain state. When the external field is either removed or decreased to zero, some domains will form to minimize the free energy of the system as described earlier. This reduces the macroscopic magnetization to a value that is referred to as the remnant magnetization. As the applied

field is continuously decreased to a negative polarity value, the net magnetization will eventually reduce to zero. This is the coercive magnetic field. However, as the crystal is still ferromagnetic, there is spontaneous magnetization and the vanishing net magnetization is caused by the decay of regions into domains. As with ferroelectric domains, adjacent domains are separated by domain walls, and the domains are either aligned or anti-aligned to neighboring domains.

Magnetic fields are described by magnetic induction, $B = \mu_0 * H$ and is related to the magnetization M by:

$$B = \mu_0 * (H + M) \tag{2.16}$$

In ferromagnetic materials, H and M are non-linearly related because of hysteresis, similar to the P-E relation for ferroelectrics. From the thermal equilibrium free energy equations, the relation is shown to be [74]:

$$\frac{\partial F}{\partial M} = B = \mu_0 * H \tag{2.17}$$

The magnetic susceptibility is defined as the magnetic field dependence of the magnetization:

$$\chi_M = \frac{\partial M}{\partial H} \tag{2.18}$$

These properties lead to a hysteresis loop similar to a PE loop, here dependent on magnetization and applied magnetic field (MH), as shown in Figure 2.8 [75].

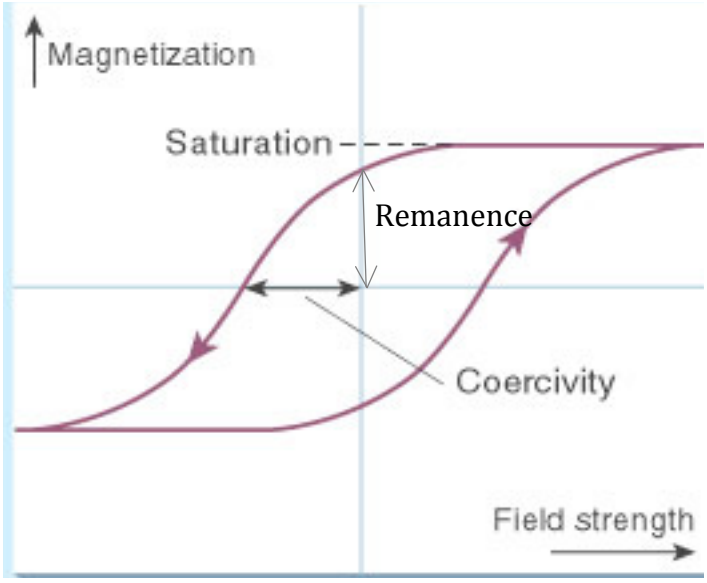

Figure 2.8: Sample MH hysteresis loop. For ferromagnetic materials, the magnetization changes as the applied field strength is changed, and displays hysteresis [75].

2.3 Multiferroic Materials and Magnetoelectric Coupling

In Ferroelastic materials, the order parameter is the strain, and is dependent on the stress, σ, as follows [76]:

$$\frac{\partial F}{\partial \varepsilon} = \sigma \tag{2.19}$$

Ferroelastic materials differ from ferroelectrics and ferromagnetics in that the free energy is only a course approximation. This is due to a phase mixture present even below the Curie temperature. While ferroelectrics and ferromagnetics contain domains that enclose regions with identical order parameters, ferroelastics have domains that are separated into two regions, called martensite and austenite regions. Because of this, a change in the strain order parameter is linked to phase transitions, not just domain reformation [77].

A multiferroic material is one in which more than one ferroic property exists in a material. This definition was originally proposed by Schmid in 1994 in an effort to describe the effects that allow the formation of switchable domains [78,79]. In multiferroic materials, the ferroic order parameters are coupled to one another. When a field is applied to the material, more than one of the parameters will change since they are coupled. A diagram of multiferroic interactions is shown in Figure 2.9 [80].

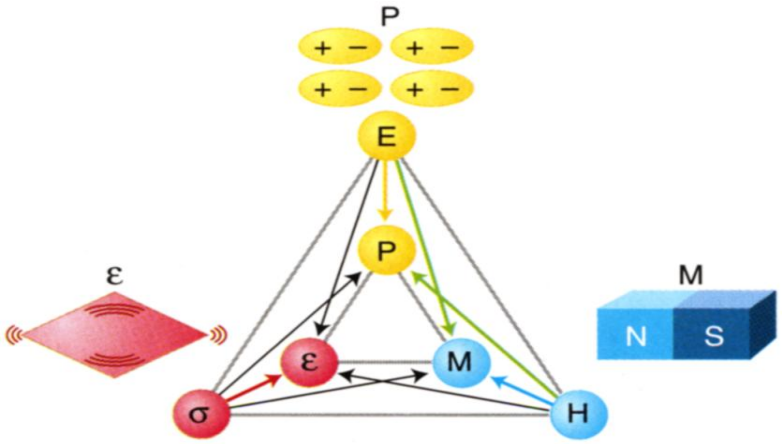

Figure 2.9: A diagram of multiferroic interactions. Multiferroic coupling occurs when changing a field will cause a change in one of the other parameters, as shown by the black and green arrows [80].

When the coupled effects are ferroelectricity and ferroelasticity (red and yellow in the figure), it is called the piezoelectric effect. In this case, an electric field controls the strain, or the stress controls electric polarization.

The second case occurs when ferromagnetic and ferroelastic properties are coupled, the case of magnetoelasticity (blue and red in the figure). This case occurs when stress controls magnetization, and when magnetic field controls strain.

The final, and most common, case of multiferroic materials is when ferroelectricity and ferromagnetism are coupled (yellow and blue in the figure, shown by the green arrows). This is the case of the magnetoelectric coupling. In the presence of magnetoelectric coupling, it is possible to control magnetic properties by an electric field [81], or to control electric properties by a magnetic field [82]. These two effects are called the magnetoelectric effect (ME). Figure 2.10 shows the overlay and interaction of magnetoelectric coupling. In this case, the coupling coefficient is defined as α, and is called the magnetoelectric coupling constant [83]. In the research of this thesis, this is the case that will be studied.

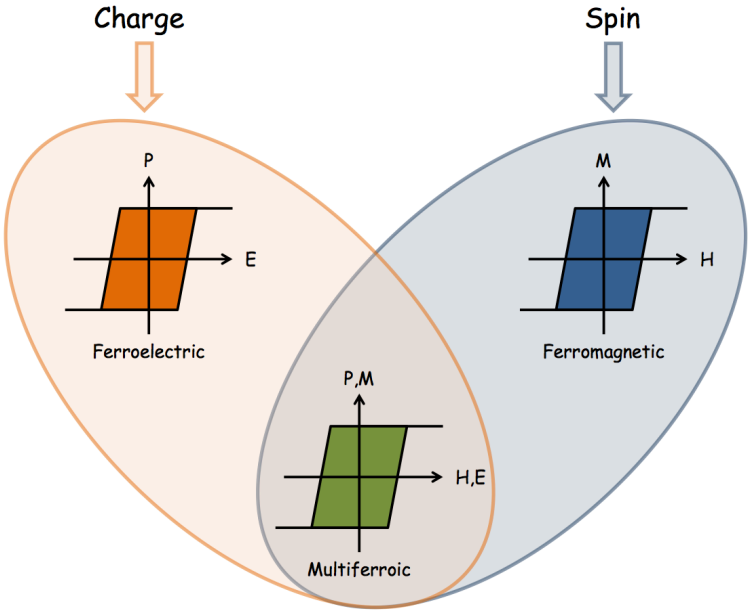

Figure 2.10: Magnetoelectric coupling diagram. For this type, the magnetic field controls polarization, or the electric field controls magnetization, as shown in the green graph. This leads to a magnetoelectric coupling constant, α [83].

Maxwell's equations have long demonstrated the relation between electric and magnetic fields [84,85]. However, during this time, they were considered as separate in solid state and nanaoscale physics: electrons and electric charge were the cause of electricity, and spin of atoms was responsible for magnetism. Curie [86] and Debye [87] introduced coupling between magnetic and electric properties. Landau and Lifshitz described the linear coupling between the parameters for certain magnetic symmetries in 1959 [88]. Later, Dzyaloshinskii and Astrov predicted and observed this coupling [89]. Soon after, nickel-iodine boracite exhibited true multiferrocity, not just magnetic symmetry based [90].

The next few sections will describe in detail several types of the magnetoelectric effect, as well as the cause of the coupling.

2.3.1 Single-phase Magnetoelectric Effect

Single-phase ME occurs when the coupling between ferroic layers arises directly between order parameters such as polarization or magnetization. Single-phase ME is described using the Landau theory, specifically the free energy, F, the polarization P, and the magnetization M in terms of the applied electric and magnetic fields, E and H respectively, and the order parameters. Doing so, the free energy is found to be [91]:

$$F(E,H) = \frac{1}{2}\varepsilon_0\varepsilon_{ij}E_iE_j + \frac{1}{2}\mu_0\mu_{ij}H_iH_j + \alpha_{ij}E_iH_j + \frac{\beta_{ijk}}{2}E_iH_jH_k + \frac{\gamma_{ijk}}{2}H_iE_jE_k + ... \quad (2.20)$$

Here, the first term is the contribution from the response to an electric field, where ε_{ij} is the relative permittivity. The second term is the response to a magnetic field, where μ_{ij} is the relative permeability. The third term represents the linear magnetoelectric

coupling, and the later terms represent higher order coupling. α_{ij}, β_{ijk}, and γ_{ijk} are the coupling coefficients. By differentiating F with respect to E and H, respectively, then setting E_i and H_i to zero, you get the following for electric polarization and magnetization [91]:

$$P_i = \alpha_{ij} H_j + \frac{\beta_{ijk}}{2} H_j H_k + \ldots \tag{2.21}$$

and

$$\mu_0 M_i = \alpha_{ji} E_j + \frac{\gamma_{ijk}}{2} E_j E_k + \ldots. \tag{2.22}$$

It follows that the magnetoelectric effects in these materials are large, such that the magnetoelectric coefficient becomes: $\alpha_{ij}^2 \le \varepsilon_o \mu_o \varepsilon_{ij} \mu_{ij}$ by ignoring the higher order terms in the free energy.

In single-phase ME materials, the above magnetoelectric coefficients are coupled to one another. A change in one, such as β, by applying and electric field causes changes in the other parameters. Single-phase ME can be observed experimentally by measuring α. This has been done in many multiferroic materials [89,92].

In single-phase ME materials, the ferroelectric and ferromagnetic properties are held by the single material. For example, we will use $TbMn_2O_5$. Figure 2.11 [93] shows an electric polarization versus applied magnetic field graph for this material. As the magnetic field is applied, the polarization of $TbMn_2O_5$ changes, and shows hysteretic properties.

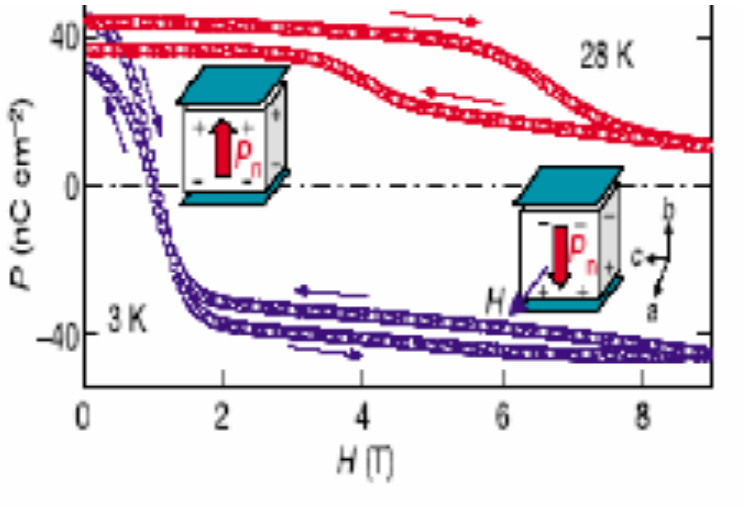

Figure 2.11: Polarization versus applied magnetic field for a single-phase ME. A change in an applied magnetic field changes the polarization. Single-phase ME occurs at low temperatures, as shown by the 3 K and 28 K temperatures of this experiment [93].

This graph does show of the main drawbacks to single-phase ME materials. These graphs were obtained at very low temperatures, 3 K and 28 K. At room temperature, the magnetoelectric effect is not present. Another drawback, as seen in the figure, is the size of the field required to see changes. The magnetic field (or electric field to magnetize) has to be very large; thereby making this material not applicable as devices such as storage drives.

2.3.2 Two-phase Magnetoelectric Effect

The other type of ME is two-phase, which happens when two separate ferroic layers are combined. A ferroelectric layer and a ferromagnetic of different material are layered together in what is called a heterostructure. Unlike single-phase ME, which is

caused by interaction between order parameters, two-phase ME occurs in two ways: 1) strain mediated, and 2) charge mediated through coupling between multilayers through interface bonding.

The first two-phase ME occurs when strain between layers causes changes in the polarization or magnetization. A schematic showing the steps of this process is shown in Figure 2.12. In this case, an applied electric field causes a shape change in the ferroelectric material. In a ferromagnetic material, by changing the shape with an applied stress, the magnetization state is altered. By combining the layers, a change in magnetization can be induced. Applying an electric field changes the shape of the ferroelectric material. Since it is bound to the ferromagnetic material at the interface, this change acts as the stress to change the shape of the ferromagnetic material. With that shape change, an altered magnetization of the sample is induced.

The other type of two-phase ME is charge mediated. This is done through spin-dependent screening of the electric field, which causes an imbalance of surface charge and leads to a change in the surface magnetocrystalline anisotropy. By applying an electric field to a metal film, conduction electrons on the surface of the film screen the electric field over the screening length of the metal, which is spin-dependent due to exchange interactions in ferromagnetic metals [94]. The spin dependence of the screening electrons creates a surface magnetization, or ME. The magnetization occurs only on the surface of the metal film, so this is a surface magnetoelectric effect, and therefore has little dependence on film thickness [95]. A schematic of this process is shown in Figure 2.13.

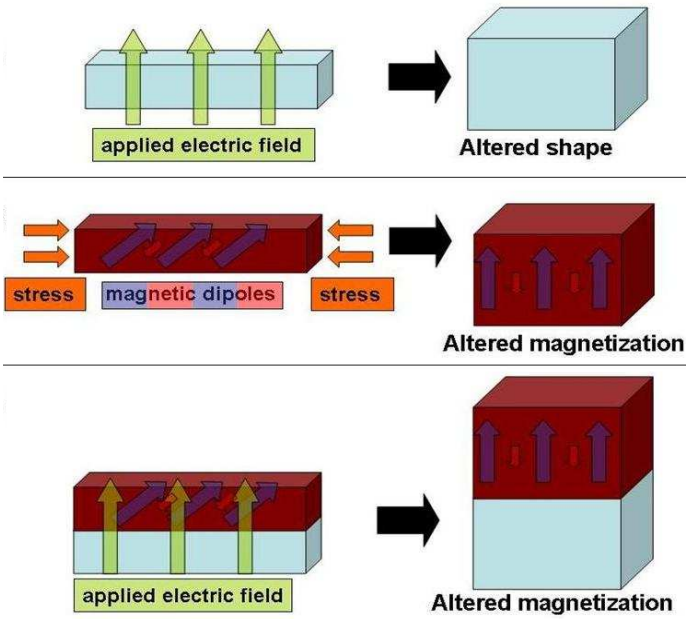

Figure 2.12: Schematic of strain mediated two-phase magnetoelectric effect. Applying an electric field to a ferroelectric material changes its shape. Changing the shape of a ferromagnetic material alters its magnetization. Combining the two, you can alter magnetization by changing the electric field.

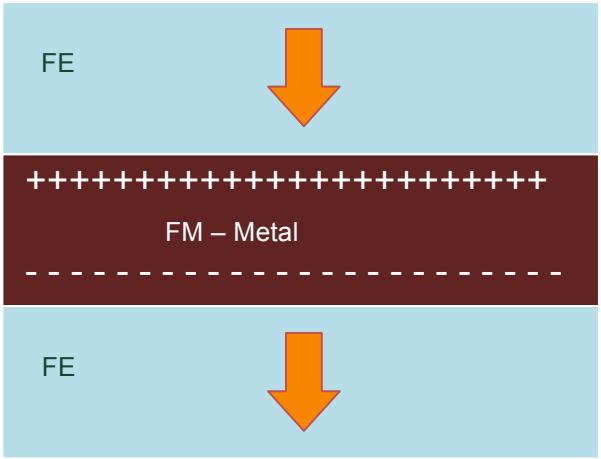

Figure 2.13: Schematic of charge mediated two-phase magnetoelectric effect. Current the sample causes charges to move to the surfaces, creating localized effects.

The origin of this ME is from induced spin-dependent charge densities on the film surface. Dipoles are formed on that surface to screen the electric field in the film, and the induced charge density is strongly spin-polarized. The spin imbalance of the screening charge causes an induced surface magnetization that reflects the presence of the surface ME. The net induced spin densities at opposite surfaces will have opposite signs, since the electric field is applied in an opposite orientation with respect to the surfaces.

The other occurrence of two-phase ME involves the coupling between different ferroic layers through interface bonding. Applying an electric field to a ferromagnetic film also changes the magnetocrystalline anisotropy energy (MAE). MAE, which is due to the spin-orbit coupling [96], is another materialization of the ME. It has been seen that the magnetic anisotropy in the film can be changed by alternating the polarization in the ferroelectric layer through an applied field [97]. This is because of the change in electronic structure at the interface. When an electric field directed outward from the film is applied, there is an increase in the MAE contribution from atoms at the surface of the film. When an electric field is directed inward, there is a decrease in this contribution. Therefore, it is possible to design ferromagnetic films with anisotropy that can be switched from in-plane to out-of-plane.

Two-phase ME due to interface bonding is also seen in the displacement of atoms at the interface caused by the overlap between atomic orbitals, which affects the interface magnetization. In the left set-up, D orbitals of manganese (gold and silver) are attracted to the positive charge, stretching the lobes of the orbitals up and down. The stretched lobe down interacts with the P orbital of the Oxygen atoms (red dot). There is a strong double

exchange interaction between the Mn and O. Exchange interactions prefer a ferromagnetic state, so the created spins are aligned.

This leads to a ME when an applied field causes a sudden change in that magnetization. Figure 2.14 shows an example of this effect in Lead, Zirconium, Titanium / Lanthanum, Strontium, Manganese Oxide (PZT/LSMO) [98].

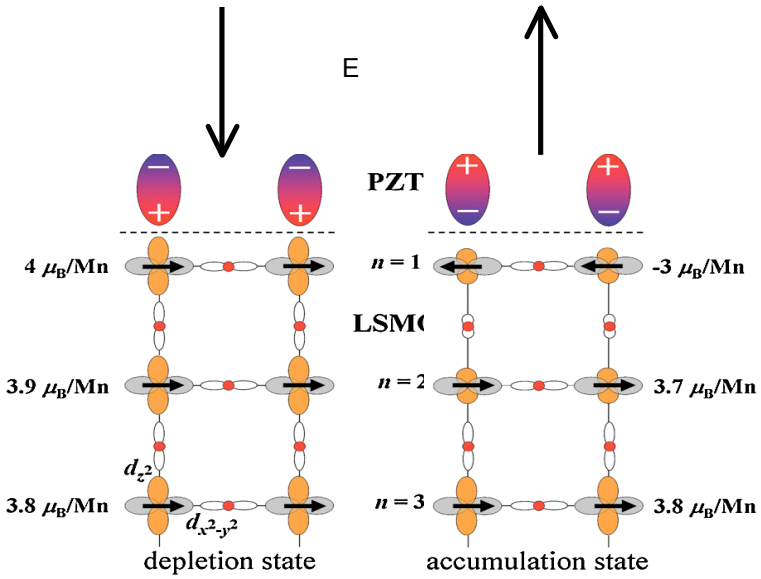

Figure 2.14: Example of two-phase ME due to the overlap between atomic orbitals in PZT/LSMO. The applied field changes the polarization of PZT, which either attracts or repels the orbital electrons in the LSMO, resulting in a change in magnetization of the LSMO layer [98].

In a multilayer material, the magnetic properties are due to the ferromagnetic metal film. By symmetry, when the material is in a paraelectric state the magnetic moments of the metal atoms are the same at the top and bottom surfaces. When a field is applied, the ferroelectric displacements break the symmetry between the surfaces, causing the magnetic moments to change, creating a ME.

This is due to the orbital-resolved local density of states (DOS). The applied electric field polarizes the ferroelectric layer, and makes metal atoms move away from one interface and towards the other. This causes the bond length between the atoms to be shorter, and leads to the overlap of the orbitals of these atoms to be stronger at one interface than at the other. This causes the minority-spin bounding state to be more populated at the interface where the overlap is stronger. Therefore, ferroelectric changes enhance the induced magnetic moment at one interface, but reduces the magnetic moment at the other [99]. A graph of the charge carriers at the surfaces is shown in Figure 2.15 [100].

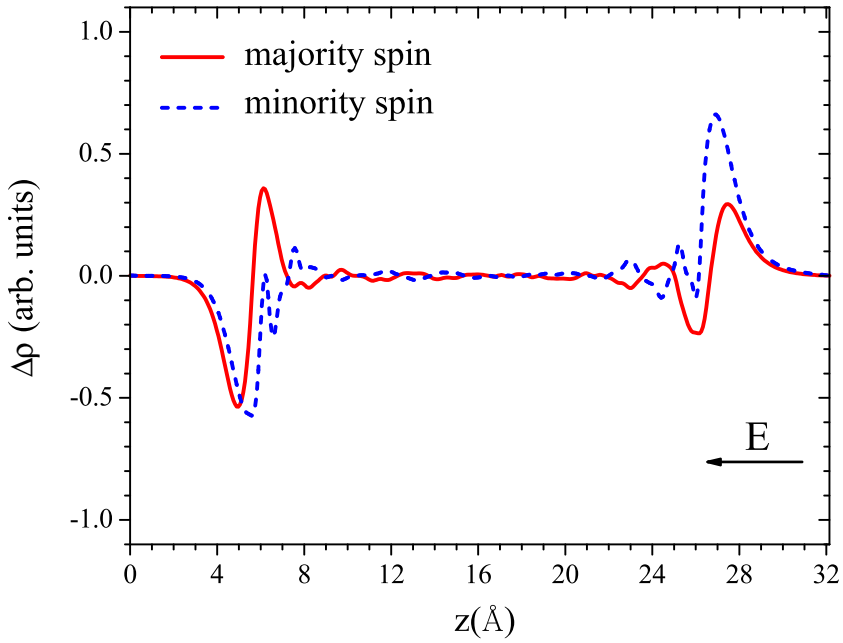

Figure 2.15: Graph of charge carriers at the surfaces of two ferroic layers. It can be seen that the different surfaces have different charge carriers [100].

Figure 2.16 is a density of states graph for the same surfaces, highlighting the difference in charge carriers at each surface.

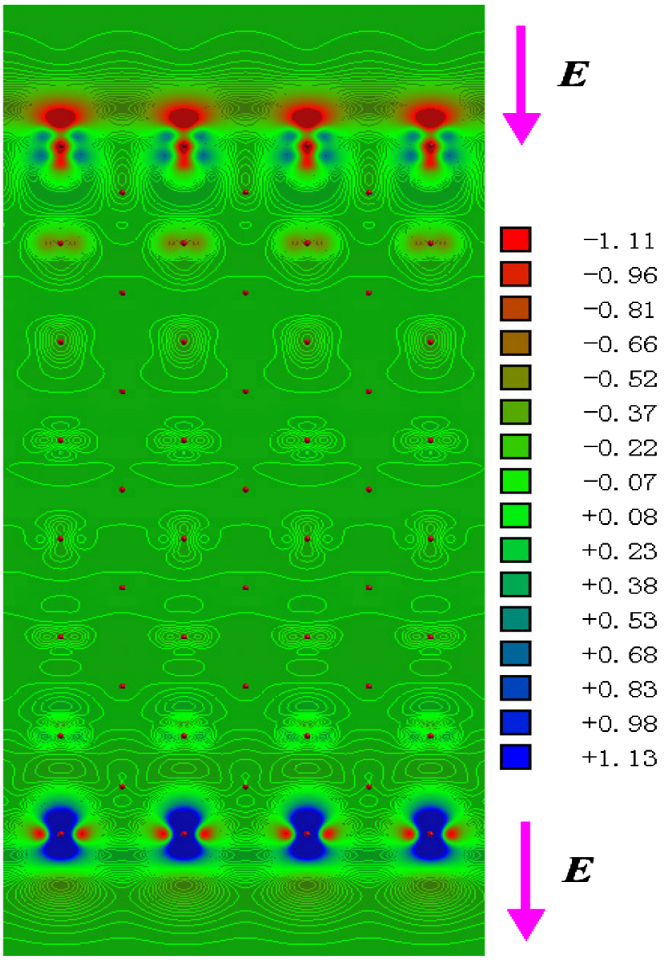

Figure 2.16: The induced spin charge densities of state in arbitrary units. The red and blue spots represent the different charge carriers at the different surfaces [100].

Two-phase ME is qualitatively different from the single-phase ME. Single-phase is a linear function of the applied field and is a volume effect. Two-phase ME is non-linear and is an effect due to the interaction of the interfaces between ferroic layers.

CHAPTER 3. EXPERIMENTAL METHODS

3.1 Deposition Techniques

For this work, multiferroic materials were formed by creating a heterostructure sample, a two-phase ME material. To create these heterostructures, multiple techniques were utilized. The heterostructures consisted of multiple layers of metallic thin films and PVDF polymer. Magnetron sputtering was used to deposit base copper layers. To deposit PVDF layers with the correct, ferroelectric phase, a Langmuir-Schaefer dipping technique was employed. Finally, to create iron and aluminum films, resistive thermal evaporation was performed.

3.1.1 Magnetron Sputtering Deposition

The sputtering process is a form of physical vapor deposition, or PVD. In the sputtering process, energetic ions are directed towards a target of solid material. Atoms in this target are ejected by the ions and are deposited on a substrate.

The set-up for standard sputtering has a target of certain material, and a substrate situated above the target. The target and substrate system is placed inside a vacuum chamber, so that there is no interaction with atoms from gases in the air. Once in the vacuum, gas is introduced into the system. This gas has a very low pressure, in the milliTor range. The ions used to eject the atoms come from this introduced gas.

The target is connected to a power source and acts as a cathode. The substrate is grounded and acts as the anode of the system. This runs high energy through the target, from which the ionized gas is created. Since high energy flows through the target, it needs to be cooled as well. The target is connected to a water-cooling system to protect it from overheating and cracking or breaking. Figure 3.1 shows the target system, with power and water-cooling connections [101].

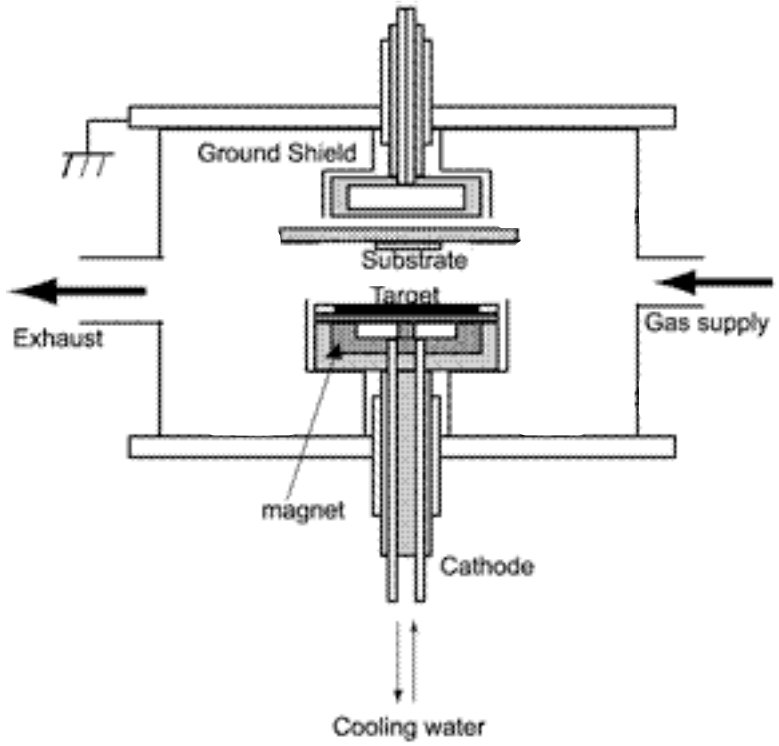

Figure 3.1: Sputtering target with connections. Argon gas supplied to the chamber is ionized, and the atoms hit the target, depositing atoms on the substrate [101].

The sputtering process occurs due to the exchange of momentum during collisions between the atoms of the material and the ions. The high-energy ions, typically at least 100 eV, created from the cloud of gas collide with the close-packed atoms of the target

material. These atoms are pushed around in the material. Eventually, some of the atoms near the surface of the target are ejected from the surface, cross the vacuum and impact with the substrate, where they are deposited. Figure 3.2 shows a diagram of the ions entering the material and ejecting target atoms [102].

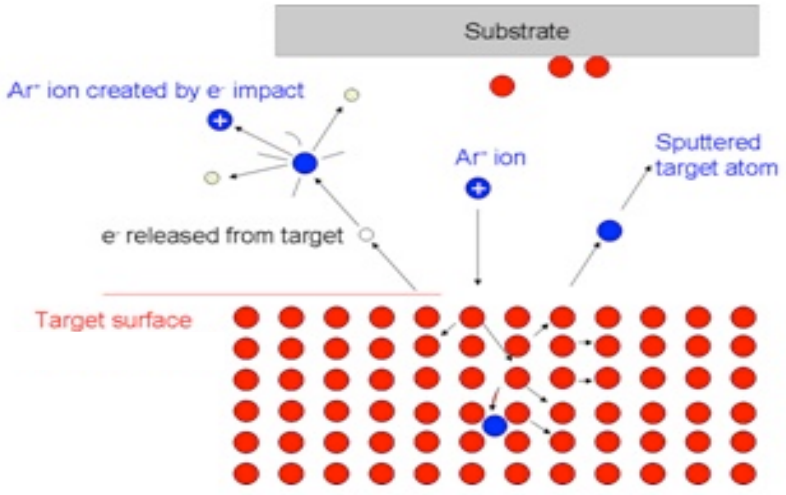

Figure 3.2: Process of ion collision and atom ejection in sputtering deposition. Argon ions cause a target ion to be ejected due to conservation of energy and momentum [102].

These ejected atoms have are high-energy, which causes them to stick to the substrate. The energy, however, is low enough that it doesn't eject atoms from the substrate. This type of deposition process creates thin films of the target material on the substrate. These deposited films have the same composition as the source material with a low impurity rate. This low impurity rate is due to the speed at which the process takes place.

For this work, the sputtering target used was copper. Argon gas was introduced to the vacuum chamber using a flow controller. A voltage of 0.204 V was applied to the controller, which corresponds to an argon pressure inside the vacuum chamber of 1 mTorr. The power source supplied 50 W of power to the sputtering target (380 V, 0.131 A). A crystal thin film thickness monitor was used to calibrate the deposition rate of copper at the above conditions, and that was found to be 2.64 Å/s. The copper films deposited on the substrates were used as electrical contacts throughout the experiment.

3.1.2 Langmuir-Schaefer Polymer Deposition

PVDF polymer films were deposited on Si (100) substrates using Langmuir–Schaefer film fabrication. The Si substrates were cleaned ultrasonically using acetone, isopropyl alcohol, and finally DI water in order to remove the contamination from the surface. A PVDF solution was made by dissolving it in an organic solvent such as acetone with a concentration of 0.05% by weight. A commercial PVDF transfer membrane from Thermo Scientific was cut into 8 mg pieces. One 8 mg piece was dissolved into 20 mL acetone for 2 h at a temperature of 80 °C. 5 µL drops of the solution were then put on the surface of DI water at a coverage rate of 1 drop per 1.5 cm_2 of surface. The films were prepared using the Langmuir–Schaefer method. The Si substrate was dipped through the solution, into the DI water, parallel to the liquid surface. The substrate was then slowly removed from the solution at a small angle [103]. The film was allowed to dry completely before dipping again. Each dip deposited one monolayer (ML) of PVDF film on the substrate, each ML 1.75 nm thick.

3.1.3 Thermal Evaporation

Using the Langmuir-Schaefer method, β phase PVDF is deposited on the substrate. As mentioned previously, magnetron sputtering can be used to deposit metallic thin films. However, due to the high energy and speed of the sputtered atoms, the PVDF layer will be destroyed when a film is sputtered on top of it. Iron can be sputtered below the PVDF if necessary, but doing so above the PVDF will ruin the sample. To avoid this problem, a different way to deposit iron and aluminum on top of the PVDF is needed. To keep the film layers consistent, all iron layers were deposited in the same way. This process is resistive thermal evaporation.

Resistive thermal evaporation is one of the most commonly used metal deposition techniques. In this process, a solid material (pure metal, compound, etc.) is heated to a high temperature until the material vaporizes. The atoms in the vapor travel through a vacuum and hit a cooled substrate, where they cool and form a solid thin film. The heating of the material is obtained by passing a large current through a filament container that has a finite resistance. These containers are usually in the shape of a boat, basket, or crucible, and consist of a resistive wire coated in a ceramic material. Figure 3.3 shows a schematic diagram and picture of a basket type container [104]. The choice of the filament container is determined by the evaporation temperature and its' inertness to reactions with the evaporant. Since the container is used to perform the heating, this method is often referred to as indirect thermal evaporation.

Once the material is evaporated, the vapor undergoes collisions with any gas molecules in the deposition chamber. Because of this, a fraction of the vapor atoms are scattered within a given distance during their movement through the ambient gas in the

deposition chamber. At room temperature, the mean free path for air is approximately 45 cm at a pressure of 1 x 10^{-4} torr. As the pressure is lowered, the mean free path for air increases, up to 4500 cm at 1 x 10^{-6} torr [105]. To ensure that vaporized atoms do not collide with air molecules, the distance from the evaporation container to the substrate must be much less than the mean free path for air. In this particular deposition chamber, the distance from container to substrate is approximately 50 cm. Therefore, a pressure less than 1 x 10^{-5} torr is necessary to ensure that the evaporated material has a straight line path to the substrate. A good vacuum is also necessary to reduce contamination in the deposited materials [106].

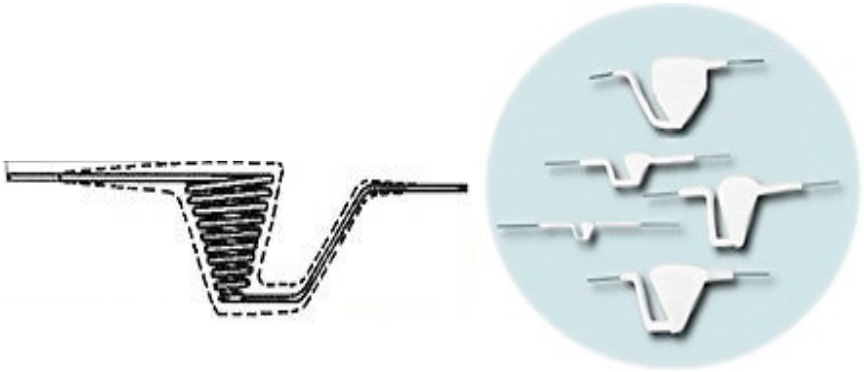

Figure 3.3: Schematic diagram of filament basket, and a sketch of the basket [106].

Figure 3.4 shows a simple schematic of a thermal evaporation system [107]. In this work, a dual evaporator system was used. Using electric feedthroughs, two containers were inserted into the vacuum chamber and connected to external sources. The containers used were both Midwest Tungsten Service alumina coated basket filaments. Two types of materials were to be evaporated during this experiment: iron and aluminum. One basket was dedicated to each material to eliminate cross contamination.

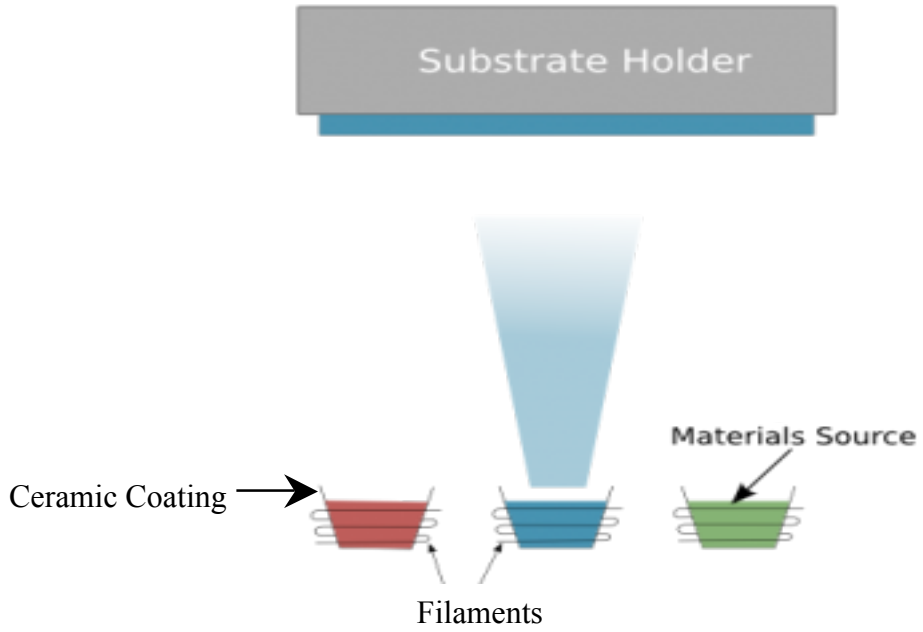

Figure 3.4: Schematic diagram of thermal evaporation. The filaments are heated using a current. The ceramic coating gets hot, causing the source material to evaporate and deposit on the substrate [107].

To perform the evaporation, pure, thin wire of the desired material was placed in the basket. The electric feedthrough ends were then connected to a power source. Current was run through the basket until the wire material melted, creating the targeted vapor. Prior to inserting a substrate, a crystal film thickness monitor was used to calibrate the deposition. The monitor was placed above the basket, and the current from the external source was increased until evaporation occurred and material was deposited on the monitor. This process was repeated several times, and each time a total thickness calibration was performed to determine the deposition rate.

When samples were placed in the chamber, the power source was run at the calibrated current in order to control sample thickness. For iron, with a melting temperature of 1811 K, a current of 12 A was necessary to initiate evaporation. This

current corresponded to a deposition rate of 0.427 Å/s. For aluminum, with a melting temperature of 934 K, an applied current of 9 A gave a deposition rate of 0.342 Å/s.

3.2 Ferroelectric Testing

To fully examine the ferroelectric properties of the PVDF polymer, a device was needed to run the polarization versus electric field tests. In these experiments, all ferroelectric tests were performed using a Radiant Technologies Precision RT66B ferroelectric testing hardware, as shown in Figure 3.5, and the accompanying Vision Data Management software. The Precision RT series testers consist of an arbitrary waveform generator (AWFG) to simulate the sample and an electrometer to capture the sample's electrical response.

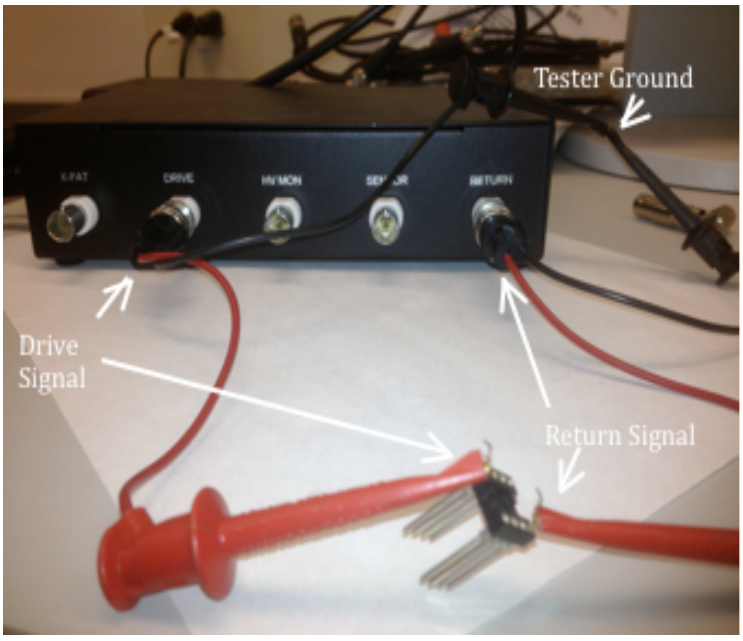

Figure 3.5: Precision RT66B testing device.

The electrometer in the device is a device that measures the charge across a sample over a given amount of time, using a virtual ground circuit, which will be discussed in more detail in the sections ahead. The AWFG and data capture functions for this device are executed using the company's software, as shown in Figure 3.6 [108].

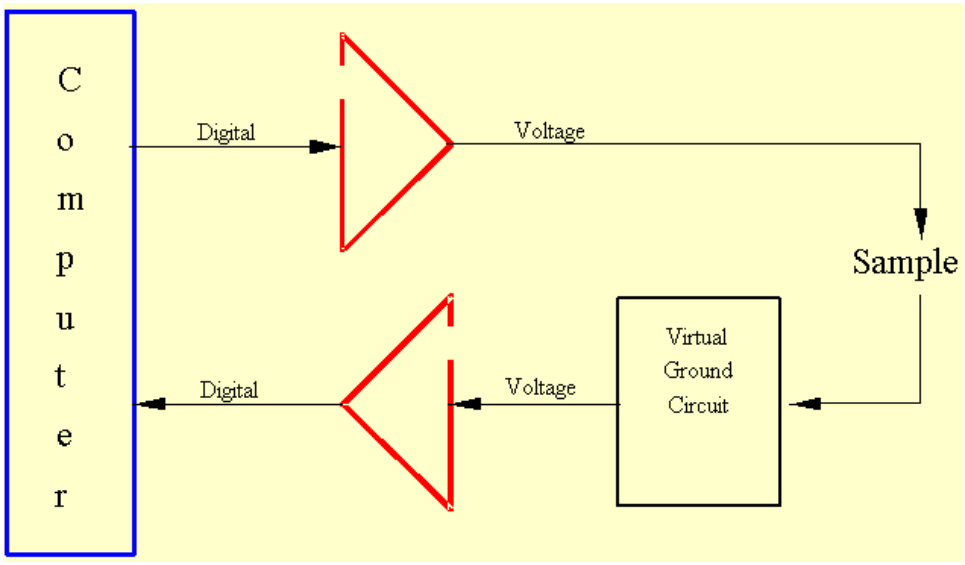

Figure 3.6: Simplified RT66B device schematic [108].

This simplistic design allows the tester to be extremely reliable. The tester relies on the computer and software to send all signals to the device, thus controlling all timing. This causes a delay in sending and receiving the data, but the device results are still within 1% of assigned values [108]. As long as the device is allowed to run a full test uninterrupted, that accuracy value will be valid.

3.2.1 Polarization Measurements Using Precision RT66B

Using this device, the sample can be considered a Voltage-to-Charge converter. For this setup, the sample is considered to have infinite impedance between the input and

output connections. This means that the response signal does not show values of the DRIVE voltage. The RETURN circuit can see a charge coming out of the sample, but that part of the circuit is not related to the DRIVE voltage sent by the device.

The circuit used to measure the charge on the sample uses a current amplifier followed by an integrator. The output of this integrator is sent as a voltage that is directly related to the charge on the sample. On a typical Hysteresis test, a signal is sent to the sample, and the output from the sample runs into the RETRUN port. From here, it runs through the circuit, and a charge value is output. The circuit diagram for this tester can be seen in Figure 3.7 [108].

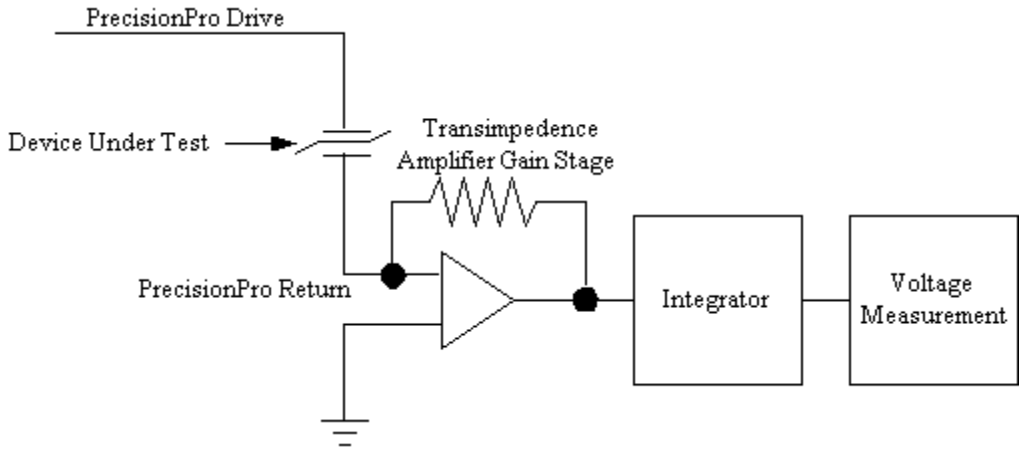

Figure 3.7: Circuit diagram for RETURN port of RT66B testing device [108].

When a test is run, the output voltage is multiplied by the capacitance of a reference capacitor to get the total charge across the sample at every point of measurement. This means that there are no manipulations on the charge data, so this is the true charge across the sample. This charge is plotted against the DRIVE voltage, which is stored in a separate circuit. To get a PE loop, the voltage can simply be

converted to electric field. In all these cases, as seen in Figure 3.7, the RETURN is connected to a ground, so the voltage measured at the DRIVE is the actual voltage across the sample.

In the Virtual Ground Circuit of the device, the tester measures data by measuring current flow through a sample, rather than voltage across the sample. As mentioned earlier, this current is then converted to a voltage based on an amplifier and reference resistors. The following will explain the Virtual Ground Circuit in more detail.

In this type of circuit, a parasitic capacitor is connected in parallel to the RETURN circuit previously shown. Figure 3.8 shows the new circuit schematic, with a parasitic capacitor added. The reference capacitor and RETURN port are connected together, and never allowed to gain a voltage greater than zero. Any voltage is collected by the parasitic capacitor and does not go to the RETURN. All current that flows through the sample is transferred directly to the integrator circuit. This type of grounding circuit, using current instead of voltage, prevents voltage from being sent back through the sample, thus eliminating a chance for error or inaccurate measurements.

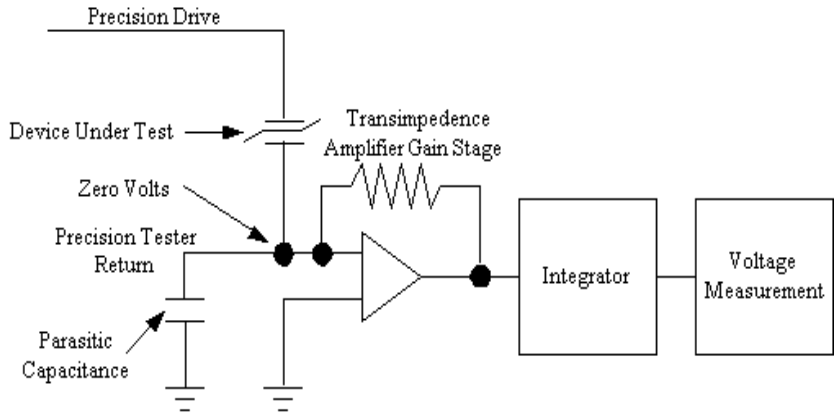

Figure 3.8: Circuit with parasitic capacitor used to ground the internal circuit.

Finally, this Virtual Ground and RETURN circuitry is added into a simple circuit with the reference capacitor, as shown in Figure 3.9.

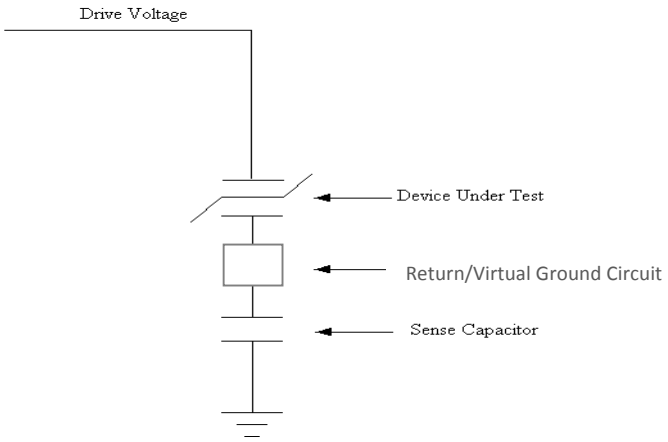

Figure 3.9: Final simplified circuit diagram.

3.2.2 Tester and Software Operation

Using the Vision Data Management software, ferroelectric tests can be run to look for hysteresis in the PE loops. Figure 3.10 shows the software for a hysteresis test. The software, with a charge signal from the tester, will calculate polarization using the charge and the area of the sample. Thus, the sample area can be input before a test is run. Also, the maximum applied drive voltage (and the corresponding maximum electric field), can be controlled from the dialog box. The final parameter to control is the period of the hysteresis loop, or the frequency at which the voltage is switching. By running the program, a drive voltage will be sent to the previously described circuit, and the measurements will be taken. A complete run can take from 50 ms to 30 seconds. The minimum time is based on the number of points collected, which is 50 points for 50 ms, enough to give enough detail about the loop.

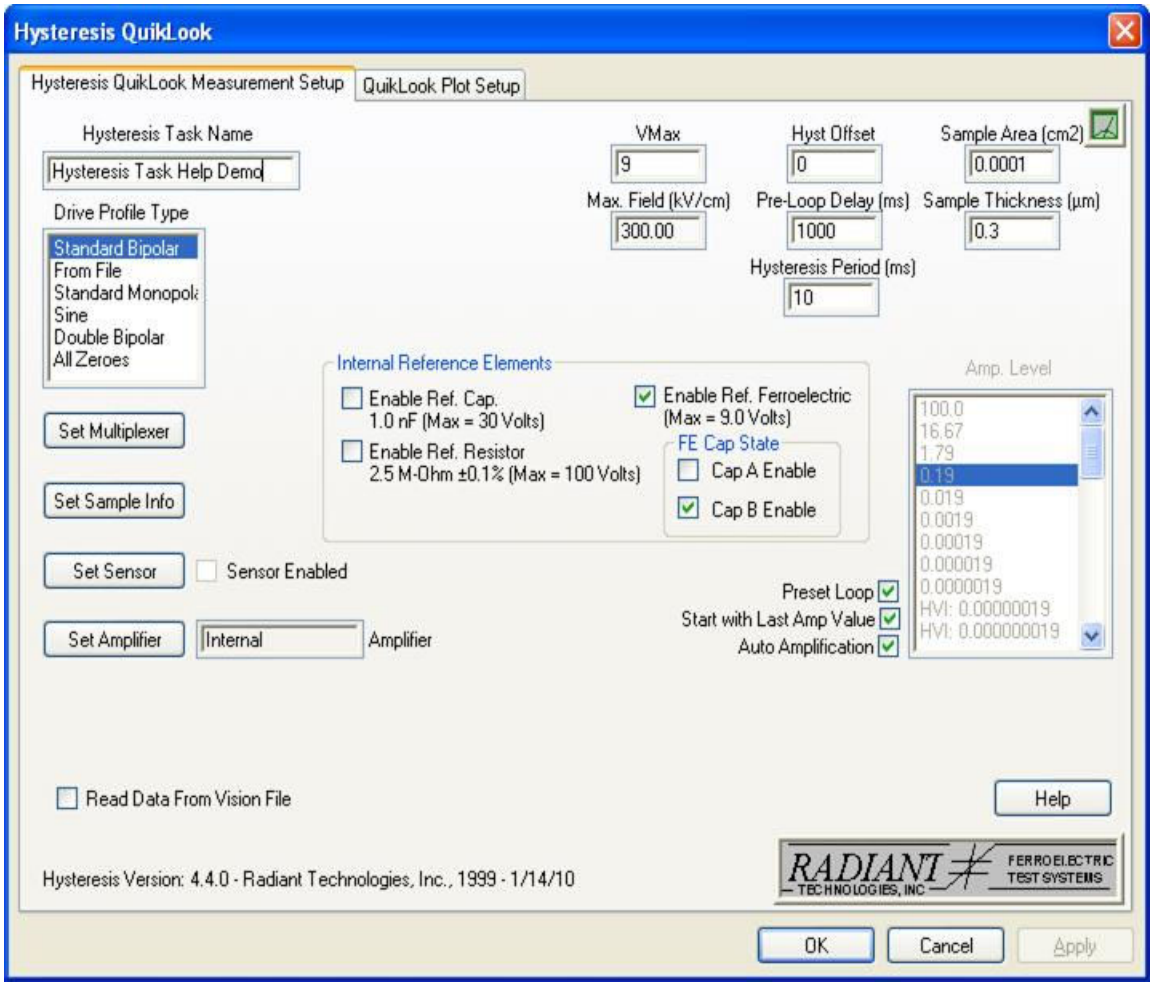

Figure 3.10: Sample Hysteresis test setup using Vision software.

3.3 X-ray Absorption Fine Structure Theory

3.3.1 Introduction

X-ray absorption fine structure (XAFS) is a type of spectroscopy that utilizes X-rays in order to investigate different physical and chemical characteristics of materials at an atomic scale. XAFS operates just below and above the binding energy of a particular core electronic level of a particular atomic class, therefore making it element specific.

The basic theoretical predictions of XAFS were explained in terms of quantum interference effects back in the 1930's. However, it did not become a feasible experimental tool until two events occurred: Stern, Sayers, and Lytle developed a theory on the necessary physical aspects leading to the standard XAFS equation, and they then proposed a simple method of data analysis [109]. Today, the amount of information about a material that can be gathered from a single XAFS spectrum is greater than most other analysis techniques.

XAFS can be defined as a modulation of X-rays absorbed by atom species dependent on the material's present structure, including lattice structure, distortion, physical state, and chemical state [110]. The information obtained for an XAFS scan, including the coordination number, the distance, the distortion states, and the surroundings of the selected element, can be determined from the experimental data and derivative calculations. Hence, XAFS provides a straightforward approach to determining the atomic structure and the chemical and physical states of a sample atomic species. XAFS is useful and routinely used in the fields of physics, materials science, chemistry, biology, and environmental science.

In practice, XAFS is a practical and relatively simple measurement, which requires an X-ray source that is intense and tunable, such as synchrotrons [111]. In fact, the theoretical and experimental advances in XAFS are closely tied to the advances in synchrotron sources. XAFS experiments using these sources have minimal requirements in terms of the samples, but provide some advantages since many creation techniques and sample conditions can be used. These advantages include in situ measurements of

chemical processes, high spatial resolution, and extreme temperature and pressure conditions during sample creation.

A reference XAFS scan can be seen in Figure 3.11 [112]. This scan was performed on an iron oxide sample. The energy of incident X-rays is increased, and a graph is produced showing that energy versus the oscillations, which will be explained shortly.

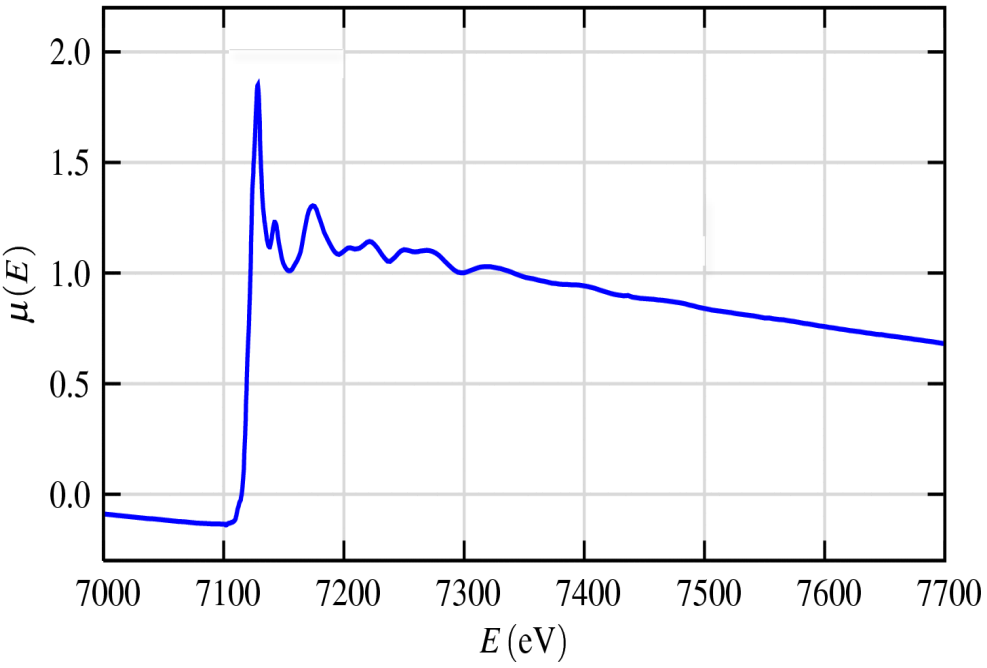

Figure 3.11 Sample XAFS scan for iron oxide. The energy of the incident x-rays is plotted versus the absorption coefficient [112].

Typically, an XAFS scan such as this is divided into two regimes: X-ray Absorption Near-Edge Spectroscopy (XANES) and Extended X-ray Absorption Fine-Structure (EXAFS). XANES can give information about the oxidation state and binding geometry of the absorbing atom, while EXAFS gives information about neighbor

distances and coordination number. Figure 3.12 shows an XAFS scan of $Ge_1Sb_2Te_4$ with these two regimes highlighted [113].

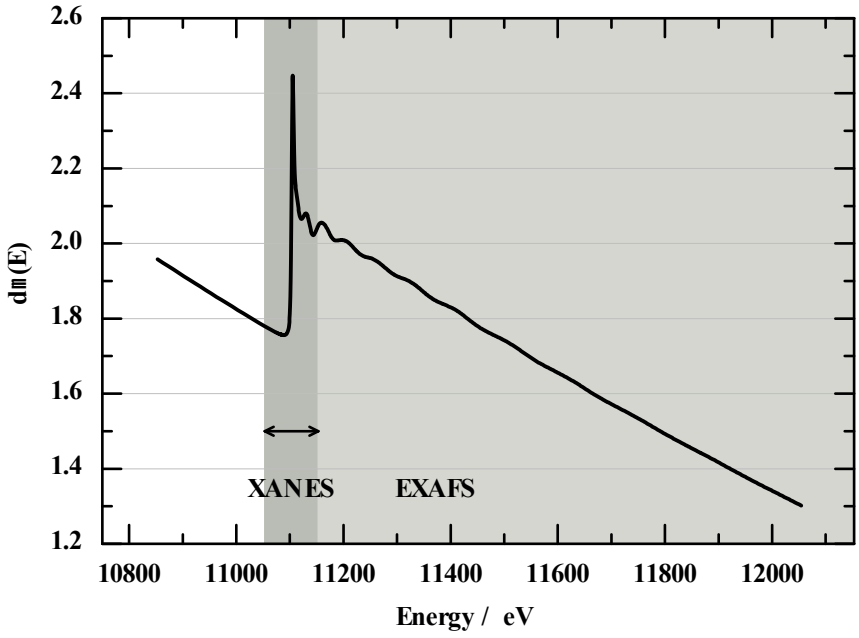

Figure 3.12: Sample XAFS scan for $Ge_1Sb_2Te_4$ showing the XANES and EXAFS regimes [113].

3.3.2 Fundamentals and Equations of XAFS

X-rays are a form of electromagnetic radiation with an energy range of 100 eV to 100 keV, and a wavelength range of 0.01 to 10 nm. Due to the photoelectric effect, incident X-rays are absorbed by most materials. The incident X-ray photon is absorbed by and electron in a tightly bound quantum core level, typically the 1s or 2p level, of an atom.

If the energy of the incident X-ray is less than the binding energy of the material, the core electron will not be excited from the previous quantum state. However, if the

incident X-ray energy is greater than the binding energy of the material, the X-ray is absorbed and the core electron enters an excited energy state, leaving a core hole, or empty electronic level, as shown in Figure 3.13 [114]. The energy from the X-ray above the binding energy is given to the excited photoelectron.

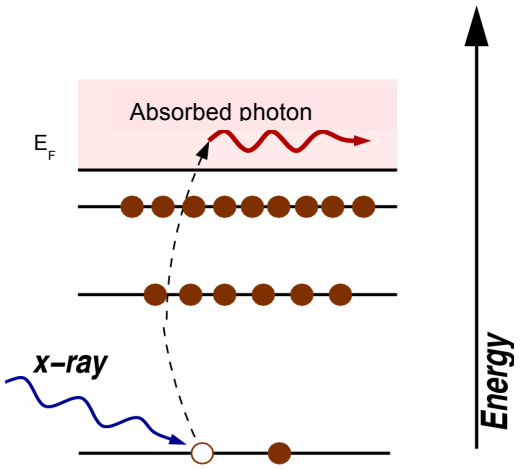

Figure 3.13: Diagram of X-ray absorption.

When X-rays are absorbed, the excited electron and empty hole prefer to return to a stable state rather than staying in the excited state. When a higher level core electron drops into another core hole, a fluorescent X-ray is emitted, such as K_α or K_β radiation. Figure 3.14 [112] shows a diagram of this process.

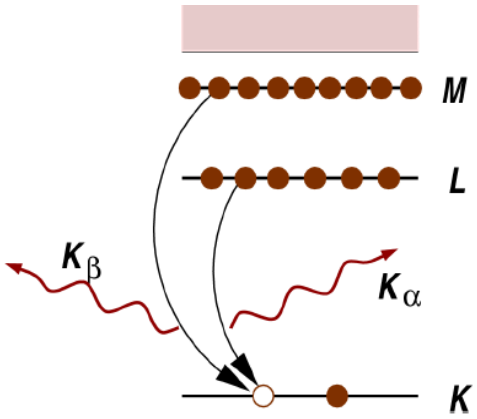

Figure 3.14: Diagram of X-ray Fluorescence.

One of the most important parameters in XAFS studies is the absorption coefficient, μ. From Beer's Law, the probability that an X-ray will be absorbed is described by:

$$I = I_0 e^{-\mu t}, \tag{3.1}$$

where I_0 is the incident X-ray intensity, t is the sample thickness, and I is the intensity of the X-ray transmitted through the material. Figure 3.15 shows a simplified picture of the X-ray interaction with a material.

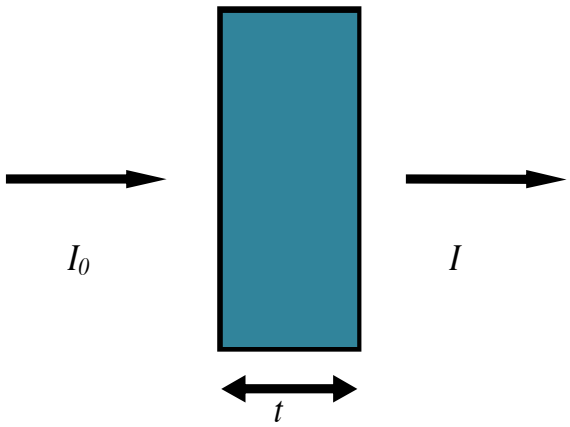

Figure 3.15: Simple schematic of X-ray interaction with a material.

The absorption coefficient above is a smooth function for most X-ray energies and depends on the incident energy E and several properties of the material, atomic number, density, and atomic mass A. It is given by the function [115]:

$$\mu = \frac{\rho Z^4}{AE^3} \tag{3.2}$$

Figure 3.16 shows an example of the coefficient versus energy curves for several different materials [116]. Notice that for the most part, the curves are smooth. However, lead, iron, and cadmium show at least one place where there is a sharp change increase in the absorption coefficient.

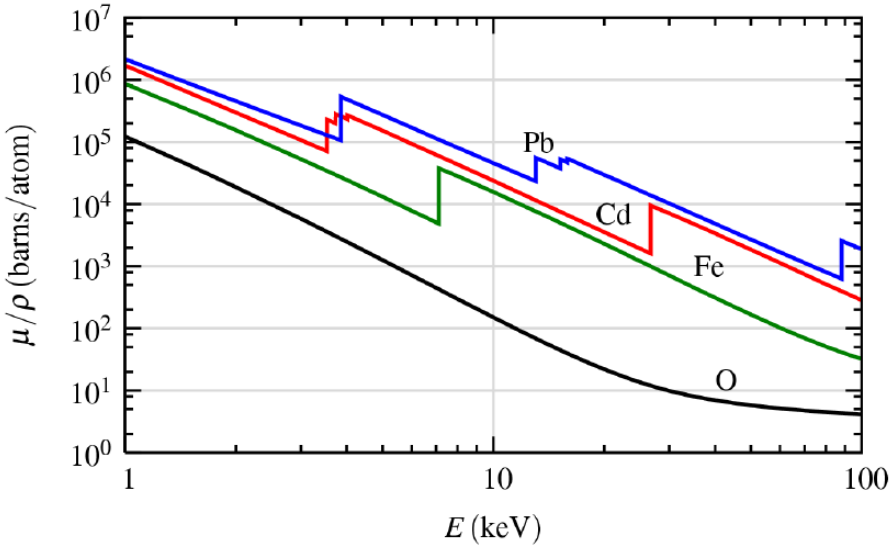

Figure 3.16: The absorption coefficient versus energy curves for lead, iron, cadmium, and oxygen. This shows the different edge steps and the variation in EXAFS oscillations [116].

Those sharp jumps in the absorption coefficient occur at the binding energy of the material. This spike is called an absorption edge, and corresponds to a core electron

moving to the conduction band. XAFS experiments focus on the region just below and above this area, and examine the absorption coefficient as the incident energies increase. There are two ways to measure the behavior of the absorption coefficient for the decay of an electron from an excited state to the core hole. The most common type is the X-ray fluorescence process as described earlier. The fluorescence energies of the emitted photons are specific to the atoms. By analyzing these energies, the type of atoms and the atom concentrations can be found.

To collect an XAFS spectrum, the most widely used method is transmission detection. The absorption is calculated directly by measuring what is transmitted through the sample. Rearranging the previous Beer's Law equation gives:

$$\mu(E) * t = -ln\left(\frac{I}{I_0}\right) \tag{3.3}$$

Using fluorescence, it can be shown that the fluorescence signal is proportional to the absorbance. From this, the EXAFS can be extracted from it and the absorption coefficient can be expressed as:

$$\mu(E) \propto \frac{I_f}{I_0}, \tag{3.4}$$

where I_f is the detected fluorescence signal and I_0 is again the incident X-ray intensity. Figure 3.17 shows the experimental setup for XAFS, showing both the transmission and fluorescence detection.

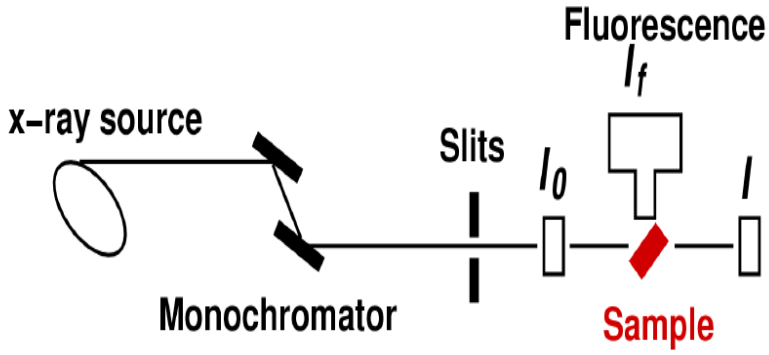

Figure 3.17: Example setup for XAFS measurements. X-rays are directed at a sample, and the incident energy or intensity is measured. Then, the transmitted and fluorescence intensities are measured.

Referring back to Figure 3.11, the sharp peak for the iron oxide sample occurs at the binding energy for the iron 1s electron level, 7112 eV. The oscillations in the signal after the peak are the EXAFS. These energy dependent oscillations above the absorption edge contain the information about the neighboring atoms. So the EXAFS fine-structure function is defined as [117]:

$$\chi(E) = \frac{\mu(E)-\mu_0(E)}{\Delta\mu_0(E_0)} \tag{3.5}$$

Here, $\mu(E)$ is the measured absorption coefficient, $\mu_0(E)$ is the absorption for an isolated atom, and $\Delta\mu_0$ is the jump in the absorption coefficient at the energy threshold E_0.

EXAFS is better expressed in terms of the wave behavior of the absorbed photon rather than the energy. Therefore, it is more common to express EXAFS measurements in the wave number, k, region. The relationship between energy and k is given by:

$$k = \sqrt{\frac{2m(E-E_0)}{\eta^2}}, \tag{3.6}$$

where E_0 is the absorption edge energy, and m is the electron mass. The primary quantity then for EXAFS is $\chi(k)$, the oscillations as a function of photon wave number, often referred to as "EXAFS". An EXAFS graph for iron oxide, showing only the oscillatory region, is shown in Figure 3.18 [112].

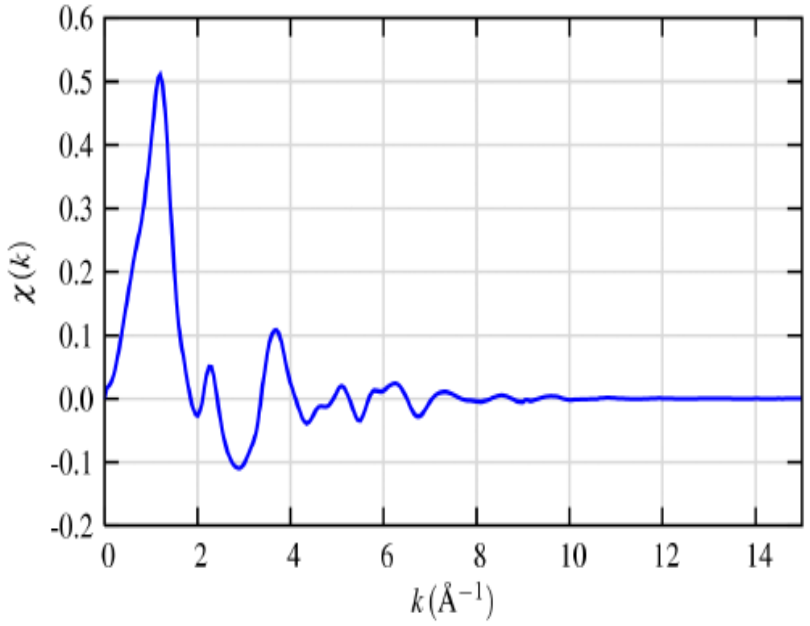

Figure 3.18: Isolated EXAFS for iron oxide. This graph shows the oscillations, called EXAFS, as a function of wave number k [112].

Commonly, EXAFS is oscillatory and decays with k. Occasionally, for clarity, the EXAFS function is multiplied by a power of k to magnify the oscillations. This is shown in Figure 3.19 [112].

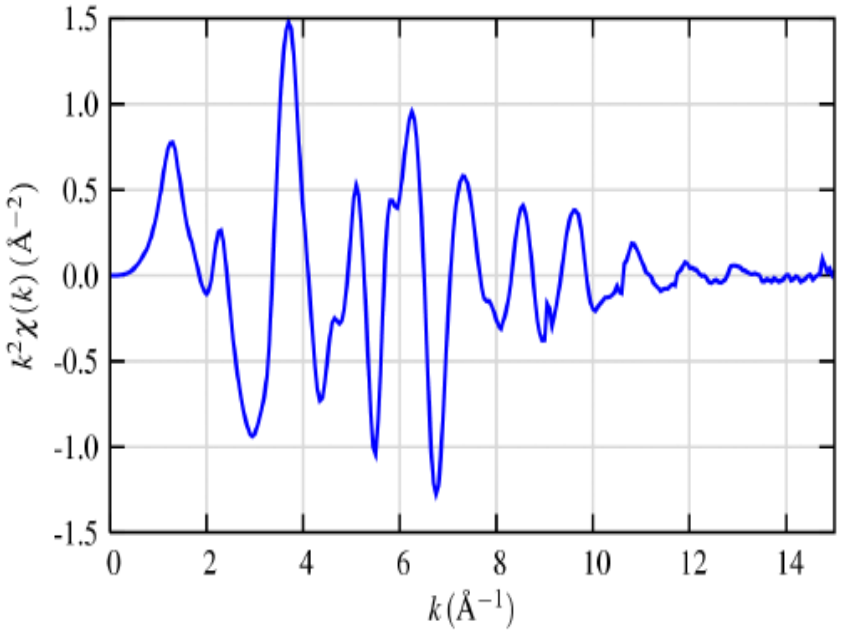

Figure 3.19: k-weighted isolated EXAFS for iron oxide. Here, the EXAFS measurement is multiplied by a factor of k in order to magnify the oscillations [112].

As previously mentioned, two methods were developed to collect EXAFS spectra. For the transmission method, a monochromator is used to select a small wavelength range and step-scanning through the required incident energies. A detector is placed after the sample to measure the transmitted intensity. Figure 3.20 shows a schematic of a transmission EXAFS measurement.

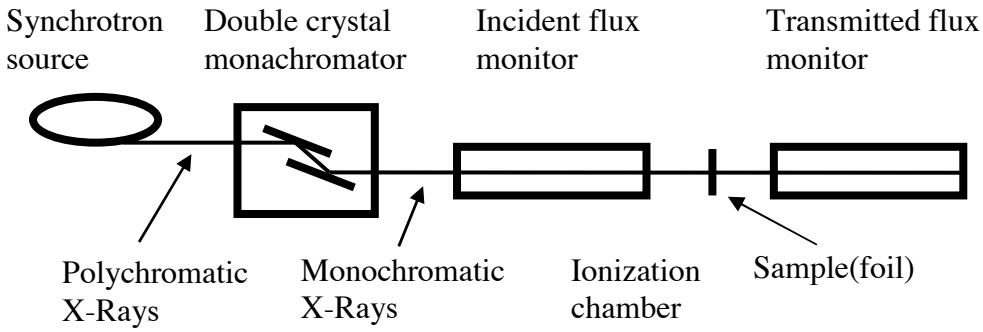

Figure 3.20: Schematic of transmission EXAFS. The intensity detector here is placed in a direct line with the incident x-rays, and is located after the sample.

The other method is the fluorescence measurements. In this case, the sample is normally set at a 45° to the incident beam. The fluorescence signal is emitted spherically from the sample. These detectors are usually solid state, cryogenically cooled devices that have a maximum count rate above which they won't work. Slits are used to control the amount that hits the detector if the count is above the maximum. Figure 3.21 shows a schematic of a fluorescence experiment.

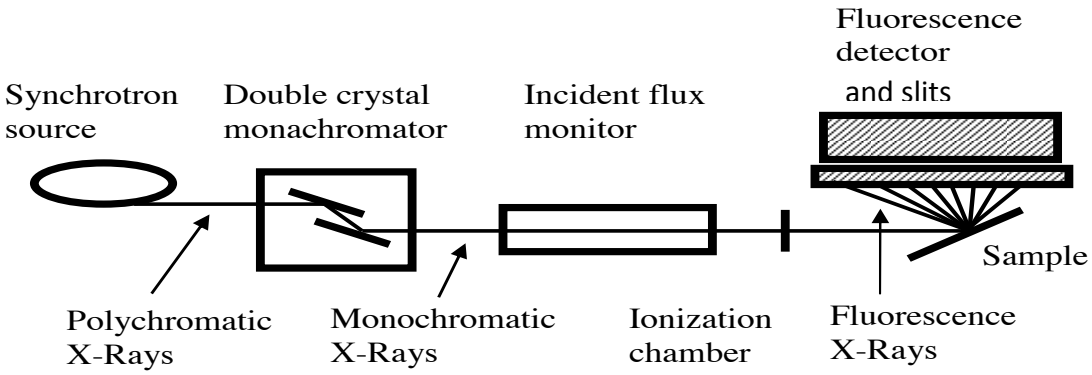

Figure 3.21: Schematic of fluorescence EXAFS. Here, the fluorescence detector is placed at a 90 degree angle to the incident x-rays, and the sample is at a 45 degree angle to both.

In this thesis, all EXAFS spectra were collected at the Argonne Advanced Photon Source (APS), Sector 12, Bending Magnet Line 12-BM-B. Figure 3.22 shows a picture of the end station for the beamline [118]. This experimental setup contains detectors capable of using both transmission and fluorescence methods. The incident X-rays come from the synchrotron from the right hand side of the photo, with the I_0 detector marked. The transmission detector is marked as I_2, with the solid-state fluorescence detector shown.

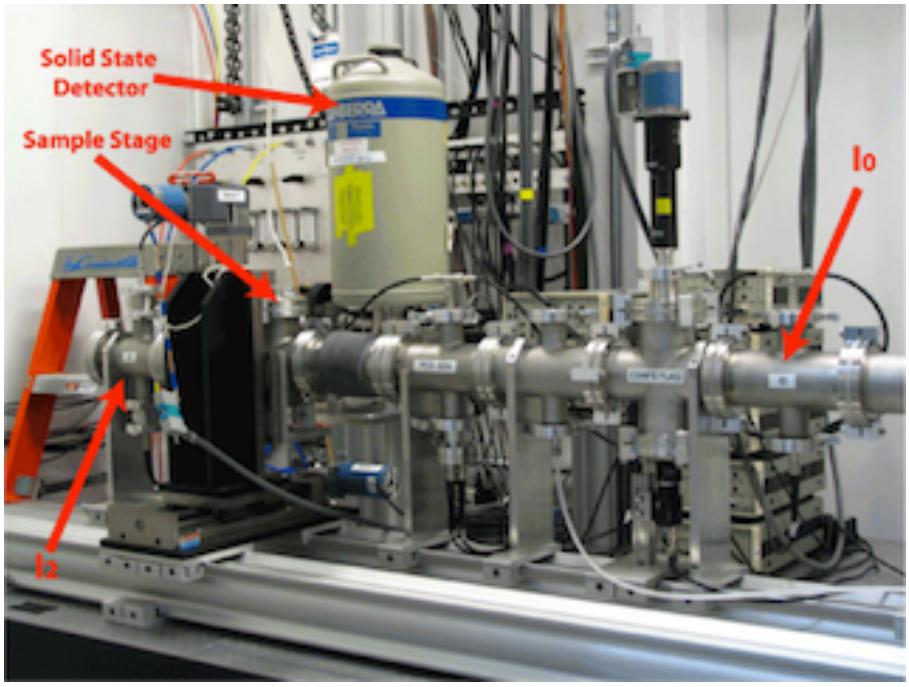

Figure 3.22: Photograph of Argonne APS Sector 12 EXAFS end station. The incident detector is labeled as I_0, the transmitted detector is I_2, and the solid state detector is used for fluorescence measurements [118].

The oscillations in $\chi(k)$ due to different materials and structures can be described according to quantum theory. As previously discussed, when an X-ray with energy above the binding energy hits a core level electron, the electron is excited into the conduction

band and a photo-electron with wave number k is created and propagates from the atom. When a neighboring atom exists in the material, the photo-electron backscatters from the neighboring atom atoms and returns to the core atom. Meanwhile, the backscattered photo-electron influences the absorption coefficient of the core atom, and can be calculated using quantum theory. Figure 3.23 [119] shows an example of backscattering of the photo-electron. The black lines represent the emitted photo-electrons, and the red represents the backscattering.

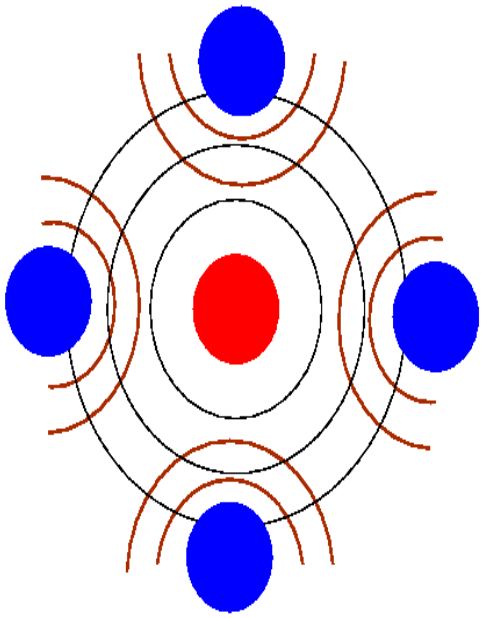

Figure 3.23: Backscattering of a photo-electron. The black lines represent photo-electrons emitted by the red central atom, the red lines represent the scattered photo-electrons off of neighboring atoms [119].

X-ray absorption is a transition between a core level and an excited state, so it can be described using Fermi's Golden Rule:

$$\mu(E) \propto |\langle i|H|f\rangle|^2, \tag{3.7}$$

where $\langle i|$ represents the initial state of the core electron, H is the interaction term, approximately 1, and $|f\rangle$ is the final state after backscattering. Obviously, the initial state is not altered by a backscattered photo-electron, but the final state is. This term can be rewritten as two terms, on for an unaltered core electron, one altered due to the backscattering as:

$$|f\rangle = |f_0\rangle + |\Delta f\rangle \tag{3.8}$$

Therefore, the absorption coefficient can be expanded as [120]:

$$\mu(E) \propto |\langle i|H|f\rangle|^2[1 + \langle i|H|\Delta f\rangle]\frac{\langle f_0|H|i\rangle}{|\langle i|H|f_0\rangle|^2} + C.C. \tag{3.9}$$

where C.C. represents the complex conjugate.

Comparing this to the previously mentioned relationship between the absorption coefficient and EXAFS, we get:

$$\mu(E) = \mu_0(E)[1 + \chi(E)] \tag{3.10}$$

The initial absorption coefficient occurs when the final state is simply f_0, which depends only on the core atom and not the neighboring atoms. So EXAFS can be given as [121]:

$$\chi(E) \sim \langle i|H|\Delta f\rangle \sim \langle i|\Delta f\rangle \tag{3.11}$$

If we consider the initial state of the core atom as a delta function, H can be recognized as e^{ikr}, and the final state is the wave function of the scattered photo-electron. Now, we can write EXAFS as [122]:

$$\chi(E) \sim \int \delta(r) e^{ikr} \psi_{scatt}(0) = \psi_{scatt}(0) \tag{3.12}$$

So, simply stated, EXAFS is proportional to the amplitude of the scattered photo-electron. Now, we can build a simple model for three photo-electron waves: 1) leaving the core atom, 2) scattering from a neighboring atom, and 3) returning to the core atom. Considering these as spherical waves, $\psi(k,r) = \frac{e^{ikr}}{k*r}$, travelling a distance R to the neighboring atom, we obtain [123]:

$$\chi(E) \sim \psi_{scatt}(k, r = 0) = \frac{e^{ikR}}{k*R}\left[2k * f(k)e^{i*\delta(k)}\right]\frac{e^{ikR}}{k*R} + C.C. \quad (3.13)$$

where the neighboring atom gives the amplitude f(k) and phase shift δ(k) to the scattered photo-electron. These scattering properties are a function of the atomic number of the neighboring atom, Z. Combining previous terms and the complex conjugates, we get a real function for a single scattering atom of:

$$\chi(E) = \frac{f(k)}{k*R^2} sin[2k * R + \delta(k)] \quad (3.14)$$

If there exists N neighboring atoms, with a defined thermal disorder of σ^2, this becomes:

$$\chi(E) = \frac{Ne^{-2k^2\sigma^2} f(k)}{k*R^2} sin[2k * R + \delta(k)] \quad (3.15)$$

Of course, actual materials can have different types of neighboring atoms around the core absorbing atom, located at different distances. So all contributions need to be considered [124].

$$\chi(E) = \sum_j \frac{N_j e^{-2k^2\sigma^2} f_j(k)}{k*{R_j}^2} sin\left[2k * R_j + \delta_j(k)\right] \quad (3.16)$$

In this equation, the j terms represent the individual coordination shell of identical atoms at approximately the same distance from the core atom. This equation neglects contributions from inelastic scattering due to other sources, since a photo-electron in an XAFS experiment must have the same energy after scattering (i.e. must be elastic).

One characteristic of XAFS is that the photo-electron has to scatter and return to the core atom before the core hole is filled by an excited state decay. So to account for both inelastic scattering and the core hole lifetime terms in EXAFS, use a wave function of a damped spherical wave:

$$\psi(k,r) = \frac{e^{ikr}e^{-\frac{2r}{\lambda(k)}}}{k*r}, \tag{3.17}$$

where λ is the mean free path of the photo-electron, or the average distance travelled before inelastic scattering occurs or the core hole is filled.

We can now update the EXAFS equation to include the mean free path. That equation now becomes [125]:

$$\chi(E) = \sum_j \frac{N_j e^{-2k^2\sigma^2} e^{-\frac{2R_j}{\lambda(k)}} f_j(k)}{k*{R_j}^2} sin\big[2k*R_j + \delta_j(k)\big]. \tag{3.18}$$

Finally, another neglected term is the amplitude reduction due to the relaxation of all other electrons in the absorbing atom to the core hole. This amplitude is [126]:

$$S_0^2 = \left|\left\langle \Phi_f^{N-1} \middle| \Phi_0^{N-1} \right\rangle\right|^2. \tag{3.19}$$

Here, the first term accounts for all other (N-1) electrons that will relax to the unexcited electrons in the second term. Adding this term, we get the final equation for EXAFS [127]:

$$\chi(E) = \sum_j \frac{N_j S_0^2 e^{-2k^2\sigma^2} e^{-\frac{2R_j}{\lambda(k)}} f_j(k)}{k*{R_j}^2} sin\big[2k*R_j + \delta_j(k)\big]. \tag{3.20}$$

If the properties of the neighboring atoms, including f, δ, and λ are known, the distance to the neighboring atom R and the coordination number N can be determined.

CHAPTER 4. RESULTS AND DISCUSSION

4.1 PVDF Ferroelectric Property Measurements

A series of samples with different numbers of ML were prepared using the Langmuir-Schaefer method described earlier. In order to characterize the electric properties of the sample, magnetron sputtering was used to deposit a copper layer, to be used as an electric lead on top of the silicon substrate. The PVDF was then deposited using the Langmuir-Schaefer method. All samples were then annealed to facilitate crystallization of the films. Finally, the samples were put into a high vacuum chamber and a small area of aluminum was thermally evaporated over the films to act as a second electric lead.

Two different techniques were used to analyze the properties of the PVDF film. X-ray diffraction using a Siemens D-5000 diffractometer (CuKa radiation) was used to analyze the crystallization of the samples annealed at various temperatures. A Radiant Technology Precision RT66B tester was used to measure the polarization versus electric field hysteresis loops of the films. The samples used for the ferroelectric hysteresis study varied in thickness from 17 nm to 70 nm. We have performed systematic measurements on these samples by varying the electric field frequency from 2 Hz to 20 Hz. Similar measurements were also conducted for different maximum electric field.

In order to improve the crystallization and the subsequent ferroelectric properties of the PVDF samples, post annealing was conducted after the deposition of the polymers. A series of these samples were created, each with a different annealing temperature. The annealing temperature was varied from 100 °C and up to 140 °C in 10 °C increments. XRD measurements were taken on these samples to determine the optimized annealing temperature. For this purpose, all films were kept at a uniform thickness of 70 nm. Figure 4.1 shows the results of the XRD measurements for three samples annealed at different temperatures from 120 °C – 140 °C. Peaks in the XRD graphs represent crystallization of the film and appear in the samples annealed at 130 °C or above. The samples annealed below that temperature do not show a peak in XRD data. The polarization electric field hysteresis measurements done on the samples annealed below 130 °C showed no electrical hysteresis, while measurements done on the samples annealed above that temperature did exhibit square-like hysteresis loops.

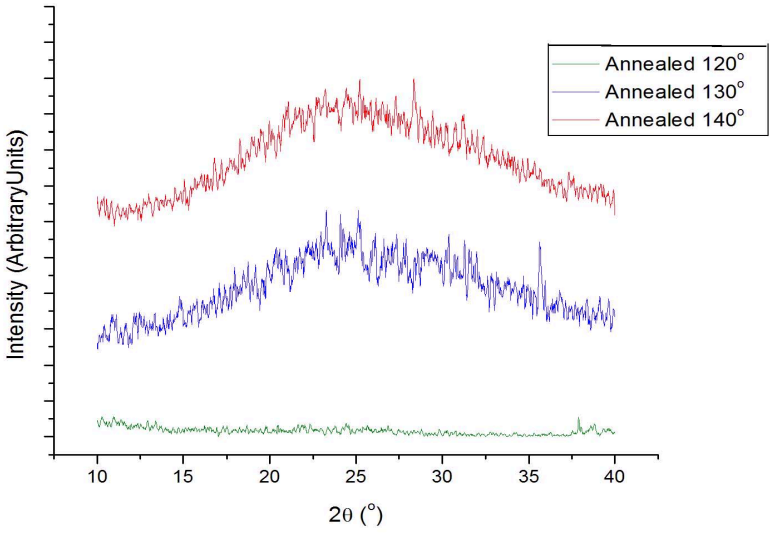

Figure 4.1: X-ray diffraction data of PVDF films annealed at different temperatures. The annealing temperature is indicated in the figure. Crystallization occurs after annealing above 130 degrees. The peaks correspond to chain-to-chain spacing of 3.3 Å.

The peaks in the XRD graphs occurred at a 2θ angle of 25 degrees. Using the Bragg equation for XRD, $n\lambda = 2d\sin(\theta)$, the lattice spacing d can be calculated. Using the wavelength of the x-rays $\lambda = 1.54$ Å. This gives a lattice spacing for the PVDF polymer of 3.5 Å. The bond lengths for PVDF polymers and the atom spacings vary between 1 Å and 2.5 Å [128]. So the measured spacing corresponds to the chain-to-chain distance in the polymer films.

The peaks on the XRD graphs are very broad. Looking at the width of the peak at half the maximum value, or the full width-half max, we can estimate the width to be 6 degrees. This corresponds to a variation of approximately 2 Å. This gives us the variations in the chain-to-chain distances. Because it is broad and a large value this

means the chains are not uniform during deposition, and can have some variation in the distance between them. If the spacing previously calculated was a variation in bond lengths, the peak would be much sharper, as the bond lengths don't change.

Data obtained from the ferroelectric hysteresis measurements was used to study the electrical properties of the PVDF films. The films used for this study were all annealed at a temperature of 130 °C. Figure 4.2 shows the polarization, P, as a function of the applied electric field, E, at several different frequencies of the field for a film of 25 ML which has the thickness of about 44 nm. The measurements with different frequencies of the electric field were done at a maximum electric voltage of 4 V, which corresponds to a maximum electric field of 90 MV/m for a 44-nm thick film.

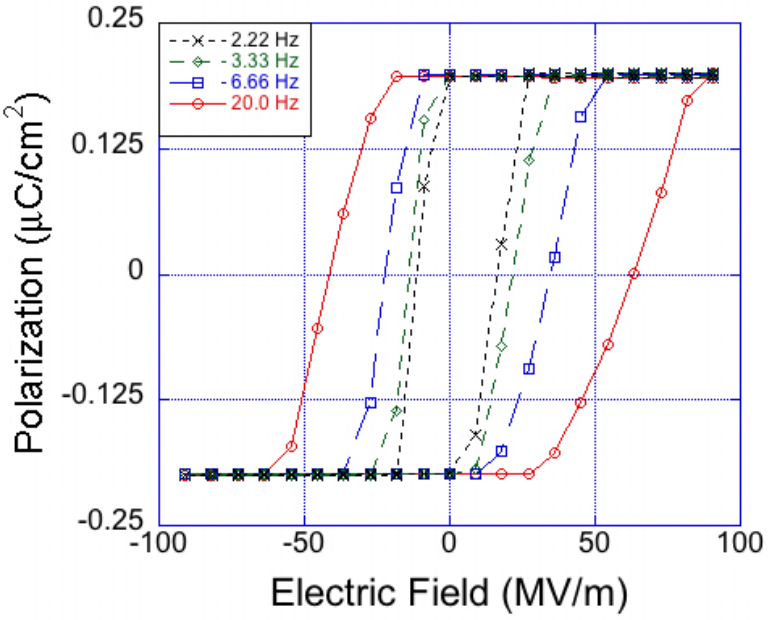

Figure 4.2: PE hysteresis loops measured with different electric field frequencies at a maximum applied voltage of 4 V for films with thickness 44 nm. The coercivity value and area of the loops change as the maximum applied field and frequency change.

Figure 4.3 shows the similar results, with the same maximum voltage, for a film with a thickness of 70 nm. Notice in comparing these two figures that the maximum polarization changes as the thickness changes.

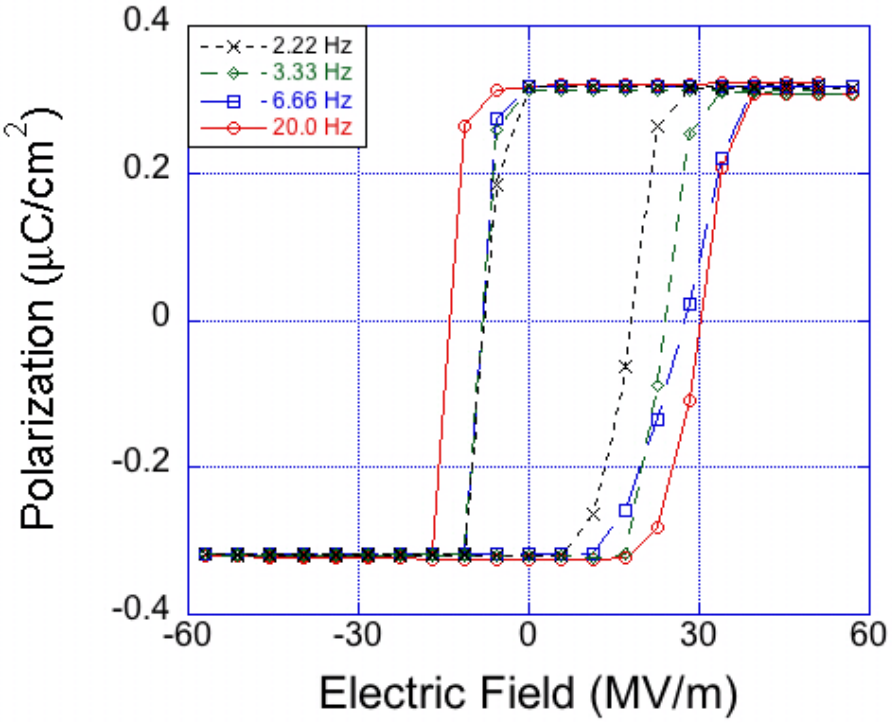

Figure 4.3: PE hysteresis loops measured with different electric field frequencies at a maximum applied voltage of 4 V for films with thickness 70 nm. The changes in coercivity and loop area can still be seen.

From these graphs, the electric coercivity for the films as a function of frequency of the applied electric field was extracted.

The polarization versus electric field (PE) loops for both film thicknesses show square shapes indicating the high quality of our samples. It is apparent that all the loops

are shifted to the positive direction and this is due to the pinning effect of the electrodes. In our samples we used copper as the bottom electrode and aluminum as the top electrode.

The interactions between PVDF and these two electrodes are different and one electrode shows a stronger pinning effect than the other. As a result, PE loops are shifted in that direction. It also can be seen clearly that as the frequency decreases, the PE loops become narrower. The electric coercivity was recorded for every film thickness at each frequency for two different maximum electric fields. In every loop the coercivity measured on the positive side is greater than the coercivity measured on the negative side due to shift of the loops. The recorded coercivity values as a function of the field frequency for the 44 nm thick film is shown as Figure 4.4. The upper two curves are the coercivities measured at a maximum voltage of 4 V that corresponds to a 90 MV/m electric field. The lower two curves are the values obtained with a lower maximum voltage of 1 V corresponding to a 22.5 MV/m electric field.

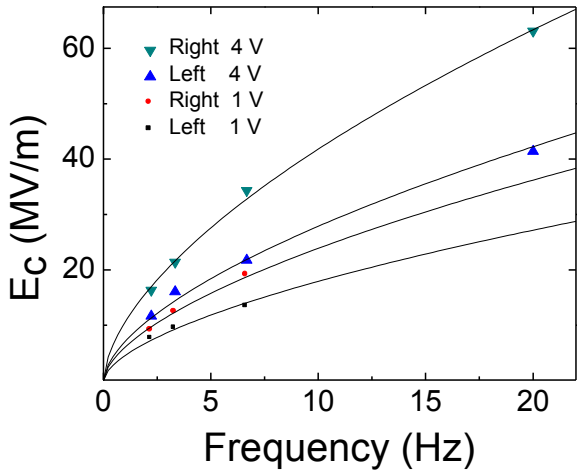

Figure 4.4: Electric coercivity plotted as a function of switching frequency for the films with a thickness of 44 nm. The solid lines are fitted curves.

Figure 4.5 shows similar results of coercivity versus frequency for the film of thickness 70 nm. These two graphs show that the coercivity depends on both the maximum electric field, as well as the frequency of the applied electric field.

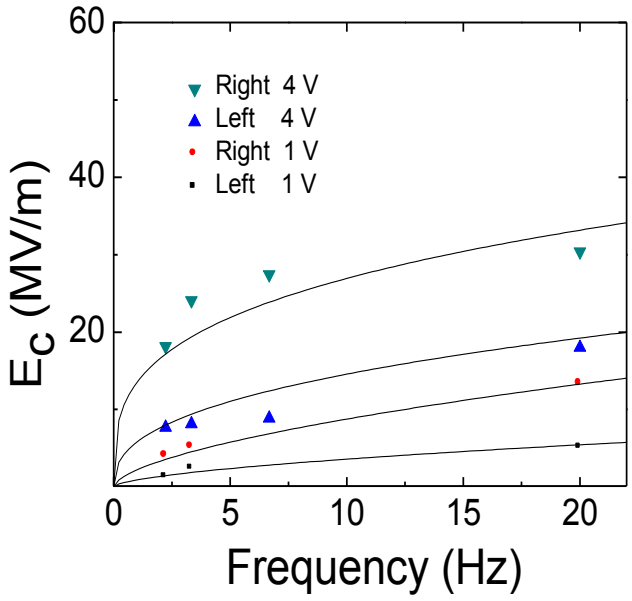

Figure 4.5: Electric coercivity plotted as a function of switching frequency for the films with a thickness of 70 nm. Again, the solid lines are fitted curves.

We observed that the electric coercivity increases as the maximum electric field increases. To explain this result, we start by considering the system as one composed of N electric dipoles, with a dipole moment per volume of μ. We can define the field acting on any one dipole as the local field:

$$E_{local} = E_{ext} + \beta P \qquad (4.1)$$

Here, P is the spontaneous polarization of a dipole, β is a coefficient that refers to the tendency of the dipoles to align in one direction, and E_{ext} is the external applied field.

If we assume a Boltzmann distribution for the system, as shown in other works on PVDF [129], the polarization of the system can be written as:

$$P = N\mu \tanh\left(\frac{\mu(E_{ext}+\beta P)}{kT}\right) \tag{4.2}$$

Then, we can rewrite equation 4.2 to get the external field as:

$$E_{ext} = \frac{kT}{\mu}\tanh^{-1}\left(\frac{P}{N\mu}\right) - \beta P \tag{4.3}$$

To get the coercive field, we want the field, Eext = EC, when the polarization of the system flips from positive to negative. At this field, the value of the polarization is given by [130]:

$$P_C = N\mu\sqrt{1 - T/T_C} \tag{4.4}$$

Here, TC is the Curie temperature. Plugging this back into equation 4.3, the coercive field is given by:

$$E_C = \frac{kT}{\mu}\left[\tanh^{-1}\left(1 - \frac{T}{T_C}\right) - \frac{T_C}{T}(1 - \frac{T}{T_C})^{1/2}\right] \tag{4.5}$$

Expanding this term and looking at only first order, we get the coercive field as:

$$E_C = \frac{kT}{\mu}(1 - \frac{T}{T_C})^{3/2} = N\mu\beta(1 - \frac{T}{T_C})^{3/2} \tag{4.6}$$

But if the crystal consists of repeating molecular units having a vacuum moment μ_0, then the reaction of the surroundings will further polarize the molecule and enhance its moment. If we assume ε_∞ is the relative permeability, then we get [131]:

$$\mu = \frac{1}{3}(\epsilon + 2)\mu_0 \tag{4.7}$$

This can be plugged into equation 4.6 to expand the coercivity. But first, we must look at the product of Nμ. If this value is constant, then the remnant polarization and

coercive field will both also be constant. To correct for this, we need to add a term for the Boltzmann distribution, as we did in equation 4.2. But since the maximum applied external field and maximum polarization are constant, we can replace the term in parenthesis with E_{max}. Thus, the coercive field becomes:

$$|E_C| = \frac{1}{3}(\epsilon + 2)\mu_0 N\beta \left(1 - \frac{T}{T_C}\right)^{\frac{3}{2}} \tanh\left(\frac{\lambda\mu E_{max}}{kT}\right) \quad (4.8)$$

The coefficient λ is a correction factor that must be added to make sure $N\mu = P_{max}$ at the maximum applied electric field. For PVDF, this value is 5.

For a given sample, all other variables will remain constant. That leaves only the maximum applied electric field, E_{max}, to cause a change in the coercivity. The hyperbolic tangent function increases as its argument increases, so the coercivity increases as the maximum electric field increases. As seen in Figure 4.4 and Figure 4.5, the two curves corresponding to higher maximum applied fields do have higher coercivities.

We also observed that the value for the coercivity is affected by the frequency of the electric field. The coercivity increases as the field frequency increases. It has been shown that, at low frequencies less than 1 kHz as described below, dynamic hysteresis can be described by a scaling law: the area A of the hysteresis loops depends on the frequency, f, as $A \propto f^{\alpha}$ for a given electric field, where α, the scaling exponent, is determined by the dimensionality and symmetry of the sample [132].

The area of a PE loop is the energy dissipated within one cycle of domain switching, or one complete PE cycle. Therefore, this energy is the polarization times the electric field, given by:

$$A = PE \quad (4.9)$$

Here, the polarization is the saturation value, and is constant. The electric field then, is the electric coercivity value, E_C. If an electric field of some amplitude, E, is applied to a crystal, the material will absorb a polarization charge equal to twice the remnant polarization of the crystal at E = 0. If the rise time of the electric field is short, no polarization reversal will occur. It's been found by Mertz [133,134] that the polarization reversal is given as a function of the applied field by:

$$\frac{\partial P}{\partial t} \cong e^{-\frac{\alpha}{E}} \tag{4.10}$$

The scaling factor α is defined as a temperature and crystal dependent activation field. The reversal time of the polarization is given by $\tau = \tau_0 e^{-\frac{\alpha}{E}}$ where τ_0 is a constant with units of time. The frequency, in terms of the hysteresis loops, represents a sinusoidal electric field and therefore $\tau = \tau_0 e^{-\frac{\alpha}{E(t)}}$. Hence, the switching time is not obtained in an explicit manner. We assume the polarization reversal takes place in a time that is very short with respect to the switching of the field.

For a rectangular hysteresis loop, switching may be assumed to start only when $E=E_C$ and the reversal time follows the above expression. The switching time, however, is also a function, σ, of the hysteresis cycle f. Hence :

$$\tau = \sigma f \tag{4.11}$$

By equating the equations for the switching time, we obtain:

$$\log\left(\frac{\sigma}{\tau_0}\right) - \log(f) = \frac{\alpha}{E_C} \tag{4.12}$$

Therefore, by plotting EC versus f, we can find the scaling factor for the polymer.

To understand this relation physically, the coercivity of a material depends on the time scale over which a polarization curve is measured. The polarization of a material

measured at an applied reversed field, which is nominally smaller than the coercivity, may, over a long time scale, slowly relax to zero. Relaxation occurs when reversal of polarization by domain wall motion is thermally activated. The increasing value of coercivity at high frequencies is a serious obstacle to the increase of data rates in high-bandwidth magnetic recording, compounded by the fact that increased storage density typically requires a higher coercivity in the media.

At the coercive field, the vector component of the polarization of a ferroelectric material measured along the applied field direction is zero. There are two primary modes of polarization reversal: single-domain rotation and domain wall motion. When the polarization of a material reverses by rotation, the polarization component along the applied field is zero because the vector points in a direction orthogonal to the applied field. When the polarization reverses by domain wall motion, the net polarization is small in every vector direction because the moments of all the individual domains sum to zero. The role of domain walls in determining coercivity is complex since defects may *pin* domain walls in addition to nucleating them.

The quantitative scaling behavior of our samples was investigated. As seen in Figure 4.2 and Figure 4.3, the area of the loops increased as the frequency increased, and that corresponds to an increase in the coercivity in our data. The data from this experiment follows the f^{α} relationship closely. Exponential fitting of the data is shown as the solids lines in Figure 4.4 and Figure 4.5 for 44 nm and 70 nm samples respectively. Dependencies of $f^{\frac{1}{3}}$ and $f^{\frac{2}{3}}$ have been reported in different ferroelectric materials

[135,136]. In this study, the scaling exponent factor α extracted within the measurement uncertainty is 0.6.

The hysteresis loops measured at different frequencies were performed for a series of samples with different thickness ranging from 17 nm to 70 nm. All the loops shifted to the positive direction as noted earlier. The values for coercivity of the left and right were averaged to one value and the values were plotted as a function of thickness for different frequencies. Figure 4.6 shows the results for a maximum electric field of 22.5 MV/m corresponding to a 1 V maximum applied voltage.

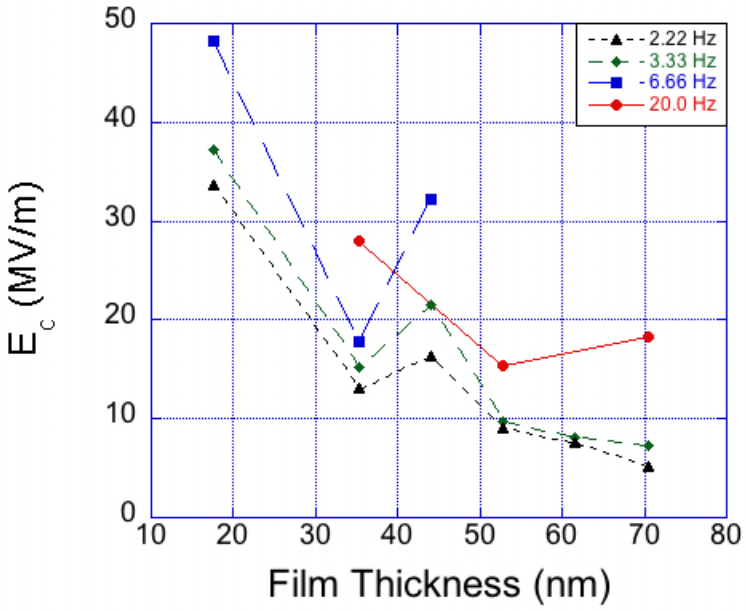

Figure 4.6: Electric coercivity plotted as a function of film thickness measured at different switching frequencies for a maximum applied voltage of 1V.

Like the graphs in Figure 4.2 and Figure 4.3, these graphs show that the coercivity increases as the frequency increases.

Figure 4.7 shows results for a 90 MV/m field corresponding to a 4 V maximum applied voltage. It is apparent that the coercivity of the films decreases as the film

thickness increases (in Figure 4.6 and Figure 4.7). This can be explained by a domain pinning effect from the electrodes. For thin films the interface to volume ratio of the dipoles is large. The pinning effect from the interfaces dominates and a large electric field is required to switch the diploes at the interfaces. For thick films, the interface to volume ratio of the dipoles is smaller. As a result of that, the pinning effect from the interface is less important and a smaller field is required to switch the polarization.

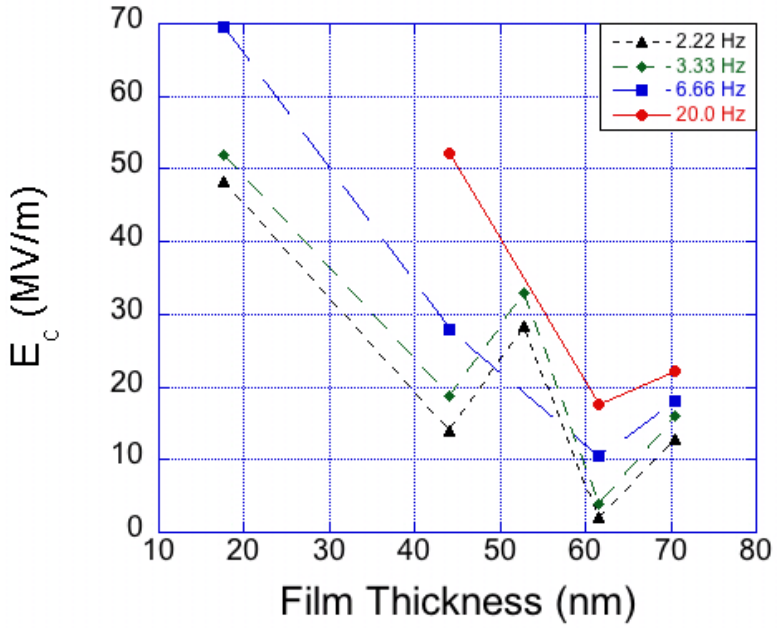

Figure 4.7: Electric coercivity plotted as a function of film thickness measured at different switching frequencies for a maximum applied voltage of 4V.

4.2 EXAFS Analysis of Multiferroic Heterostructures

Now that we have characterized the ferroelectric properties of the PVDF polymer, we wanted to combine that with a ferromagnetic layer to create a multiferroic heterostructure. To analyze the coupling and interaction between the layers, we started by performing EXAFS experiments.

4.2.1 EXAFS Data Elaboration

Using the theoretical equation previously found, detailed analysis has to be performed to obtain precise information from the EXAFS spectra. The analysis procedure is based on fitting the EXAFS equation to the experimental data. To perform this fitting, a software package called FEFF was used. FEFF is a set of programs for processing EXAFS data created by Bruce Ravel and his colleagues at Brookhaven National Lab and available as freeware. It consists of several necessary procedures that are performed in order to obtain an accurate final result. The following sections will describe in some detail these procedures.

The part of the spectra before the step edge in considered the pre-edge portion. Based on experimental conditions, including beamline conditions, this section is not always flat, and can have a slope to it. The pre-edge subtraction fits a linear function within a user defined range. The user selects two points before the step edge, “pre1” and “pre2”, and a linear fit is performed. Figure 4.8 shows an example of this, with both points chosen. The fit can be seen by the dashed line. If the user does not select two points, the program will select two default points.

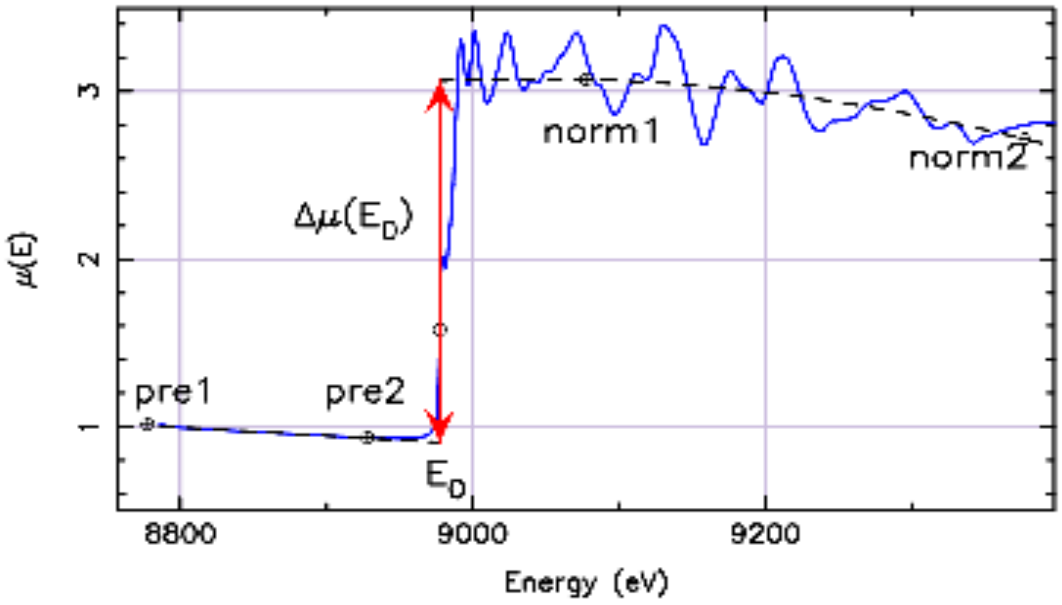

Figure 4.8: EXAFS scan with the Pre-edge subtraction, done using a linear fit, as shown by the dashed line. The points used for the pre-edge are marked by pre1 and pre2 [138].

The next step in the analysis process is to set the edge step. The edge energy, denoted as E_0 in the software, can be entered by the user for whatever material is under examination. First, the post edge region (the EXAFS region) is fitted to a quadratic curve, again shown in Figure 4.8 as a dashed line in the oscillating part, and uses again two points, "norm1" and "norm2". Both the oscillatory quadratic function and the pre-step linear function are evaluated at the edge energy. The difference between those values is taken as the edge step, and is denoted by the term $\Delta\mu_0(E_0)$.

With a calculated edge step, the spectrum is then normalized to that step according to the following formula:

$$\mu_n = \mu - f_1 * \Psi(E_0) - (1 - f_q * \Theta(E_0)) \tag{4.13}$$

Here, μ is the measured spectrum, the function f_l is the pre-edge linear function, f_q is the oscillatory quadratic function, $\Psi(E_0)$ is equal to 1 for the pre-edge, 0 for the post edge, and $\Theta(E_0)$ is 0 for the pre-edge and 1 for the post edge. The result of this normalization is stored in a file, with a name chosen by the user. An example of the output-normalized curve can be seen in Figure 4.9. This normalization is performed as a way to compare different samples of the same material.

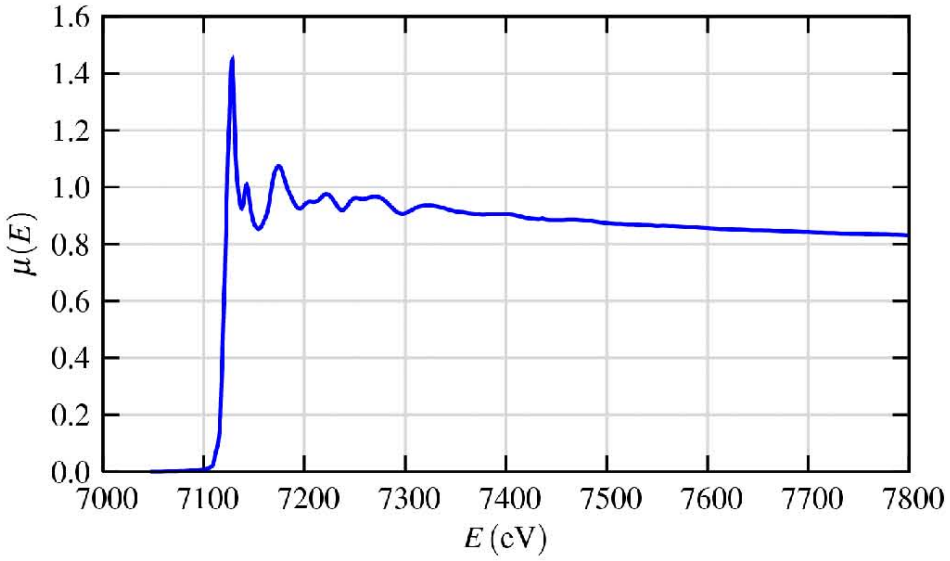

Figure 4.9: Normalized XAFS spectrum. Normalization is used to compare different samples of the same material.

As previously mentioned, EXAFS is only the oscillatory part of the post edge spectrum. The relation between EXAFS and the spectrum is given by:

$$\chi(E) = \frac{\mu(E) - \mu_0(E)}{\Delta\mu_0(E_0)} \tag{4.14}$$

The remaining elemental absorption still contains some background noise such as the spectrometer baseline and elastic scattering. To determine the background function, one

must fit a spline with data points. A spline is a polynomial that might be of linear, quadratic, or cubic order. In this work, the ATHENA [137] program, using a function called AUTOBK, performs the spline procedure [138].

Now, the EXFAS equation is transformed from the energy domain into k domain, as described in the previous "Fundamentals of EXAFS" section. The beginning of the k vector is set as E_0, and the electron kinetic energy is given as $E_e = E - E_0$, where E is the incident energy. The AUTOBK function produces the EXAFS function in k space, a function in which the information about structure is encoded. For an example of this result, refer back to Figure 3.18.

As mentioned and shown in previously in Figure 3.19, the EXAFS function is often multiplied by a factor of k. Using the Fourier Transform procedure on the weighted k space EXAFS function, we obtain a radial distribution function that is related to the charge density around the central atom. An example of this graph is shown in Figure 4.10. From this graph, you are already able to obtain information on the nearest neighbor distances, as well as the number of nearest neighbors. With a material selected, FEFF will insert all necessary values for constants to perform the analysis.

In the previous derivations, only single scattering events have been considered, i.e. only events where the photo-electron scatters directly off the nearest neighbor. In general, the wave can be scattered onto one or more other atoms before being scattered back to the central atom. An example of this is shown in Figure 4.11 a and b [139].

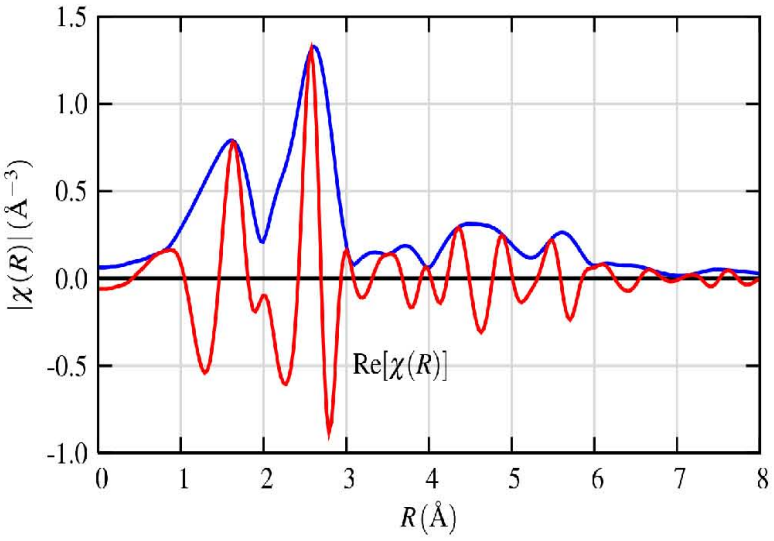

Figure 4.10: Example of a Fourier Transform on the EXAFS function showing the nearest neighbor distances with the real part and the magnitude.

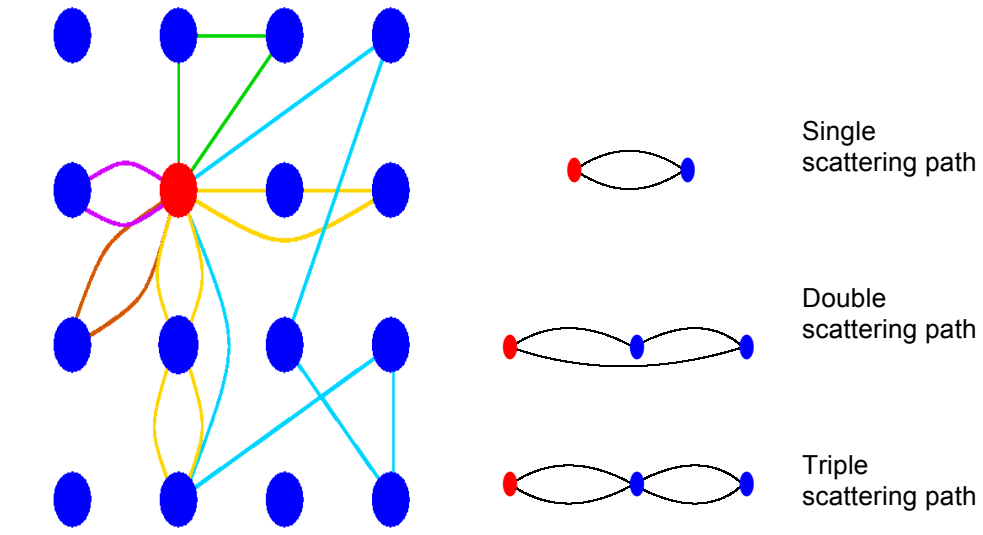

Figure 4.11: a) Multiple backscattering of a photo-electron. b) Definition of different scattering paths [139].

This multiple scattering is important for accurate analysis of EXAFS spectra, due to the fact that the amplitude in Figure 4.10 for the peaks past the first can be even higher with multiple scattering [140]. To calculate the EXAFS signal, FEFF uses a scattering path formalism. In the beginning of the analysis, all scattering paths are determined by FEFF using the known data for a material. For every scattering path with a path length below a program specified cutoff, the EXAFS contribution is calculated and data is stored for each individual path. Using the path formalism feature in FEFF, the total EXAFS spectrum is the sum of all paths, both single and multiple scattering. The advantage of this is that the algorithm uses only paths that have a significant contribution to the signal. This simplifies and shortens the FEFF calculations.

4.2.2 EXAFS Data and Results

For the EXAFS experiments, 3 different sample sets were created, each set containing several identical samples. The samples were approximately 2 cm by 2 cm in size. Extra samples in each set were used to verify that the PVDF polymer exhibited ferroelectric properties. Each of the 3 sets was made such that the electric field could be applied through the iron film in a different way. In the first set, the electric signal travelled through the iron film perpendicular to the surface of the substrate. Figure 4.12 shows a side and top view schematic of this sample set. The current was applied from the top layer (Al) to the bottom layer (Cu).

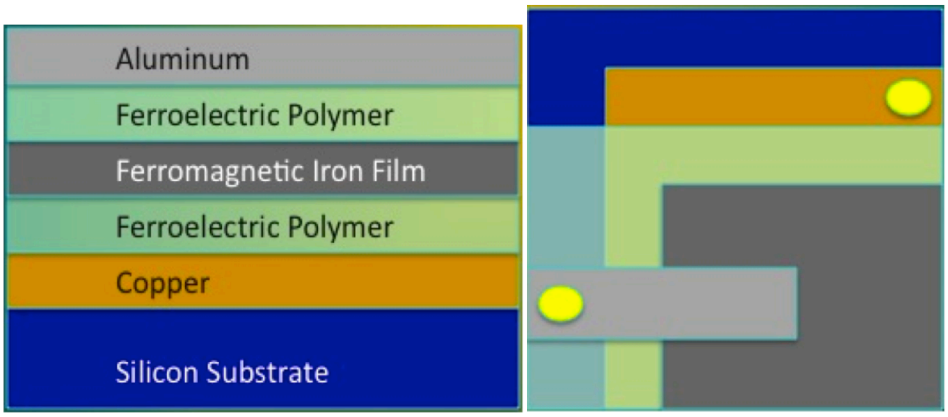

Figure 4.12: Top and side view schematics for samples where the electric field could be applied through the iron film perpendicular to the substrate. Sample area is 2 cm by 2 cm. Side view not shown to scale.

The second set of samples was prepared such that the current flowed through the iron film parallel to the substrate surface. Figure 4.13 shows the side and top view schematics for these samples. Here, a second Al layer has replaced the copper layer. The applied current flows through the film from left to right.

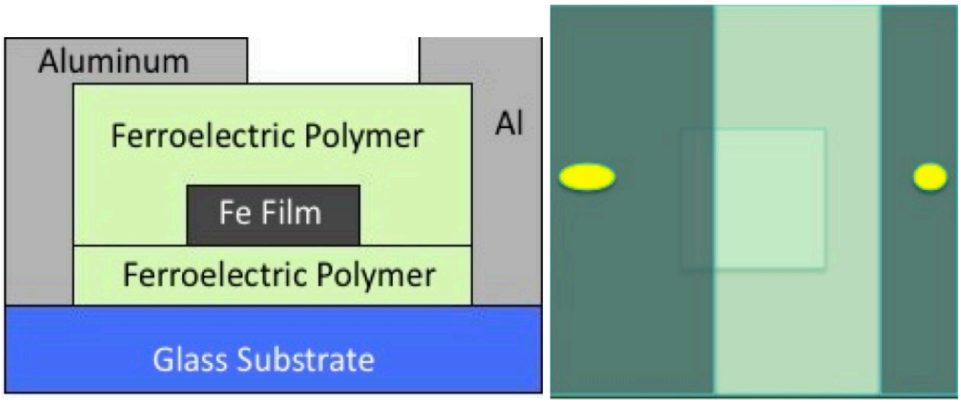

Figure 4.13: Top and side view schematics for samples where the electric field could be applied through the iron film parallel to the substrate. Sample area is 2 cm by 2 cm. Side view not shown to scale.

Finally, a set of samples was created that allowed the electric field to be applied through the film either parallel or perpendicular to the substrate surface. Figure 4.14 shows the top and side schematics for this set. The current was able to flow left to right or top to bottom. For this sample set, the iron film that was evaporated onto the substrate was thicker than the film in the other two sets.

In all schematic diagrams, the small circles are where the electrical connections were made. Also, one sample set was made containing only a iron film evaporated on a clean glass substrate, which would be used as a reference sample.

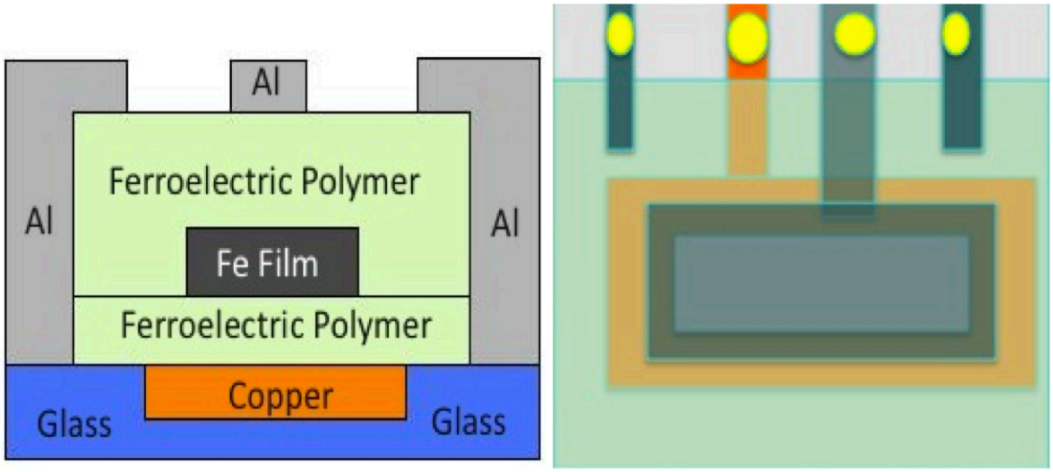

Figure 4.14: Top and side view schematics for samples where the electric field could be applied through the iron film both perpendicular and parallel to the substrate. Sample area is 2 cm by 2 cm. Side view not shown to scale.

EXAFS measurements on the iron K-edge (7112 eV) were collected on a bending magnet beamline (Sector 12-BM-B) at Advanced Photon Source (APS), Argonne

National Lab. Quick EXAFS spectra (about 12 minutes each) were set to repeat and were recorded overnight. The energy range went from below the edge at 6912 eV to an energy above the edge of 7912 eV. The 1 keV region can be used to accurately analyze detailed information on the structure of the sample.

EXAFS scans on samples were performed with and without an electric signal biasing the sample. Hysteresis loops were obtained for samples not used in scanning to find the saturation point for the PVDF polymer. A signal well into saturation was used in the experiment. A Radiant Technology Precision RT66B tester was used to measure the polarization *vs.* electric field hysteresis loops of the films as well as to provide the signal for biasing.

Figure 4.15 shows the iron K-edge EXAFS energy scan for the pure iron film reference sample. This is shown in red and is referred to as S10 reference. Also in Figure 4.15 the energy spectrum for a sample with a thinner iron film from one of the first two sample sets, as in Figure 4.12. For this sample, shown in blue and named S2, no electric field was applied to the sample, so the polymer had never been polarized. The EXAFS oscillations of the iron film sandwiched between the PVDF polymers are very different from the reference sample. There is a considerable decline in the number of oscillations, as well as an increase in the amplitude of the oscillations.

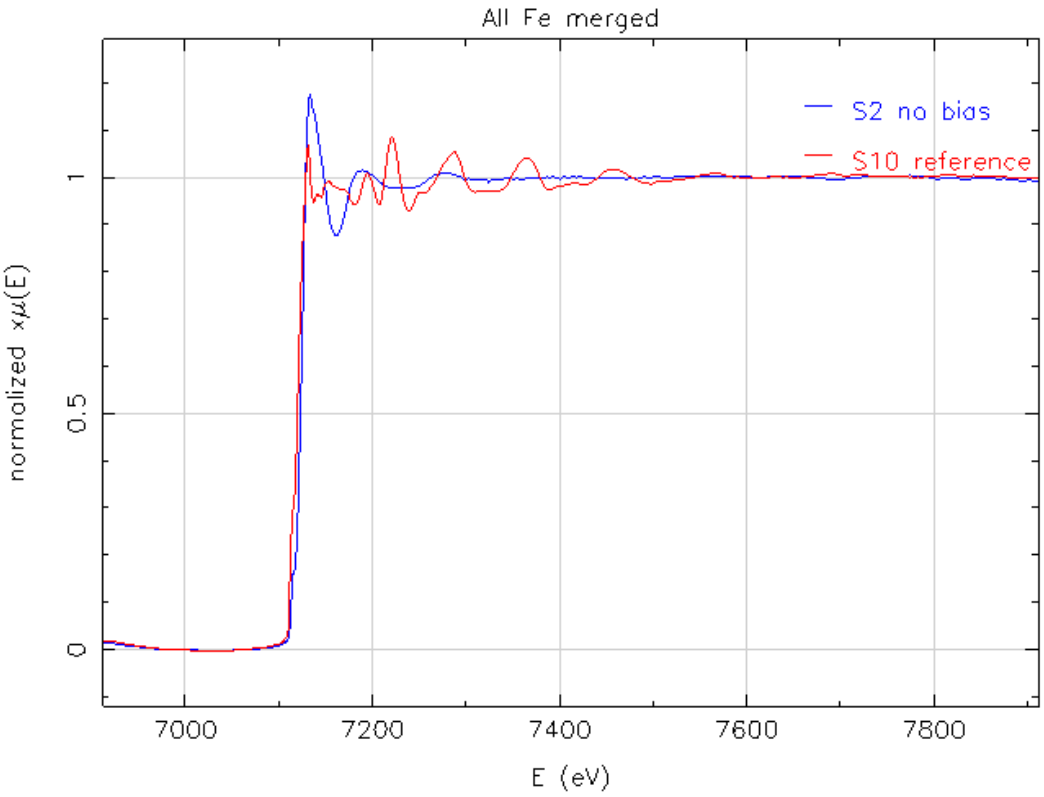

Figure 4.15: EXAFS energy spectrum for a reference iron film and for a sample with a thin Fe film between two PVDF layers.

To get meaning out of these changes, EXAFS was calculated as described previously using the FEFF software. The resulting nearest neighbor graph is shown in Figure 4.16. This represents the radial distribution of atoms about the central iron atoms. The results in this graph can be used to explain the changes seen in the energy spectrum of the iron films. The iron atoms in the sandwiched film are closer together than the atoms in the reference sample. Iron atoms also appear at positions not seen in iron films with a normal structure. The structure for the film layered between the PVDF polymers is

no longer purely face centered cubic as in the reference sample. In the case of the multilayered samples, there is diffusion between the iron atoms and the PVDF layer. At the interface between the iron film and PVDF polymer, iron atoms diffuse into the polymer layer, destroying the pure fcc structure, and allowing the iron atoms to get more tightly packed.

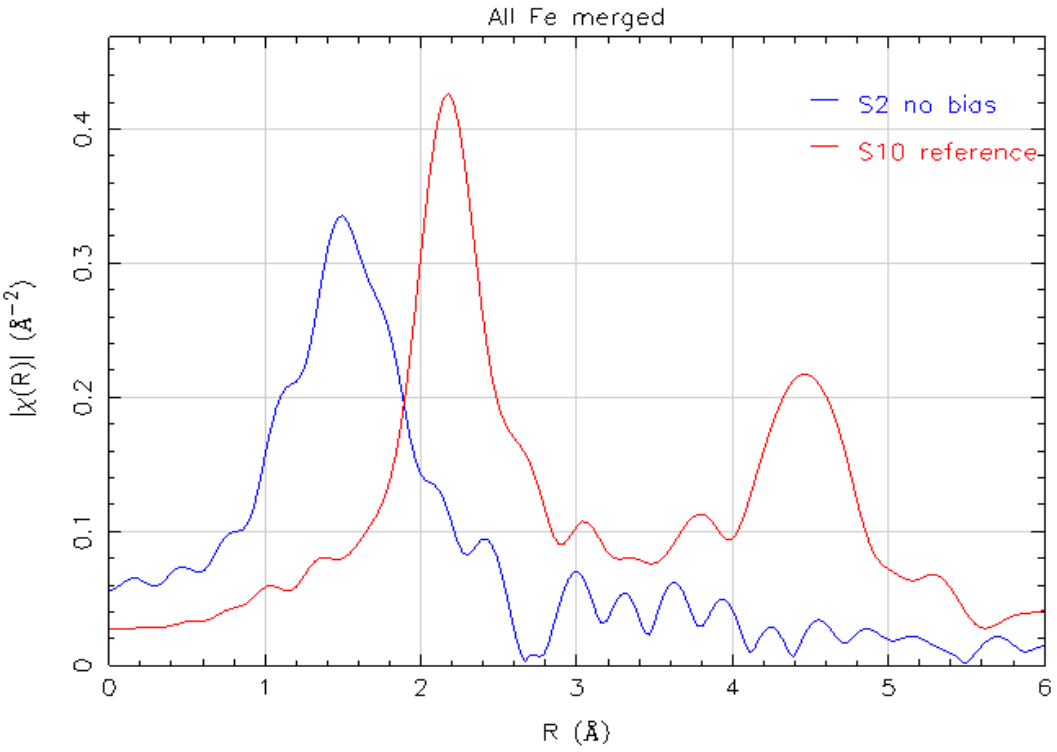

Figure 4.16: EXAFS radial distribution of atoms for a reference iron film and for a sample with a thin Fe film between two PVDF layers.

EXAFS scans were performed on samples with thin iron films both with and without an applied electric field. The absorption spectra for the films with and without the biasing were the same; iron atoms diffused into the polymer during deposition.

Polarizing the PVDF layers has no effect on the atoms at the interface since the iron atoms are already embedded in the polymer. The energy scans and nearest neighbor distribution were exactly the same.

EXAFS spectra for the sample set created using the Figure 4.13 configuration showed the same effect as the previous examples. There was no change, and atoms diffused during deposition.

Figure 4.17 presents the absorption spectrum for the reference film along with the spectrum for a sample with a thicker iron film, as seen in Figure 4.14. In this scan, it is seen that the spectrum for the layered sample shifts slightly to the left when compared to the reference sample. In this experiment, as was the case with the previous iron films, there is a reduction in the number of oscillations. Although there is still a reduction, for the thicker films that reduction isn't as large. Many of the oscillations seen in the reference film still appear in the scan of the sample.

A third energy spectrum is also included in Figure 4.17. This spectrum is for the same sample, but taken after a 4V electric signal was used to bias the sample. The signal was large enough that the PVDF polymer would reach saturation, and the field was applied such that it went through the iron film perpendicular to the substrate. It can be seen that there is a small change in the energy scan for the sample film after biasing has occurred. The amplitude of the oscillations after biasing has decreased.

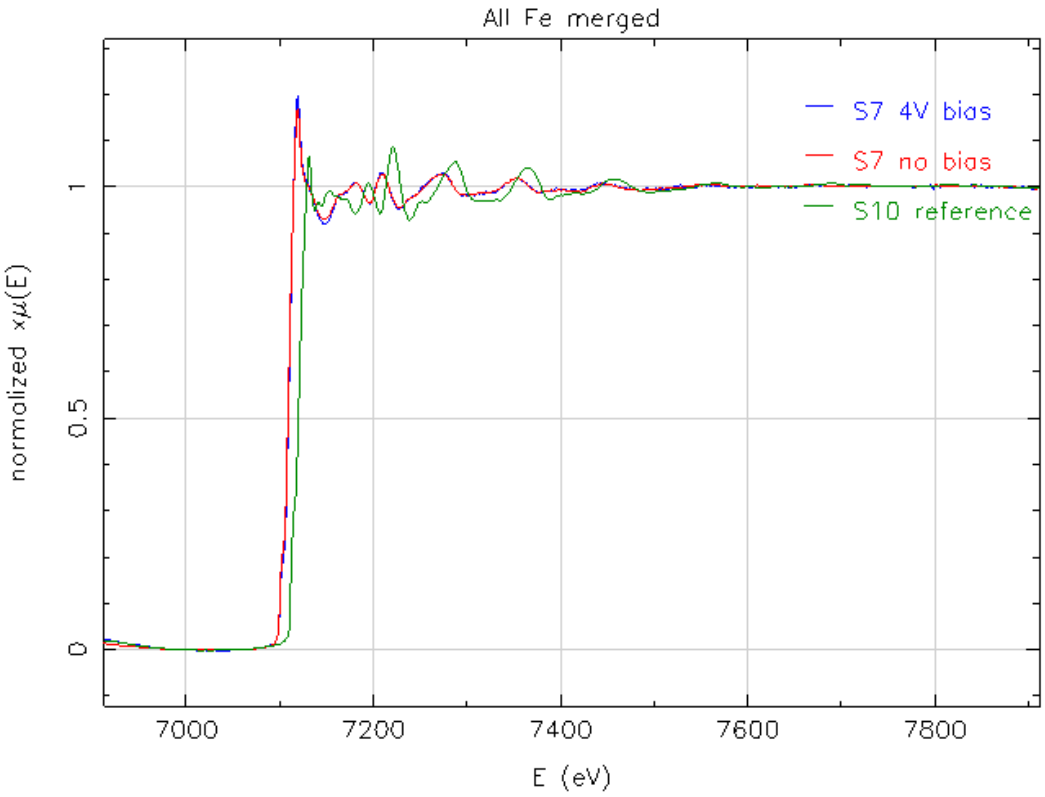

Figure 4.17: EXAFS energy spectrum for a reference film as well as for a sample with an iron film between two PVDF polymer layers. The sample was scanned before and after an electric biasing was applied.

After obtaining the EXAFS energy scans, the radial distribution of atoms for each set was obtained by taking the Fourier transform as previously done. Figure 4.18 shows the resulting distribution for the reference film, as well as for the unbiased and biased sample. For the sample scanned before the electric signal was applied, the position of the iron atoms matches closely with the reference film. While the position of the peaks is the same, the amplitude at each of those peaks is different, indicating that, although iron with

normal structure is still present, some mixing has occurred as at the interface. In the previous scans, the iron films were thinner and there was diffusing that occurred. Here, with a thicker iron film, some mixing does occur at the interface, but some of the iron in the middle of the film still maintains the pure iron phase.

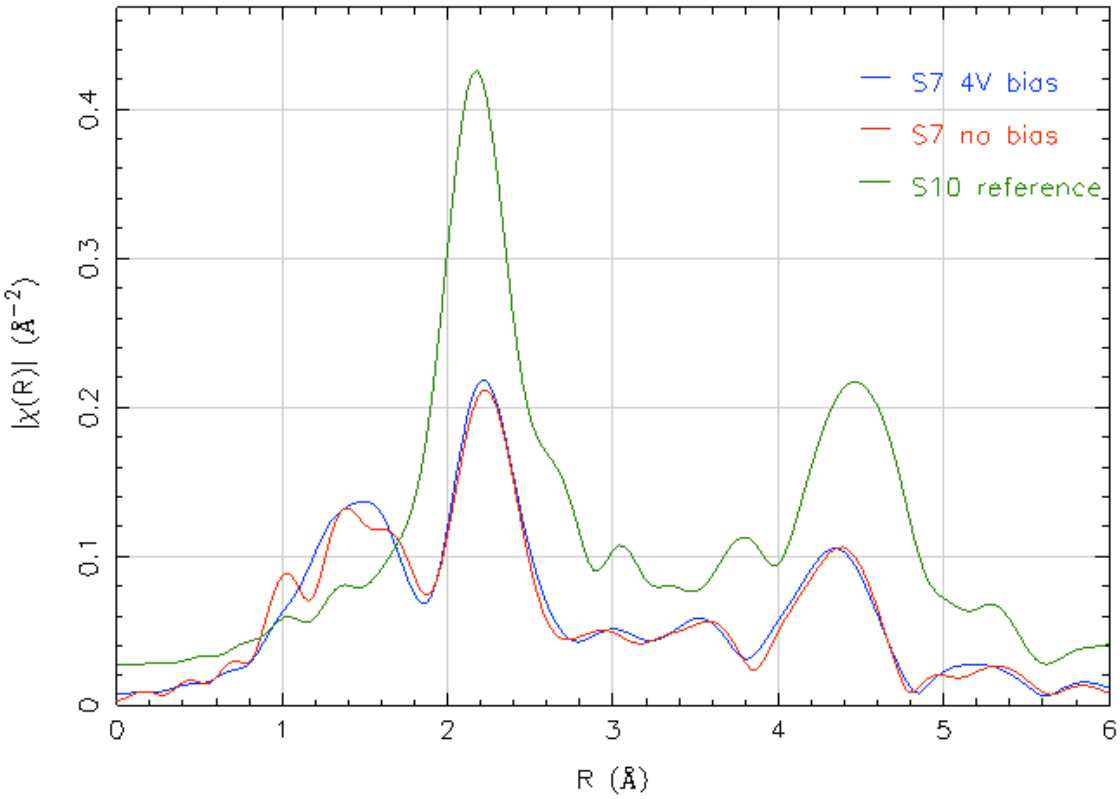

Figure 4.18: EXAFS radial distribution of atoms for a reference film as well as for a sample with a Fe film between two PVDF polymer layers. The sample was scanned before and after an electric biasing was applied.

After applying an electric field to the polymer, a change is seen in the atomic spacing of the iron atoms. Several of the peaks shift slightly, and some of the double peaks and shoulders disappear completely and only a single peak is observed. This is an

indication that as the field is applied and the polymer dipoles align themselves, there is a force that is applied to the iron film, causing the more iron atoms at the interface to diffuse into the polymer. Pure iron still exists in the middle of the film, but additional mixing does occur at the interface.

One problem seen with this heterostructure setup is that the process was neither repeatable nor reversible. Once the iron atoms diffused into the polymer, there was no undoing the process. This shows that any coupling between the ferroelectric and ferromagnetic layers will not be due to piezoelectric strain or magnetostriction. If the coupling was strain induced, a change would be seen when the bias was reversed.

No matter the magnitude or direction of an applied electric field, the atoms were diffused and stuck in the polymer. To use the magnetoelectric coupling in devices, the process needs to be repeatable, so more experiments and different heterostructure setups needed to be used.

4.3 Magnetoelectric Coupling

Since we saw diffusion of iron atoms into the PVDF polymer during EXAFS experiments, we needed to change the heterostructures to prevent this from occurring. We then also had to analyze the magnetoelectric coupling of these heterostructures.

4.3.1 Ferroelectric Response of PVDF to an External Magnetic Field

To prove that any effect was from the iron and PVDF interactions, and not just a response of the PVDF to an external magnetic field, tests were run on samples that contained only the polymer. A lower copper layer and an upper aluminum layer were

added as electrical leads. These samples were placed between the poles of an electromagnet, and the external magnetic field was varied. At each applied magnetic field, a PE loop was taken. The resulting PE loops can be seen in Figure 4.19. As this graph shows, there is no change in the ferroelectric properties of the polymer as the magnetic field is changed.

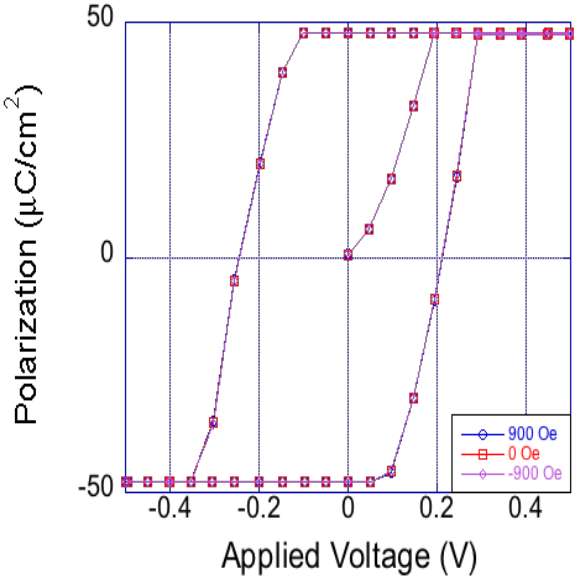

Figure 4.19: PE loops for a sample created with no iron layers. This shows the ferroelectric properties do not change due to an applied magnetic field.

4.3.2 Magnetoelectric Coupling in Multiferroic Heterostructures

To study artificial multiferroics that are based on organic ferroelectrics, we synthesized multiferroic heterostructures, shown as Figure 4.20, consisting of a ferromagnetic iron layer sandwich with ferroelectric polyvinylidene fluoride (PVDF) polymer layer, i.e. Fe/PVDF/Fe. Very thin Al layers (with thickness of only 3 nm) were added to avoid interdiffusion between iron and PVDF layers with the goal of improving

the magneto-electric coupling. By applying an external magnetic field, we were able to control the electric polarization of the ferroelectric PVDF layer. Moreover, as the applied magnetic field is varied, the properties of PVDF layer show hysteretic features.

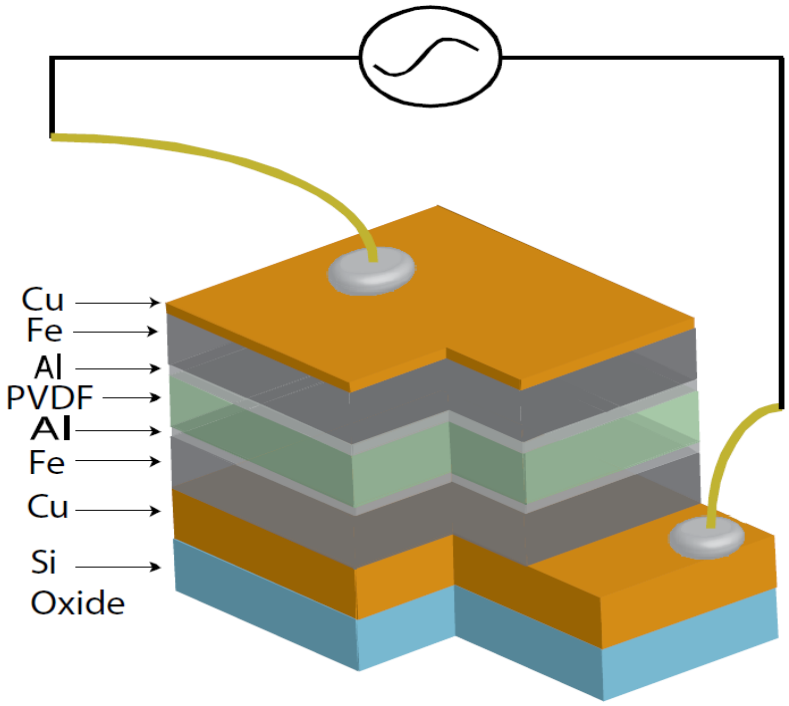

Figure 4.20: Schematic of multilayer ferromagnetic Fe/ferroelectric PVDF/ferromagnetic Fe heterostructure sample. The magnetic field used to magnetize magnetic layers was applied in parallel with the sample. The electric field used to characterize the ferroelectric properties of PVDF layer was applied perpendicular to the sample as shown in the graph. The samples have area 1.5 cm by 2.5 cm, with a total thickness of 100-200 nm, depending on the sample.

A set of samples was created using the above heterostructure design. All samples were 1.5 cm by 2.5 cm in size. In the sample set, the copper layers were deposited using the magnetron sputtering technique described earlier. The bottom copper layer was made

80 nm thick, and the top layer was 15 nm thick. These values were held constant throughout the entire sample set. Similarly, the 3 nm thick aluminum layers were the same throughout the set. These layers were deposited using the thermal evaporation method. The lower iron film layer was also deposited using thermal evaporation, and was held constant at 80 nm thick.

The difference in samples in this set came in the PVDF and upper iron layers. The thickness of these layers was varied in order to examine the magnetoelectric coupling dependence on these parameters. The PVDF layer, deposited using the Langmuir-Schaefer method, was applied with three different thicknesses: 35 nm, 53 nm, and 70 nm. These values corresponded to the number of monolayers deposited during dipping, 20 ML, 30 ML, and 40 Ml respectively. For these three samples, the upper iron layer thickness, thermally evaporated onto the PVDF, was held constant at 26 nm. This was done to prove that any changes or effects were the result of varying the PVDF thickness only.

Similarly, three samples were prepared with varying thickness in the upper iron layer. These iron layers had thicknesses of 26 nm, 39 nm, and 52 nm. For the samples with varying iron thickness, the PVDF layer was held at a constant thickness of 35 nm, or 20 ML. As with the Varying PVDF samples, any changes seen would be solely due to the changing iron thickness.

During testing, each sample was placed between the poles of an electromagnet. The magnetic field applied by the magnet was controlled by the current being sent through it. The electromagnet was calibrated to show the dependence of the field on the current. The calibration showed that it followed the equation:

$$B = (31.762 * I)mT - 23.673\,mT \quad (4.15)$$

The magnetic field created by the electromagnet was applied parallel to the surface of the samples. With the samples between the poles of the magnet and a magnetic field applied, a PE loop was taken of the sample using the Radiant Precision RT66B ferroelectric tester. The electric signal was applied perpendicular to the sample surface, through the leads as shown in Figure 4.20. After a PE loop was obtained at a specified magnetic field, the current was changed to apply a different field, and another PE loop was obtained. This process was repeated for all applied magnetic fields.

Figure 4.21 shows a set of polarization versus electric field hysteresis loops measured under different magnetic fields for a multilayer sample with the key structure of Fe(80 nm)/PVDF(52 nm)/Fe(26 nm). Here the external magnetic field was varied from -930 Oe to 930 Oe and then returned from 930 Oe to -930 Oe. It is clear that the ferroelectric properties of the PVDF polymer thin film strongly depend upon the applied magnetic field.

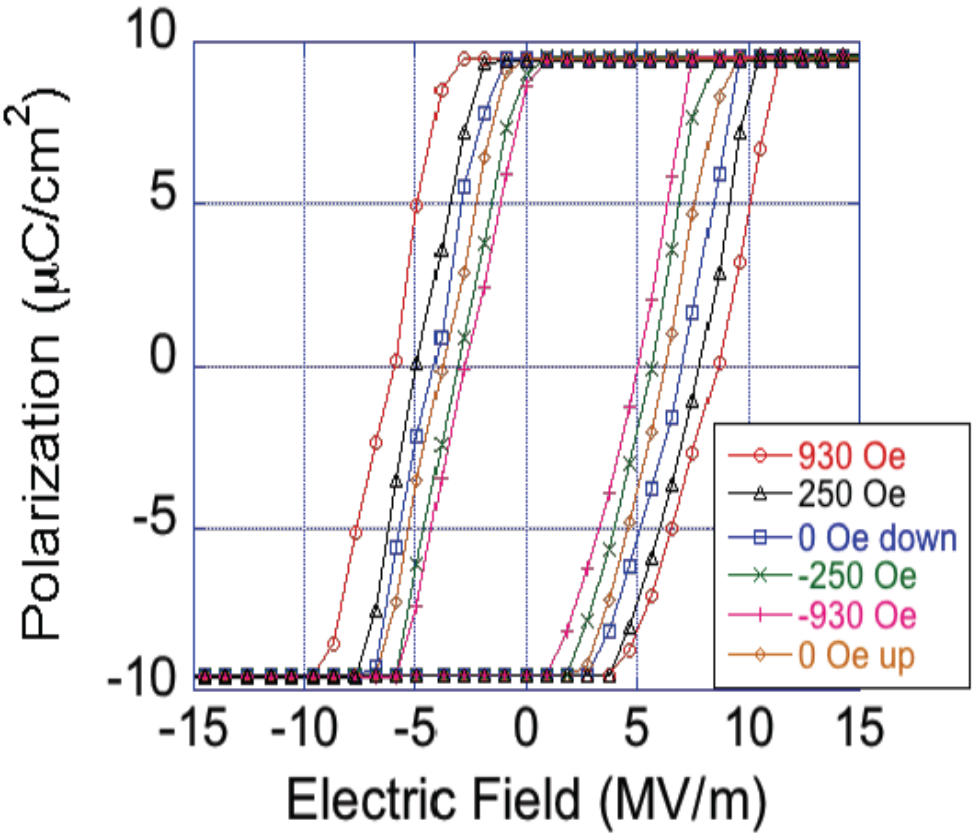

Figure 4.21: PE hysteresis loops of the Fe (80 nm)/PVDF (52 nm) /Fe (26 nm) heterostructure measured under different applied magnetic fields.

This dependence of the PVDF thin film ferroelectric properties is not simply on the magnitude of the external magnetic field, but also on the direction of the magnetic field. The energy product (area under the PE loop) shows a minimum at -930 Oe, which then increases with external magnetic field. When the magnetic field is applied at -930 Oe, as shown in Figure 4.21, the polarization can be saturated at 6.8 MV/m, while the polarization switches with a characteristic coercivity of 4.3 MV/m. As the applied magnetic field approaches to zero, the electric polarization of the PVDF polymer layer

saturates at an electric field of 8.4 MV/m, and the characteristic coercivity is then seen to occur with a 5.5 MV/m field (labeled as 0 up).

The PVDF polymer becomes hard to saturate and flip with the magnetic field changed from -930 Oe to 930 Oe. The PE loop taken at a 930 Oe magnetic field shows that the polarization can be saturated at an electric field of 10.8 MV/m and it can be flipped with a 7.9 MV/m field. While this influence of the external magnetic field is extremely reproducible over many cycles, after the initial cycle, as described above, when the magnetic field goes back to zero from a maximum field, the electric polarization saturates at an electric field of 8.9 MV/m and the coercivity is at 6.9 MV/m electric field. The PE loop taken at this zero magnetic field (labeled as 0 down in Figure 4.21) is different from the results taken at the other zero magnetic field (labeled as 0 up). In order to characterize the magneto-electric coupling of the sample, for a bias electric field of 6.0 MV/m, we studied the polarization versus magnetic field, shown in Figure 4.22. It can be clearly seen that the electric polarization shows hysteresis with the applied external magnetic field.

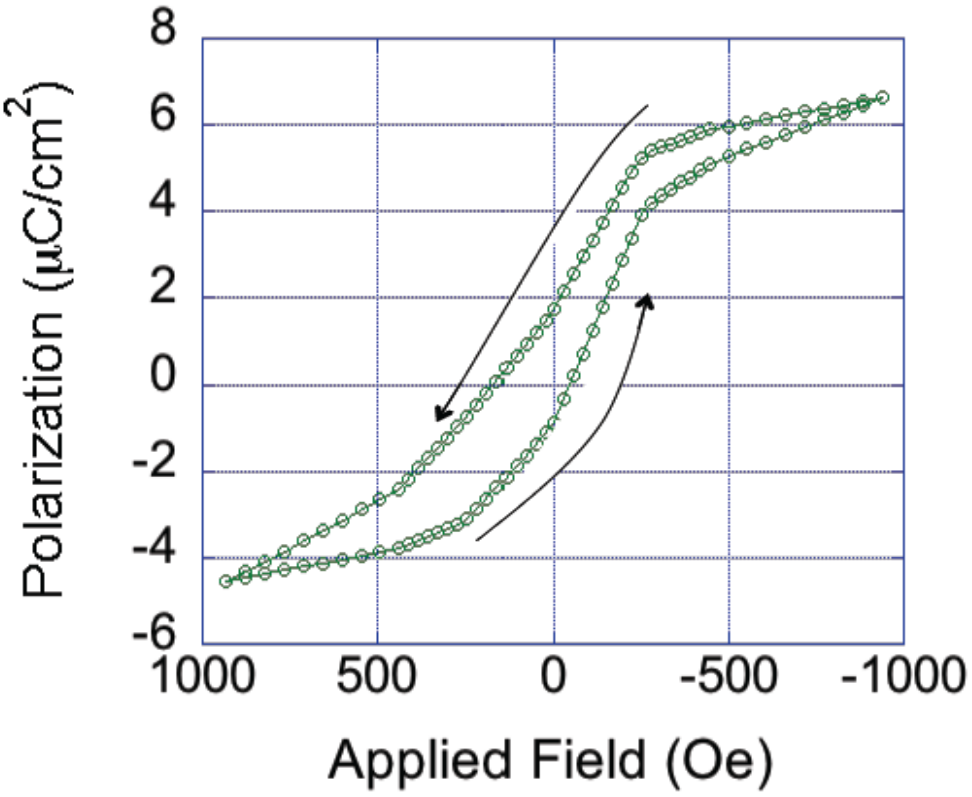

Figure 4.22: The polarization of the PVDF polymer as a function of the applied magnetic field at an electric bias field of 6.0 MV/m.

Because of the fabrication methodology for these Fe/PVDF/Fe heterostructures, the top and bottom PVDF interfaces differ significantly. Iron oxide (likely antiferromagnetic dielectrics) formation is certain at the first PVDF/Fe interface. This oxidation at one interface would tend to give the one iron layer a strong exchange bias. Interdiffusion of iron into the PVDF at the other Fe/PVDF interface is possible [141,142], although we have added Al layers to minimize the diffusion. The difference between the two Fe/PVDF/Fe interfaces is also evident in the difference in the coercive field that indicates that the ferroelectric dipoles do have a slightly favored asymmetry in the

favored dipole direction. This is a common observation, especially with thin organic ferroelectric layers, and also expected on theoretical grounds given the differences in the two Fe/PVDF/Fe interfaces [143]. The differences at each Fe/PVDF/Fe interface and intrinsic exchange bias are evident in the external magnetic field training and the exchange bias is evident in the fact that hysteresis at -930 Oe results in a smaller coercive field than +930 Oe. We have exploited the intrinsic exchange bias in our samples to our advantage.

We have plotted the ferroelectric coercivity of the PVDF polymer in the Fe(80 nm)/PVDF(52 nm)/Fe(26 nm) heterostructure under different magnetic fields as shown in Figure 4.23. Very noticeably, the ferroelectric coercivity shows hysteretic feature with the applied external magnetic field. It is also clear that there is significant magneto-electric coupling presented in our Fe/PVDF/Fe heterostructures.

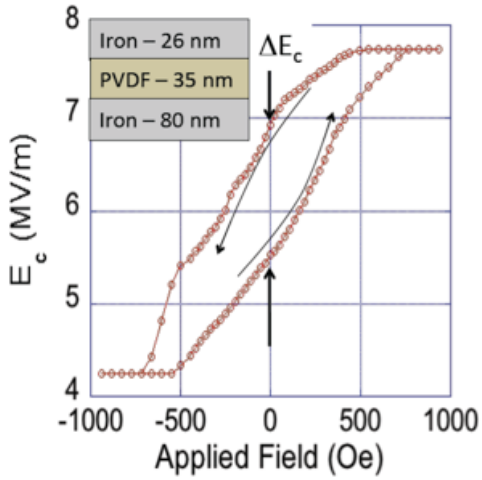

Figure 4.23: Electric coercivity of the Fe (80 nm)/PVDF (52 nm) /Fe (26 nm) heterostructure as a function of the applied magnetic field, showing that the coercivity of the PVDF layer hysteretically depends on the magnetic field.

We also studied the coupling strength dependence upon the PVDF film thickness. The magneto-electric coupling strength in each of the samples is related with, ΔE_C (labeled as the black arrow in Figure 4.23), the width of the hysteresis curve of E_C versus magnetic field graph evaluated at H=0 field. This width ΔE_C indicates the effect of the magnetic field on the ferroelectric property and it has been plotted as a function of PVDF thickness as Figure 4.24.

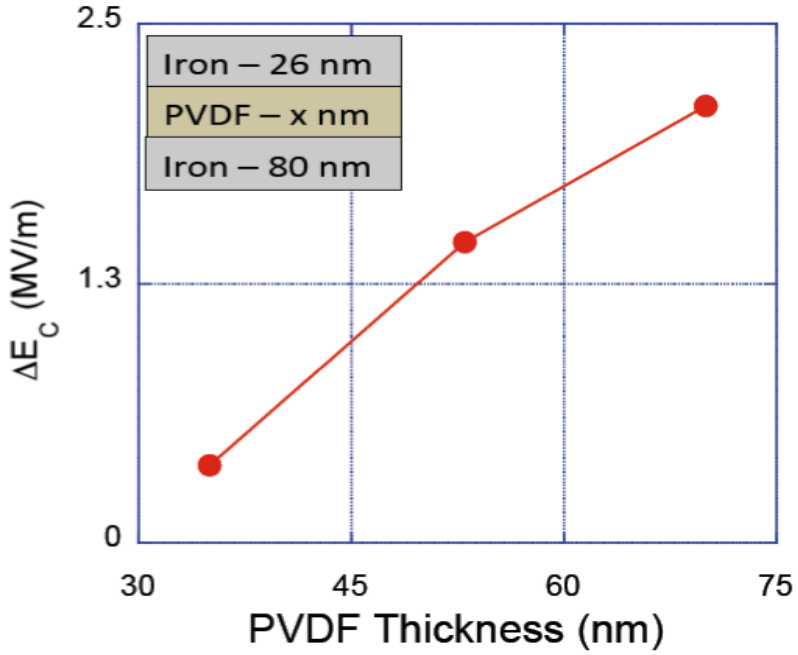

Figure 4.24: ΔE_C, the width of the coercivity hysteresis under magnetic field, as a function of PVDF layer thickness.

While ΔE_C shows a strong dependence on the PVDF thickness, the comparable results for fixed PVDF thickness and varying iron thickness show negligible dependence of ΔE_C. As with the previous case, the electric coercivity of the PVDF layer was graphed as a function of the applied magnetic field, as shown in Figure 4.25.

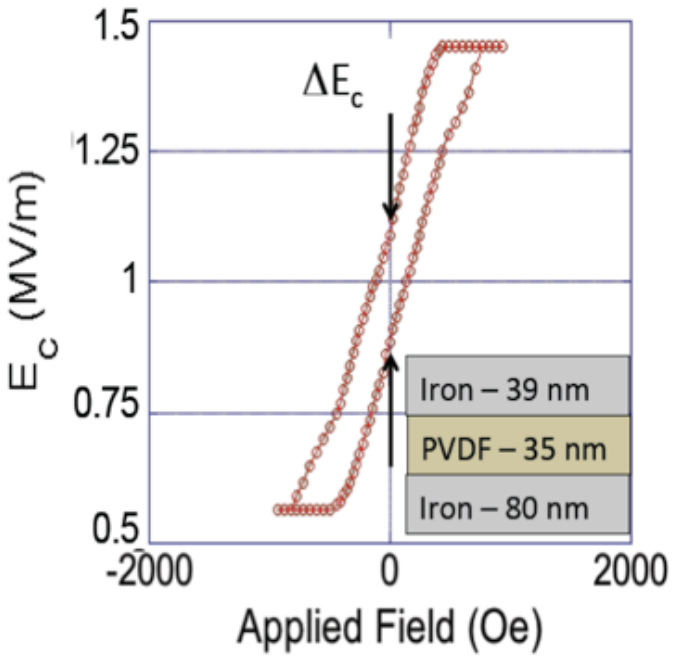

Figure 4.25: Electric coercivity of the Fe (80 nm)/PVDF (35 nm) /Fe (39 nm) heterostructure as a function of the applied magnetic field. We vary the top ferromagnetic Fe layer thickness.

Again, the effect of changing the iron thickness can be seen by graphing the change in the coercivity as a function of iron film thickness, as shown in Figure 4.26. This graph shows the negligible dependence on iron thickness, as the change in coercivity does not change in a noticeable way.

The magneto-electric coupling strength is evident in the width of ΔE_C: the wider ΔE_C, the stronger the magneto-electric coupling strength. It can be seen that as the PVDF thickness increases, the width ΔE_C from the E_C-H hysteresis loops also increases, so the magneto-electric coupling strength increases as the PVDF thickness increases. This cannot be explained by the simple strain effect. First, according to strain effect, the

magnetostriction stress is kept the same for all our samples by keeping the iron layers thickness unchanged. When this same stress (or pressure) is applied to a thicker PVDF layer, the magneto electric coupling effect is expected to be smaller which contradicts our observed data. Second, magnetostriction does not depend on the polarity of magnetic field; however, our data shows dependence on the polarity of the magnetic field.

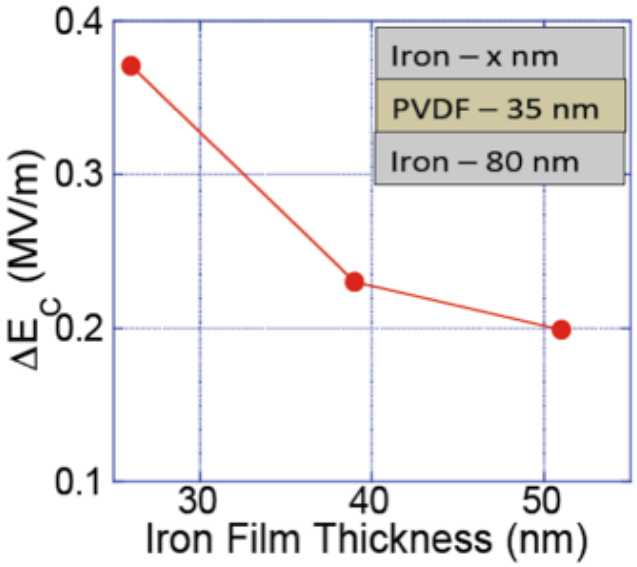

Figure 4.26: ΔE_C, the width of the coercivity hysteresis under magnetic field, as a function of Fe layer thickness.

One possible explanation for the magneto-electric coupling effect is the following: the magnetic field generated by magnetized iron (this generated field is much larger than the external applied magnetic field) can exert a force on rotating dipoles of PVDF and affect the rotation of those dipoles [144,145,146,147]. When an external magnetic field is applied to the samples, the iron layers become magnetized. The magnetization of these layers creates a localized magnetic field, at the interface between iron and PVDF that is

much larger than the applied field. We start by examining the local field due to the iron layer. When an external field is applied, the layer of ferromagnetic iron becomes magnetized. Eventually, the iron will reach a maximum magnetization, the saturation point. The saturation magnetization is equal to the product of the net magnetic moment for each atom and the number of atoms present per unit volume, and can be determined by the following:

$$M_S = 2.22\mu_B N \tag{4.16}$$

Here, μ_B is the Bohr magneton, 9.27 x 10^{-24} Am^2, 2.22 is the number of Bohr magnetons per iron atom [148], and N is the number of atoms per cubic meter. The number of atoms per cubic meter is related to the density, atomic weight, and Avogadro's number. Using the values for iron from a periodic table, we find:

$$N = \frac{\rho N_A}{A} = \frac{(7.86 \times 10^6 g/m^3)(6.023 \times 10^{23} \frac{atoms}{mol})}{55.845\ g/mol} = 8.477 \times 10^{28}\ atoms/m^3 \tag{4.17}$$

Putting this back into equation 4.16, we get that the saturation magnetization for iron is 1.745 x 10^6 A/m.

To find the local magnetic field created by this magnetization, we start with the vector potential due to a magnetized material:

$$\bar{A} = \frac{\mu_0}{4\pi}\int_{Surface}\frac{\bar{\nabla}\times\bar{M}}{\Delta r}d\tau + \frac{\mu_0}{4\pi}\oint_{Surface}\frac{\bar{M}\times d\bar{a}}{\Delta r} = \frac{\mu_0}{4\pi}\int_{Surface}\frac{\bar{J}_b}{\Delta r}d\tau + \frac{\mu_0}{4\pi}\oint_{Surface}\frac{\bar{K}_b}{\Delta r}da \tag{4.18}$$

If a material is saturated, it means all magnetic dipoles are in the same direction and the material is uniformly magnetized, so the bound volume current $\bar{J}$ is zero. The bound surface current is $\bar{K}_b = \bar{M}\times\hat{n}$. Using Ampere's Law, we can obtain the magnetic field:

$$B = \mu_0 M_S = 4\pi \times 10^{-7} T * \frac{m}{A} * 1.745 \times 10^6 \frac{A}{m} = 2.193\, Tesla = 2.2 \times 10^4 Oe \qquad (4.19)$$

This value for B, on the order of 10^4 Oe, is much greater than the external applied field of 10^2 Oe.

In other inorganic materials, the dipoles that flip during coupling are due to the material itself. There is no movement of atoms in the materials. For inorganic materials, magnetoelectric coupling generates a force on the order of 10^{-12} N at a ferroelectric/ferromagnetic interface [149,150,151]. In PVDF, the dipoles are formed due to the electronegativity difference between the fluorine and hydrogen atoms. In this case, to flip the dipoles, the position of the actual atoms must flip. For the polarization direction to flip from up to down, the fluorine atoms must switch positions with the hydrogen atoms. The chains themselves must rotate. This rotation leads the chains to have some velocity.

This velocity has been calculated for PVDF polymers based on the switching time for the dipoles [152]. Previous works have shown this velocity to be on the order of 10^3 m/s [153,154]. Using the Lorentz Force equation, F = qvB, a force of 10^{-10} N is generated at the interface. The direction of this force does depend on the polarity of the magnetic field.

As a result of that, this additional force can affect and tune the polarization properties of the PVDF layer. This force then permeates through the material, and is transferred to other chains deeper into the heterostructure, thereby causing movement and rotation in the other chains. When all the chains start to rotate and change their dipole direction, it causes an overall change in polarization of the material.

The predicted results for the forces generated at the ferroelectric/ferromagnetic interface by organic PVDF is several orders of magnitude higher than the forces generated at the same interfaces for inorganic materials. This predicts that there should be a giant magnetoelectric coupling, also several orders of magnitude higher in organic PVDF than in inorganic materials. Our results support this theoretical prediction.

The linear term for the magneto-electric coupling is often used to characterize the performance of a magneto-electric material, and is defined as [155,156]:

$$\alpha_E = \frac{\Delta E}{\Delta H} \tag{4.22}$$

This quantifies the response of a ferroelectric layer, such as in our heterostructures, to the applied magnetic field. The linear magneto-electric coefficient α_E has been estimated as a function of the PVDF ferroelectric layer thickness by extracting the change in the electric field of the polymer layer with applied magnetic field from the polarization versus magnetic field plots, as shown in Figure 4.22, extracted in the regions of low applied fields. We start this analysis by looking at the definition of polarization.

$$P = (\varepsilon - 1)\varepsilon_0 E \tag{4.23}$$

Here, ε is the permittivity of the material and ε_0 is the permittivity of free space. We can rearrange equation 4.4 to get an expression for the electric field, E. This becomes:

$$E = \frac{P}{(\varepsilon - 1)\varepsilon_0} \tag{4.24}$$

Using equation 4.5, we can now use our data to get an estimate for the change in electric field. For the PVDF polymer, the permittivity is known to be approximately 13. Using Figure 4.22, we estimate the change in the polarization around low magnetic fields as:

$$\Delta P = 5\,\frac{\mu C}{cm^2} = 0.05\ \frac{C}{m^2} \tag{4.25}$$

Plugging this value, as well as the values for ε and ε_0, into equation 4.5, we can estimate a value for the change in electric field as:

$$\Delta E \cong 5 \times 10^8\ \frac{V}{m} \cong\ 5 \times 10^6\ \frac{V}{cm} \tag{4.26}$$

Using this value back in equation 4.3, along with a value of 500 Oe for DH, obtained from Figure 4.22, we can estimate the coupling coefficient as:

$$\alpha_E = \frac{\Delta E}{\Delta H} = \frac{5 \times 10^6\ \frac{V}{cm}}{500\ Oe} = 10^4\ \frac{V}{cm{*}Oe} \tag{4.27}$$

The values of magneto-electric coupling coefficient α_E for our samples are estimated to be 3700±400 V/(cm Oe), 30000 V/(cm Oe), and 41700±2200 V/(cm Oe), for samples with a PVDF layer thickness of 35 nm, 52 nm and 70 nm, respectively. A graph of the magnetoelectric coupling constant for all samples, including the varying PVDF polymer and iron layer thickness samples, is shown in Figure 4.27. These giant α_E values for the magneto-electric coefficient are almost 50 times higher than previously reported [157,158]. This points a way to increasing the magneto-electric effect: construct multiferroics from organic multilayer structures or metal organic frameworks (MOFS). We have now shown that a large electrical response for only a small applied magnetic field change is also possible – ideal for magnetic sensors.

As stated earlier in this section, very thin Al layers were added to avoid interdiffusion between iron and PVDF layers with the goal of improving the magnetoelectric coupling. To show that this change was necessary and prove that the aluminum did improve the magnetoelectric coupling, the tests were run on a sample

created similar to the structure in Figure 4.20, but with the aluminum removed. This sample was of structure Fe (80 nm)/PVDF (70 nm) /Fe (26 nm). The results of this test are shown in Figure 4.28. It is seen in this graph that changes in the ferroelectric properties, and therefore magnetoelectric coupling, are present.

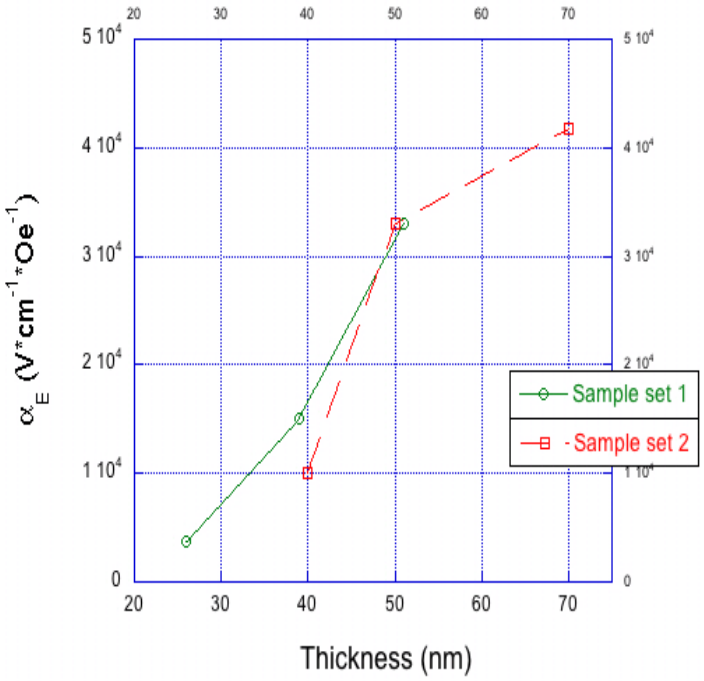

Figure 4.27: Coupling coefficient values for different sample sets.

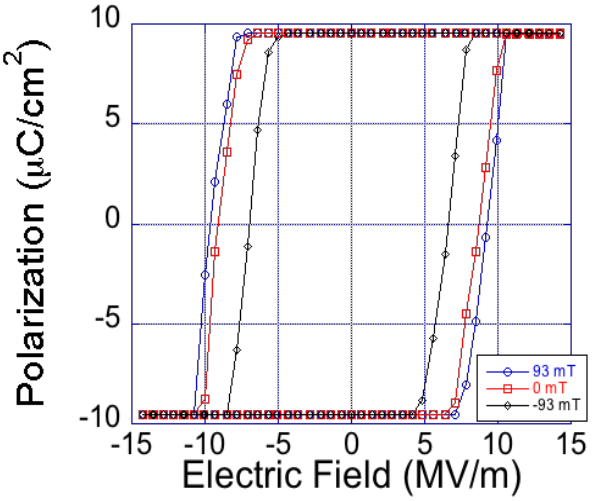

Figure 4.28: PE loops for a Fe (80 nm)/PVDF (70 nm) /Fe (26 nm) heterostructure with no aluminum layers.

Examining the polarization and electric coercivity as a function of applied magnetic field was also performed. The results of the coercivity versus applied magnetic field can be seen in Figure 4.29, with the polarization versus applied magnetic field shown in the inset. The coupling constant for this sample is 3000 V/(cm Oe). For comparison, the value for the coupling constant for the same structure with aluminum was 41700 V/(cm Oe). This shows that adding an aluminum layer between the polymer and iron layers does improve the coupling.

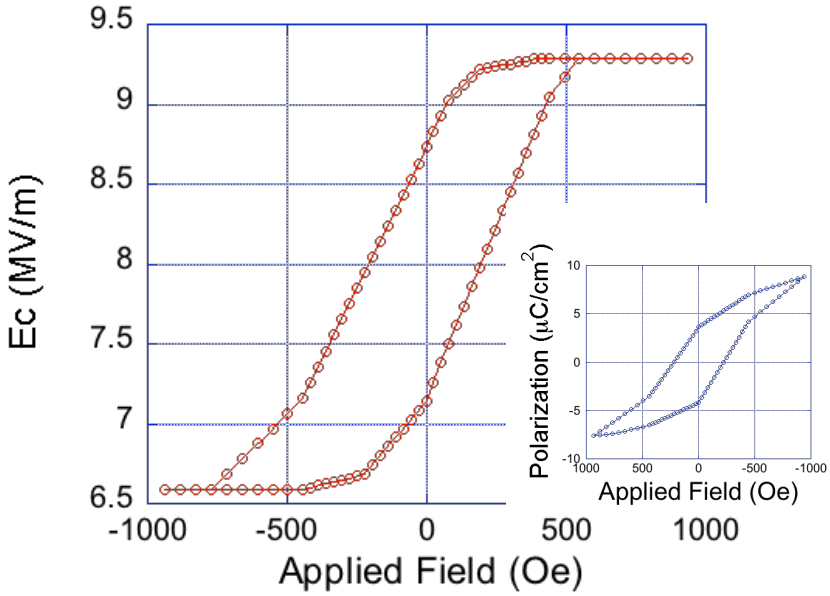

Figure 4.29: Coercivity versus applied magnetic field for a heterostructure sample with no aluminum layers. Inset: Polarization versus magnetic field graph for the same sample.

CHAPTER 5. CONCLUSIONS

In this thesis, we started by characterizing PVDF polymer films created using a Langmuir-Schaefer method. These polymers were found to crystallize and show ferroelectric properties above an annealing temperature of 130°C. For ferroelectric PVDF films, the electric coercivity increases as the maximum electric field increases. The coercivity also depends on the frequency of the applied electric field according to a power law, f^{α}. The scaling factor, α, is 0.6 in our samples. A domain pinning effect from the interfaces is observed and evidenced by a shift of the hysteresis loops. The pinning effect also explains the fact that the electric coercivity decreases when the film thickness increases.

Having characterized the PVDF polymer, the next step was to combine this ferroelectric material with a ferromagnetic layer, in this case iron, to form multiferroic heterostructures. To analyze these heterostructures, thin films of ferromagnetic iron were deposited between layers of ferroelectric PVDF polymer. EXAFS studies show that for films too thin, iron atoms diffuse into the polymer at the interface between the materials during deposition. Further EXAFS studies showed that thicker films had some mixing during deposition, but they retained some pure iron structure as well. When an electric signal was applied to the polymer, the aligning of the dipoles in the polymer pressed the iron films, causing more atoms to diffuse at the interface. However, the process was not

reversible or repeatable. Once the atoms diffused into the polymer and changed the structure, we could not get the samples to return to the original state.

Finally, multiferroic heterostructures were created, this time with aluminum layers separating the iron and PVDF layers. We have been able to create multiferroic ferromagnetic/ferroelectric heterostructures by sandwiching a layer of PVDF polymer between ferromagnetic iron thin films. We found that both the coercivity and polarization for the PVDF polymer display hysteretic features as the applied magnetic field is changed. Our experimental results have shown significant advances to prior studies of organic ferromagnetic multilayer studies where an electric field induced change in magnetic anisotropy was demonstrated but here the magneto-electric coupling is seen to be extremely strong by comparison. In our experiments, the electric dipoles in the organic polymer are due to the molecules in the chains. The local magnetic fields created by the magnetized iron layer at the ferroelectric interface causes these dipoles to rotate, and a force is generated that is approximately two orders of magnitude larger than with the inorganic materials. A giant magneto-electric coupling with values as large as 3700 V/(cm Oe) to 41700 V/(cm Oe) have been observed at room temperature.

CHAPTER 6. FUTURE WORK

The experiments in this work have shown that multiferroic heterostructures can exhibit giant magnetoelectric coupling, with coupling coefficients far greater than previously reported results. This was accomplished by creating a heterostructure in which ferroelectric PVDF polymer was sandwiched between ferromagnetic iron layers.

In this work, we controlled the ferroelectric properties of the PVDF using an external magnetic field. This can be useful in future magnetic sensor devices. Future work would explore the opposite effect, controlling ferromagnetic properties using an external electric field.

To run these types of experiments, the sample structure would have to be changed. The samples would have to be a ferromagnetic layer between two polymer layers, similar to the samples used in the EXAFS studies. Unlike those samples, aluminum layers will need to be added between the layers to prevent interdiffusion. In order to test if the ferromagnetic properties can be controlled with an electric field, the samples will be tested using ferromagnetic resonance (FMR).

Ferromagnetic resonance is a spectroscopy technique used to probe the magnetization of ferromagnetic materials. FMR is similar to electron paramagnetic resonance (EPR) and nuclear magnetic resonance (NMR). The difference with FMR is

that it probes the magnetization due to magnetic moments of unpaired electrons rather than atomic nuclei.

FMR is due to the motion of the magnetization of a ferromagnetic material due to an external magnetic field. The magnetic field exerts a torque on the sample magnetization which causes movement in the magnetic moments. The frequency of this movement depends on magnetization, as well as field strength and orientation. This frequency is also much lower than the movement frequency seen in EPR. Thus, the analysis of FMR is far more complex than EPR or NMR.

In an FMR experiment, the sample is placed in a microwave resonant cavity between the poles of an electromagnet. The cavity is fixed at a frequency in the super high band. Using the electromagnet, an applied magnetic field is swept with the sample in place while the resonant microwave absorption is detected. When the movement frequency and microwave frequency are equal, absorption increases, and the signal at the detector decreases.

To test the magnetoelectric coupling, current will be passed through the sample, thereby applying an electric field, while a magnetic field sweep is run. The electric field will be varied, and an FMR measurement will be taken at each value for the electric field. The magnetization and magnetic properties can then be studied as functions of the applied electric field. This process is similar to the work done in this thesis, only with the electric and magnetic roles reversed.

LIST OF REFERENCES

LIST OF REFERENCES

[1] N. Yamauchi, "A metal-insulator-semiconductor (MIS) device using a ferroelectric polymer thin film in the gate insulator," *Jpn J Appl Phys 1*, vol. **25**, pp. 590 – 594, 1986.

[2] P. A. Jacobson, L. G. Rosa, C. M. Othon, K. Kraemer, A. V. Sorokin, S. Ducharme, and P. A. Dowben, "Water Absorption and Dielectric Changes in Crystalline Poly(Vinylidene Fluoride-Trifluoroethylene) Copolymers Films," *Appl. Phys. Lett*., vol. **84**, pp. 88 – 90, 2004.

[3] C. N. Borca, S. Adenwalla, J. Choi, P. T. Sprunger, S. Ducharme, L. Robertson, S. P. Palto, J. Liu, M. Poulsen, V. M. Fridkin, H. You, and P. A. Dowben, "A Lattice Stiffening Transition in Copolymer Films of Vinylidene Fluoride (70%) with Trifluoroethylene (30%)," *Phys. Rev. Lett*., vol. **83**, pp. 4562 – 4565, 1999.

[4] T. T. Wang, J. M. Herbert, and A. M. Glass (Ed.). *The Applications of Ferroelectric Polymers*, New York: Chapman and Hall, 1998.

[5] T. Lottermoser, T. Lonkai, U. Amann, D. Hohlwein, J. R. Ihringer, and M. Fiebig, "Magnetic phase control by an electric field," *Nature*, vol. **430**, pp. 541 – 544, 2004.

[6] M. N. Baibich, J. M. Broto, A. Fert, F. Nguyen van Dau, F. Petroff, P. Eitenne, G. Creuzet, A. Friederich, and J. Chazelas, "Giant Magnetoresistance of (001)Fe/(001)Cr Magnetic Superlattices," *Phys. Rev. Lett*., vol. **61**, pp. 2472 – 2475, 1988.

[7] G. Binasch, P. Grünberg, F. Saurenbach, and W. Zinn, **"**Enhanced magnetoresistance in layered magnetic structures with antiferromagnetic interlayer exchange," *Phys. Rev. B*, vol. **39**, pp. 4828 – 4830, 1989.

[8] J. S. Moodera, L. R. Kinder, T. M. Wong, and R. Meservey, "Large Magnetoresistance at Room Temperature in Ferromagnetic Thin Film Tunnel Junctions," *Phys. Rev. Lett.*, vol. **74**, pp. 3273 – 3276, 1995.

[9] W. J. Gallagher, S. S. Parkin, Y. Lu, X. P. Bian, A. Marley, K. P. Roche, R. A. Altman, S. A. Rishton, C. Jahnes, T. M. Shaw, and G. Xiao, "Microstructured Magnetic Tunnel Junctions," *J. Appl. Phys.*, vol. **81**, pp. 3741 – 3746, 1997.

[10] Q. Chen, A. J. Rondinone, B. C. Chakoumakos, and Z. J. Zhang, "Synthesis of superparamagnetic $MgFe_2O_4$ nanoparticles by coprecipitation," *J. Magn. and Magn. Mater.*, vol. **194**, pp. 1 – 7, 1999.

[11] J. J. Betouras, G. Giovannetti, and J. van den Brink, "Multiferroicity Induced by Dislocated Spin-DensityWaves," *Phys. Rev. Lett.*, vol. **98**, pp. 257602-1 – 257602-4, 2007.

[12] J. Wang, J. B. Neaton, H. Zheng, S. Nagarajan, S. B. Ogale, B. Liu, D. Viehland, V. Vaithyanathan, D. G. Schlom, U. V. Waghmare, N. A. Spaldin, K. M. Rabe, M. Wuttig, and R. Ramesh, "Epitaxial $BiFeO_3$ Multiferroic Thin Film Heterostructures," *Science*, vol. **299**, pp. 1719 – 1722, 2003.

[13] J. Hemberger, P. Lunkenheimer, R. Fichtl, H. A. Krug von Nidda, V. Tsurkan and A. Loidl, "Relaxor Ferroelectricity and Colossal Magnetocapacitive Coupling in Ferromagnetic $CdCr_2S_4$," *Nature*, vol. **434**, pp. 364 – 367, 2005.

[14] I. L. Prejbeanu, S. Bandiera, J. Alvarez-Hérault, R. C. Sousa, B. Dieny, and J.-P. Nozières. "Thermally assisted MRAMs: ultimate scalability and logic functionalities," *J. Phys. D Appl. Phys.*, vol. **46**, no. 7, pp. 1 – 16, 2013.

[15] C. Chappert, A. Fert, F. Nguyen van Dau. "The emergence of spin electronics in data storage," *Nature Mater.*, vol. **6**, pp. 813 – 823, 2007.

[16] M. C. Tsigkourakos and C. Trompoukis, *Magnetoresistive Random Access Memory (MRAM)*, rev. 1, 2010.

[17] A. J. Heeger, "Semiconducting and Metallic Polymers: The Fourth Generation of Polymeric Materials," *Rev. Mod. Phys.*, vol. **73**, pp. 681 – 700, 2001.

[18] A. G. MacDiarmid, "Synthetic Metals: A Novel Role for Organic Polymers," *Rev. Mod. Phys.*, vol. **73,** pp. 701 – 712, 2001.

[19] H. Shirakawa, "The Discovery of Polyacetylene Film—the Dawning of an Era of Conducting Polymers," *Rev. Mod. Phys.*, vol. **73,** pp. 713 – 718, 2001.

[20] H. Sirringhaus, N. Tessler, and R. H. Friend, "Integrated Optoelectronic Devices Based on Conjugated Polymers," *Science*, vol. **280,** pp. 1741 – 1744, 1998.

[21] R. H. Friend, R. W. Gymer, A. B. Holmes, J. H. Burroughes, R. N. Marks, C. Taliani, D. D. C. Bradley, D. A. Dos Santos, J. L. Bredas, M. Logdlund, and W. R. Salaneck, "Electroluminescence in Conjugated Polymers," *Nature*, vol. **397**, pp. 121 – 128, 1999.

[22] A. J. Lovinger, "Ferroelectric Polymers," *Science*, vol. **220**, pp. 1115 – 1121, 1983.

[23] K. Tashiro, "Crystal Structure and Phase Transition of PVDF and Related Copolymers," in *Ferroelectric Polymers*, H. S. Nalwa, ed. New York: Marcel Dekker, pp. 63, 1995.

[24] A. Bune, S. Ducharme, V. Fridkin, L. Blinov, S. Palto, N. Petukhova, and S. Yudin, "Novel Switching Phenomena in Ferroelectric Langmuir–Blodgett Films," *Appl. Phys. Lett*., vol. **67**, pp. 3975 – 3977, 1995.

[25] P. Güthner, and K. Dransfeld, "Local Poling of Ferroelectric Polymers by Scanning Force Microscopy," *Appl. Phys. Lett*., vol. **61**, no. 4, pp. 1137 – 1139, 1992.

[26] J. Choi, P. A. Dowben, S. Pebley, A. V. Bune, S. Ducharme, V. M. Fridkin, S. P. Palto, and N. Petukhova, "Changes in Metallicity and Electronic Structure Across the Surface Ferroelectric Transition of Ultrathin Crystalline Poly(vinylidene Fluoride-Trifluoroethylene) Copolymers," *Phys. Rev. Lett*., vol. **80**, pp. 1328 – 1331, 1998.

[27] J. Choi, C. N. Borca, P. A. Dowben, A. Bune, M. Poulsen, S. Pebley, S. Adenwalla, S. Ducharme, L. Robertson, V. M. Fridkin, S. P. Palto, N. N. Petukhova, and S. G. Yudin, "Phase Transition in the Surface Structure in Copolymer Films of Vinylidene Fluoride (70%) with Trifluoroethylene (30%)," *Phys. Rev. B*, vol. **61**, pp. 5760 – 5770, 2000.

[28] M. T. Hung, O. Choi, Y. S. Ju, and H. T. Hahn, "Heat Conduction in Graphite-Nanoplatelet-Reinforced Polymer Nanocomposites," *Appl. Phys. Lett*., vol. **89**, pp. 0231171-1 – 0231171-3, 2006.

[29] Z. Guo, T. Pereira, O. Choi, Y. Wang, and H. T. Hahn, "Surface Functionalized Alumina Nanoparticle Filled Polymeric Nanocomposites with Enhanced Mechanical Properties," *J. Mater. Chem.*, vol. **16**, pp. 2800 – 2808, 2006.

[30] Z. Yao, H. Liu, M. Cao, H. Hao, and Z. Yu. "Effects of Mn doping on the structure and electrical properties of high-temperature $BiScO_3$–$PbTiO_3$–$Pb(Zn_{1/3}Nb_{2/3})O_3$ piezoelectric ceramics," *Mater. Res. Bull*., vol. **46**, no. 8, pp. 1257 – 1261, 2011.

[31] R. E. Newnham, "Fifty Years of Ferroelectrics," *14th IEEE International Symposium on Applications of Ferroelectrics*, pp. 1 – 6, 2004.

[32] S. L. Swartz, T. R. Shrout, W. A. Schulze, and L. E. Cross, "Dielectric Properties of Lead-Magnesium Niobate Ceramics," *J. Am. Ceram. Soc*., vol **67**, no. 5, pp. 311 – 314, 1984.

[33] K. Matsuura, Y. Cho, and R. Ramesh, "Observation of domain walls in $PbZr_{0.2}Ti_{0.8}O_3$ thin film using scanning nonlinear dielectric microscopy," *Appl. Phys. Lett*., vol. **83**, pp. 2650 – 2652, 2003.

[34] A. Artemev, J. Slutsker, and A. L. Roytburd, "Phase field modeling of domain structures in ferroelectric thin films," *IEEE T. Ultrason. Ferr*., vol. **5**, pp. 963 – 970, 2008.

[35] A. Rudiger, T. Schneller, A. Roelofs, S. Tiedke, T. Schmitz and R. Waser, "Nanosize ferroelectric oxides – tracking down the superparaeletric limit," *Appl. Phys. A*, vol. **80**, pp. 1247 – 1255, 2005.

[36] M. Alexe, A. Gruverman, *Nanoscale Characterization of Ferroelectric Materials*, New York: Springer, 2004.

[37] L. D. Landau, *Collected papers*, Oxford: Pergamon Press, pp. 546, 1965.

[38] W. Cochran, "Dynamical, scattering and dielectric properties of ferroelectric crystals,"*Advanc. Phys*., vol. **18**, pp. 157 – 192, 1969.

[39] H. Bilz, G. Benedek, and A. Bussmann-Holder, "Theory of ferroelectricity: The polarizability model," *Phys. Rev. B*., vol. **35**, pp. 4840 – 4849, 1987.

[40] A. Filippetti, and N. A. Spaldin, "Strong-correlation effects in Born effective charges," *Phys. Rev. B*., vol. **68**, pp. 045111-1 – 045111-4, 2003.

[41] A. Villesuzanne, C. Elissalde, M. Pouchard, and J. Ravez, "New considerations on the role of covalency in ferroelectric niobates and tantalates," *Eur. Phys. J. B*., vol. **6**, no. 3, pp. 307 – 312, 1998.

[42] M. Stengel, D. Vanderbilt, and N. A. Spaldin, “Enhancement of ferroelectricity at metal/oxide interfaces,” *Nature Mater.,* vol. **8,** pp. 392 – 397, 2009.

[43] W. Zhong, D. Vanderbilt, and K. M. Rabe, “First-principles theory of ferreoelectric phase transitions for perovskites: The case of batio3,” *Phys. Rev .B*, vol. **52**, pp. 6301 − 6312, 1995.

[44] L. Q. Chen, “Phase-field method of phase transitions/domain structures in ferroelectric thin films: A review,” *J. Am. Ceram. Soc*., vol. **91**, pp. 1835 – 1844, 2008.

[45] J. Hlinka, “Mobility of ferroelastic domain walls in barium titanate,” *Ferroelectrics*, vol. **349**, pp. 49 – 54, 2007.

[46] R. Smith, S. Seelecke, Z. Ounaies, and J. Smith, “A Free Energy Model for Hysteresis in Ferroelectric Materials,” *J. Intel. Mat. Sys. Struc*., vol. **14**, no. 11, pp. 719 – 739, 2003.

[47] M. Guo, H. Cai, and R. Xiong, “Ferroelectric metal organic framework (MOF),” *Inorg. Chem. Comm*., vol. **13**, no. 12, pp. 1590 – 1598, 2010.

[48] A. J. Lovinger, “Ferroelectric Polymers,” *Science*, vol. **220**, pp. 1115 – 1121, 1983.

[49] S. J. Kang, Y. J. Park, I. Bae, K. J. Kim, H. C. Kim, S. Bauer, E. L. Thomas, and C. Park, “Printable Ferroelectric PVDF/PMMA Blend Films with Ultralow Roughness for Low Voltage Non-Volatile Polymer Memory,” *Adv. Funct. Mater*., vol. **19**, pp. 2812 – 2818, 2009.

[50] J. H. Kim, B. E. Park, and H. Ishiwara. “Fabrication and Electrical Characteristics of Metal–Ferroelectric–Semiconductor Field Effect Transistor Based on Poly(vinylidene fluoride),” *Jpn. J. Appl. Phys*., vol. **47**, pp. 8472 – 8475, 2008.

[51] A. Kimoto, and T. Kitajima, “An optical, electrical and ultrasonic layered single sensor for ingredient measurement in liquid,” *Meas. Sci. Technol*., vol. **21**, no. 3, pp. 035204-1 – 035204-7, 2010.

[52] H. Qu, W. Yao, T. Garcia, J. Zhang, A. V. Sorokin, S. Ducharme, P. A. Dowben, and V. M. Fridkin, “Nanoscale polarization manipulation and conductance switching in ultrathin films of a ferroelectric copolymer,” *Appl. Phys. Lett*., vol. **82**, pp. 4322 – 4324, 2003.

[53] Z. V. Gareeva, and A. K. Zvezdin, "Interacting antiferromagnetic and ferroelectric domain structures of multiferroics," *Phys. Status. Solidi. RRL*, vol. **3**, pp. 79 – 81, 2009.

[54] A. C. Rastogi, and S. B. Desu, "Ferroelectric Poly(vinylidene fluoride) Thin Films Grown by Low-Pressure Chemical Vapor Polymerization," *Chem. Vap. Deposition*, vol. **12**, pp. 742 – 750, 2006.

[55] Y. Lu, J. Claude, L. E. Norena-Franco, and Q. Wang, "Structural Dependence of Phase Transition and Dielectric Relaxation in Ferroelectric Poly(vinylidene fluoride−chlorotrifluoroethylene−trifluoroethylene)s," *J. Phys. Chem. B*, vol. **112**, pp. 10411 – 10416, 2008.

[56] M. Wegener, "Polarization-electric field hysteresis of ferroelectric PVDF films: Comparison of different measurement regimes," *Rev. Sci. Instrum*., vol. **79**, pp. 106103-1 – 106103-3, 2008.

[57] G. Eberle, H. Schmidt, and W. Eisenmenger, "Piezoelectric Polymer Electrets," *IEEE T. Dielect. Elec. In*., vol. **3.5**, pp. 624 – 646, 1996.

[58] M. Tamura, "Piezoelectric Polymer Properties and Potential Applications," *Ultrasonic Symposium Proceedings*, pp. 344 – 346, 1987.

[59] E. Fukada, "History and Recent Progress in Piezoelectric Polymer Research," *1998 IEEE Ultrasonics Symposium*, pp. 597 – 605, 1998.

[60] W. Salaneck, S. Stafstrom, and J. Bredas, *Conjugated Polymer Surfaces and Interfaces: Electronic and Chemical Structure of Interfaces for Polymer Light Emitting Devices*, Cambridge: Cambridge University Press, pp. 172, 2003.

[61] M. Broadhurst, "Polymer Physics," *Phys. Tod*., vol. **37**, no. 1, pp. 51 – 52, 1984.

[62] D. Martin, *Magnetism in Solids*, Oxford: Butterworth & Co Publishers Ltd, First edition, pp. 452, 1967.

[63] J. Coey, *Magnetism and Magnetic Materials*, Cambridge: Cambridge University Press, pp. 625, 2010.

[64] K. Yosida, *Theory of Magnetism*, New York: Springer, pp. 330, 2001.

[65] O. Volnianska, and P. Boguslawski, "Magnetism of solids resulting from spin polarization of p orbitals," *J. Phys.-Condens. Mat*., vol. **22**, no. 7, 0723202-1 – 0723202-4, 2010.

[66] C. Zener. “Interaction between the *d* shells in the transition metals,” *Phys. Rev*., vol. **81**, no. 3, pp. 440 – 444, 1951.

[67] C. Zener, “Interaction between the *d*-Shells in the transition metals. II. ferromagnetic compounds of manganese with perovskite structure,” *Phys. Rev*., vol. **82**, no. 3, pp. 403 – 405, 1951.

[68] H. A. Kramers, “L’interaction entre les atomes magnétogènes dans un cristal paramagnétique,” *Phys*., vol. **1**, no. (1-6), pp. 182 – 192, 1934.

[69] P. W Anderson, “Antiferromagnetism: theory of superexchange interaction,” *Phys. Rev*., vol. **79**, no. 2, pp. 350 – 356, 1950.

[70] P. W. Anderson, “New approach to the theory of superexchange interactions,” *Phys. Rev*., vol. **115**, no. 1, pp. 2, 1959.

[71] J. B. Goodenough, “Theory of the role of covalence in the Perovskite-Type manganites [La,M(II)]MnO3,” *Phys. Rev*., vol. **100**, no. 2, pp. 564 – 573, 1955.

[72] J. Kanamori, “Crystal distortion in magnetic compounds,” *J. App. Phys*., vol. **31**, no. 5, pp. S14 – S23, 1960.

[73] P. Mohn, *Magnetism in the Solid State: An Introduction*, New York: Springer, pp. 240, 2004.

[74] S. Blundell, *Magnetism in Condensed Matter*, Oxford: Oxford University Press, 1st edition, pp. 256, 2001.

[75] D. Sellmyer, “Applied Physics: Strong Magnets by Self-Assembly,” *Nature*, vol. **420**, pp. 374 – 375, 2000.

[76] V. Wadhawan, “Ferroelasticity,” *Bull. Mater. Science*, vol. **6**, no. 4, pp. 733 – 753, 1984.

[77] S. Abrahams, “Ferroelasticity,” *Mater. Res. Bull*., vol. **6**, no. 10, pp. 881 – 890, 1971.

[78] M. Fiebig, “Revival of the Magnetoelectric Effect,” *J. Phys. D: Appl. Phys*., vol. **38**, pp. R123 – R152, 2005.

[79] H. Schmid, “Multiferroic Magnetoelectrics,” *Ferroelectrics*, vol. **162**, pp. 317 – 338, 1994.

[80] N. Spaldin, and M. Fiebig, "The Renaissance of Magnetoelectric Multiferroics," *Science*, vol. **309**, pp. 391 – 392, 2005.

[81] T. Lottermoser, T. Lonkai, U. Amann, D. Hohlwein, J. Ihringer, and M. Fiebig, "Magnetic phase control by an electric field," *Nature*, vol. **430**, pp. 541 – 544, 2004.

[82] T. Kimura, T. Goto, H. Shintani, K. Ishizaka, T. Arima, and Y. Tokura, "Magnetic control of ferroelectric polarization," *Nature*, vol. **426**, pp. 55 – 58, 2003.

[83] D. Khomskii, "Trend: Classifying multiferroics: Mechanisms and effects," *Phys*., vol. **2**, pp. 20, 2009.

[84] J. Maxwell, *A Treatise on Electricity And Magnetism, Posner Memorial Collection, Vol. 1*, Pittsburgh: Carnegie Mellon University Press, 1873.

[85] J. Maxwell, *A Treatise on Electricity And Magnetism, Posner Memorial Collection, Vol. 2*, Pittsburgh: Carnegie Mellon University Press, 1873.

[86] P. Curie, "On the symmetry of the physics phenomena, symmetry of and electric and magnetic field," *J. Phys.*, vol. **3**, pp. 393, 1894.

[87] P. Debye, "Bemerkung zu einigen Versuchen u¨ber einen magneto- elektrischen Richteffekt, (Remarks on some new experiments on a magneto-electric directional effect)," *Z. Phys*., vol. **36**, pp. 300, 1926.

[88] I. Dzyaloshinskii, "K voprosu o magnitno-elektricheskom effekte v anti-ferromagnetikakh (On the magneto-electrical effect in antiferromagnets)," *Sov. Phys. JETP*, vol. **10**, pp. 628, 1959.

[89] D. Astrov, "The magnetoelectric effect in antiferromagnetics," *Sov. Phys. JETP*, vol. **11**, pp. 708, 1960.

[90] E. Ascher, H. Rieder, H. Schmid, and H. Stossel, "Some Properties of Ferromagnetoelectric Nickel-Iodine Boracite, Ni3B7O13I," *J. App. Phys*., vol. **37**, pp. 1404, 1966.

[91] W. Eerenstein, N. D. Mathur, and J. F. Scott, "Multiferroic and Magnetoelectric Materials," *Nature*, vol. **442**, pp. 759 – 765, 2006.

[92] V. J. Folen, G. T. Rado, and E. W. Stalder, "Anisotropy of the Magnetoelectric Effect in Cr_2O_3," *Phys. Rev. Lett*., vol. **6**, pp. 607 – 608, 1961.

[93] C. N. R. Rao, and C. R. Serrao, "New routes to multiferroics," *J. Mater. Chem*., vol. **17**, pp. 4931 – 4938, 2007.

[94] S. Zhang, "Spin-Dependent Surface Screening in Ferromagnets and Magnetic Tunnel Junctions," *Phys. Rev. Lett*., vol. **83**, pp. 640 – 643, 1999.

[95] C. G. Duan, J. P. Velev, R. F. Sabirianov, Z. Zhu, J. Chu, S. S. Jaswal, and E. Y. Tsymbal, "Surface Magnetoelectric Effect in Ferromagnetic Metal Films," *Phys. Rev. Lett*., vol. **101**, pp. 137201-1 – 137201-4, 2008.

[96] J. H. van Vleck, "On the Anisotropy of Cubic Ferromagnetic Crystals," *Phys. Rev*., vol. **52**, pp. 1178 – 1198, 1937.

[97] C. G. Duan, J. P. Velev, R. F. Sabirianov, W. N. Mei, S. S. Jaswal, and E. Y. Tsymbal, "Tailoring Magnetic Anisotropy at the Ferromagnetic/Ferroelectric Interface," *Appl. Phys. Lett.*, vol. **92**, pp. 122905-1 – 122905-4, 2008.

[98] C. A. F. Vaz, J. Hoffman, Y. Segal, J. W. Reiner, R. D. Grober, Z. Zhang, C. H. Ahn, and F. J. Walker, "Origin of the magnetoelectric coupling effect in $Pb(Zr_{0.2}Ti_{0.8})O_3/La_{0.8}Sr_{0.2}MnO_3$ multiferroic heterostructures," *Phys. Rev. Lett*., vol. **104**, pp. 127202, 2010.

[99] C. G. Duan, S. S. Jaswal, and E. Y. Tsymbal, "Predicted Magnetoelectric Effect in $Fe/BaTiO_3$ Multilayers: Ferroelectric Control of Magnetism," *Phys. Rev. Lett*., vol. **97**, pp. 047201-1 – 047201-4, 2006.

[100]. C. G. Duan, J. P. Velev, R. F. Sabirianov, Z. Zhu, J. Chu, S. S. Jaswal, and E. Y. Tsymbal, "Surface magnetoelectric effect in ferromagnetic metal films," *Phys. Rev. Lett*., vol. **101**, pp. 137201, 2008.

[101] K. Yasui, N. Ninagawa, and T. Akahane, "Improvement of the Crystallinity of 3C-SiC Films by Lowering the Electron Temperatures in Afterglow Plasma Region Using Triode Plasma CVD," *J. Electron. Mater*., vol. **26**, pp. 178 – 182, 1997.

[102] R. Fazel-Rezai, *Biomedical Engineering – From Theory to Applications*, In-Tech, pp. 486, 2011.

[103] M. Petty, "Langmuir-Blodgett Films: An Introduction," Cambridge: Cambridge University Press, pp. 256, 1996.

[104] Midwest Tungsten Service, Retrieved 01/18/2013, from http://www.tungsten.com/crucible.html, 2013.

[105] K. L. Chopra, and I. Kaur, *Thin Film Device Applications*, New York: Plenum Press, Chapter 1, pp. 14 – 18, 1983.

[106] R. V. Stuart, *Vacuum Technology, Thin Films and Sputtering*, London: Academic Press, Chapter 3, pp. 65 – 89, 1983.

[107] A. Sanders, F. Salama, and J. P. Handrigan, *Organic Light Emitting Diodes*, Revision 1, 2010.

[108] Radiant Technologies Inc, *Precision RT66B Part III – Hardware Discussion*, 2010.

[109] D. E. Sayers, E. A. Stern, and F. W. Lyte, "New technique for investigating noncrystalline structures: Fourier analysis of the extended X-ray absorption fine structure," *Phys. Rev. Lett*., vol. **27**, pp. 1204 – 1207, 1971.

[110] B. Lengeler, *Neutron and X-ray Spectroscopy, chapter 4 - Extended X-ray absorption fine structure*, Dordrecht: Springer-Verlag, pp. 131 – 168, 2006.

[111] P. Eisenberger, B. Kincaid, S. Hunter, D. Sayers, E. A. Stern, and F. Lytle, "X-ray absorption spectroscopy using synchrotron radiation for structural investigation of organometallic molecules of biological interest," in *Proceedings of the IV international Conference on Vacuum Ultraviolet Radiation Physics*, Oxford: Pergamon Press, 1974.

[112] M. Newville, *Fundamentals of XAFS*, Revision 1.6.1 (2005).

[113] R. Shankar, *Principles of quantum mechanics*. New York: Plenum, 2nd edition, 1994.

[114] B. K. Teo, *EXAFS: Basic Principles and Data Analysis*, Berlin: Springer, 1986.

[115] J. J. Rehr, and R. C. Albers, "Theoretical approaches to X-ray absorption fine structure," *Rev. Mod. Phys*., vol. **72**, pp. 621 – 654, 2000.

[116] M. Newville, *Fundamentals of XAFS*, Revision 1.6, 2004.

[117] J. J. Rehr, R. C. Albers, and S. I. Zabinsky "High-order multiple-scattering calculations of x-ray-absorption fine structure," *Phys. Rev. Lett*., vol. **69**, pp. 3397 – 3400, 1992.

[118] Argonne National Laboratory Advanced Photon Source, Retrieved 02/10/2013, from http://www.aps.anl.gov/Sectors/Sector9/Science/Programs/exafs/index.html, 2013.

[119] D. C. Koningsberger, and R. Prins, *Chemical Analysis, Vol. 91: X-ray Absorption: Principles, Applications, Techniques of EXAFS, SEXAFS, and XANES*, New York: John Wiley & Sons, pp. 673, 1988.

[120] H. Ebert, "Fully relativistic treatment of core states for spin-dependent potential," *J. Phys. Condens. Matter*, vol. **1**, pp. 9111 – 9116, 1989.

[121] J. Igarashi, and K. M. Hirai, "Magnetic circular dichroism at the *K* edge of nickel and iron," *Phys. Rev. B*, vol. **50**, pp. 17820 – 17829, 1994.

[122] H. Ebert, V. Popescu, D. Ahlers, G. Schutz, L. Lemke, H. Wende, P. Srivastava, and K. Baberschke, "Theoretical and experimental investigations on the magnetic EXAFS at the *K*- and *L*2,3- edges of bcc-Fe," *Europhys. Lett*., vol. **42**, no. 3, pp. 295 – 300, 1998.

[123] P. Carra, B. T. Thole, M. Altarelli, and X. Wang, "X-ray circular dichroism and local magnetic fields," *Phys. Rev. Lett*., vol. **70**, pp. 694 – 697, 1993.

[124] B. T. Thole, P. Carra, F. Sette, and G. van der Laan, "X-ray circular dichroism as a probe of orbital magnetization," *Phys. Rev. Lett*., vol. **68**, pp. 1943 – 1946, 1992.

[125] D. C. Koningsberger, B. L. Mojet, G. E. van Dorssen, and D. E. Ramaker, "XAFS spectroscopy; fundamental principles and data analysis," *Top. Catal*., vol. **10**, pp. 143 – 155, 2000.

[126] A. Filliponi, A. DiCicco, and C. R. Natoli, "X-ray-absorption spectroscopy and *n*-body distribution functions in condensed matter. I. Theory," *Phys. Rev. B*, vol. **52**, pp. 15122 – 15134, 1995.

[127] A. Mishra, N. Parsai, and B. D. Shrivastava. "Analysis of K-absorption extended X-ray absorption fine structure data of some transition metals," *X-ray Spec*., vol. **41**, pp. 219 – 224, 2012.

[128] N. Ramer, and K. Stiso, "Comparison of polarization and Born effective charges in alternatively-deflected zigzag and planar-zigzag β-poly(vinylidene fluoride)," *Polymer,* vol. **46**, pp. 10431 – 10436, 2005.

[129] R. Smith, G. Andrew, M. Binu, L. Shifang, and J. Intell, "A homogenized energy model for hysteresis in ferroelectric materials: General density formulations," *J. Intell. Mater. Systems Struct*., vol. **16**, pg. 713 – 732, 2005.

[130] R. Smith, and C. Hom, "A Temperature-dependent Constitutive Model for Relaxor Ferroelectrics," *J. Intell. Mater. Systems Struct*., vol. **16**, pg. 433 – 448, 2005.

[131] M. Broadhurst, G. Davis, J. McKinney, and R. Collins, "Piezoelectricity and Pyroelectricity in Polyvinylidene Fluoride – a Model," *J. App. Phys*., vol. **49**, pg. 4992 – 4997, 1978.

[132] J. M. Liu, W. M. Wang, Z. G. Liu, H. L. Chan, and C. L. Choy, "Dynamic hysteresis in ferroelectric systems: experiment and Monte Carlo simulation," *Appl. Phys. A*, vol. **75**, pp. 507 – 514, 2002.

[133] W. J. Mertz, "Domain Formation and Domain Wall Motions in Ferroelectric $BaTiO_3$ Single Crystals," *Phys. Rev*., vol. **95**, pg. 690 – 698, 1954.

[134] W. J. Mertz, "Switching Time in Ferroelectric $BaTiO_3$ and Its Dependence on Crystal Thickness," *J. Appl. Phys*., vol. **27**, pg. 938 – 942, 1956.

[135] Y. Y. Guo, T. Wei, Q. Y. He, and J. M. Liu, "Dynamic hysteresis scaling of ferroelectric $Pb_{0.9}Ba_{0.1}(Zr_{0.52}Ti_{0.48})O_3$ thin films," *J. of Phys.: Condens. Matter*, vol. **21**, pp. 485901-1 – 485901-8, 2009.

[136] B. Pan, H. Yu, D. Wu, X. H. Zhou, and J. M. Liu, "Dynamic response and hysteresis dispersion scaling of ferroelectric $SrBi_2Ta_2O_9$ thin films," *Appl. Phys. Lett*., vol. **83**, pp. 1406 – 1408, 2003.

[137] B. Ravel, and M. Newville, "ATHENA, ARTEMIS, HEPHAESTUS: data analysis for X-ray absorption spectroscopy using IFEFFIT," *J. Synch. Rad*., vol. **12**, pp. 537 – 541, 2005.

[138] M. Newville, P. Livins, Y. Yacoby, J. Rehr, and E. Stern, "Near-edge x-ray absorption fine structure of Pb: A comparison of theory and experiment," *Phys. Rev. B*, vol. **47**, pp. 14126 – 14130, 1993.

[139] B. Ravel, *Intro to EXAFS Analysis Using Theoretical Standards Part 1: Presentation,* Revision 0.02, 2001.

[140] P. Lee, and J. Pendry, "Theory of the extended x-ray absorption fine structure," *Phys. Rev. B*, vol. **11**, no. 8, pp. 2795 – 2798, 1975.

[141] B. Xu, J. Choi, C. N. Borca, A. V. Sorokin, P. A. Dowben, S. P. Palto, N. Petukhova, and S. G. Yudin, "Comparison of aluminum and sodium doped poly(vinylidene fluoride-trifluoroethylene) copolymers by x-ray photoemission spectroscopy," *Appl. Phys. Lett*., vol. **78**, pp. 448 – 451, 2001.

[142] J. Choi, P. A. Dowben, C. N. Borca, S. Adenwalla, A. V. Bune, S. Ducharme, V. M. Fridkin, S. P. Palto, and N. Petukhova, "Aluminum doping of poly(vinylidene fluoride with trifluoroethylene) copolymer," *Phys. Rev. B*, vol. **59**, pp. 1819 – 1822, 2001.

[143] C. G. Duan, W. N. Mei, W. G. Yin, J. Liu, J. R. Hardy, S. Ducharme, and P. A. Dowben, "Simulations of ferroelectric polymer film polarization: The role of dipole interactions," *Phys. Rev. B*, vol. **69**, pp. 235106 – 235109, 2004.

[144] A. Mardana, M. Bai, A. Baruth, S. Ducharme, and S. Adenwalla, "Magnetoelectric effects in ferromagnetic cobalt/ferroelectric copolymer multilayer films," *Appl. Phys. Lett*., vol. **97**, pp. 112904 – 112907, 2010.

[145] A. Mardana, S. Ducharme, and S. Adenwalla, "Ferroelectric Control of Magnetic Anisotropy," *Nano Lett*., vol. **11**, pp. 3862 – 3867, 2011.

[146] J. X. Zhang, J. Y. Dai, L. C. So, C. L. Sun, C. Y. Lo, S. W. Or, and H. L. W. Chan, "The effect of magnetic nanoparticles on the morphology, ferroelectric, and magnetoelectric behaviors of CFO/P(VDF-TrFE) 0–3 nanocomposites," *J. Appl. Phys*., vol. **105**, pp. 054102 – 054105, 2009.

[147] Y. P. Guo, Y. Liu, J. L. Wang, R. L. Withers, H. Chen, L. Jin, and P. Smith, "Giant Magnetodielectric Effect in 0-3 Ni0.5Zn0.5Fe2O4-Poly(vinylidene-fluoride) Nanocomposite Films," *J. Phys. Chem. C*, vol. **114**, pp. 13861 – 13866, 2010.

[148] A. Ayuela, and N. H. March, "The magnetic moments and their long range ordering for Fe atoms in a wide variety of metallic environments," *Intern. J. Quan. Chem*., vol. **110**, pp. 2725 – 2733, 2010.

[149] M. Fechner, S. Ostanin, and I. Mertig, "Magnetoelectric coupling at biferroic interface studied from first principles," *J. Phys.: Conf. Ser*., vol. **200**, pp. 072027-1 – 072027-4, 2010.

[150] Y. Chen, "Study on multiferroic properties in $Ni_{80}Fe_{20}/BaTiO_3$ bilayer films," *J. App. Phys*., vol. **103**, pp. 07E305-1 – 07E305-3, 2008.

[151] M. Fiebig, "Phase engineering in oxides by interfaces," *Phil. Trans. R. Soc. A*, vol. **370**, pp. 4972 – 4988, 2012.

[152] D. Mao, I. Mejia, H. Steigler, B. Gnade, and M. Quevedo-Lopez, "Polarization behavior of poly(vinylidene fluoride-trifluoroethylene) copolymer ferroelectric thin film capacitors for nonvolatile memory application in flexible electronics," *J. App. Phys*., vol. **108**, pp. 094102 – 094108, 2010.

[153] T. Furukawa, "Ferroelectric properties of vinylidene fluoride copolymers," *Phase Transit*., vol. **18**, pp. 143 – 211, 1989.

[154] M. Li, H. Wondergem, M. Spijkman, K. Asadi, I. Katsouras, P. Blom, and D. de Leeuw, "Revisiting the δ-phase of poly(vinylidene fluoride) for solution-processed ferroelectric thin films," *Nat. Mater*., vol. **AOP**, 2013.

[155] J. Ma, J. Hu, Z. Li, and C. W. Nan, "Recent Progress in Multiferroic Magnetoelectric Composites: from Bulk to Thin Films," *Adv. Mater*., vol. **23**, pp. 1062 – 1087, 2011.

[156] C. W. Nan, M. Li, X. Feng, and S. Yu, "Possible giant magnetoelectric effect of ferromagnetic rare-earth–iron-alloys-filled ferroelectric polymers," *Appl. Phys. Lett*., vol. **78**, pp. 2527 – 2530, 2001.

[157] G. Sreenivasulu, L. Y. Fetisov, Y. K. Fetisov, and G. Srinivasan, "Piezoelectric single crystal langatate and ferromagnetic composites: Studies on low-frequency and resonance magnetoelectric effects," *Appl. Phys. Lett*., vol. **100**, pp. 052901 – 052904, 2012.

[158] J. Zhai, S. Dong, Z. Xing, J. Li, and D. Viehland, "Giant magnetoelectric effect in Metglas/polyvinylidene-fluoride laminates," *Appl. Phys. Lett*., vol. **89**, pp. 083507 – 083510, 2006.

VITA

VITA

Jeffrey David Carvell

EDUCATION

- Ph.D. in Physics, May 2013
  Purdue University, Indianapolis, IN

- Masters of Science in Physics, May 2008
  Purdue University, Indianapolis, IN

- Bachelors of Science in Electrical Engineering, May 2006
  Purdue University, Indianapolis, IN

- Bachelors of Science in Physics, May 2006
  Butler University, Indianapolis, IN

RESEARCH AND PROFESSIONAL EXPERIENCE

- PhD candidate, Department of Physics (Aug. 2006 – May 2013)
  Indiana University Purdue University Indianapolis
  Advisor: Dr. Ruihua Cheng
  Thesis: Study of Heterostructures of Ferromagnetic and Ferroelectric Materials
  - Characterized ferromagnetic materials using a superconducting quantum interference device (SQUID).
  - Characterized ferroelectric polymers using polarization/field hysteresis curves.
  - Combined these ferro- materials in a layered heterostructure. Used techniques including Ferromagnetic Resonance (FMR), Electron Paramagnetic Resonance (EPR), and SQUID to examine the magnetoelectric effect in the layered heterostructures.
  - Used Advanced Photon Source at Argonne National Lab to run x-ray scattering and Extended X-ray Absorption Fine Structure (EXAFS) experiments on multiferroic heterostructures.
  - Conducted solo and group experiments of energy absorption spectra on at the Center for Advanced

- Microstructures and Devices (CAMD) at LSU.
- Analyzed heterostructure surface using atomic force microscopy (AFM) and scanning tunneling microscopy (STM).

- Research Mentor, Department of Physics (June 2010 – August 2010, June 2011 – August 2011)
  Indiana University Purdue University Indianapolis
  - Acted as mentor to high school students participating in summer research projects. Designed projects for the students, helped the students understand the projects, answered questions regarding the projects, gave the students advice and guidance to completing their research, and made sure that progress was being made throughout the summer.

- Research Assistant, Centre National de la Recherche Scientifique (CNRS) (May 2005 – July 2005)
  University of Aix-Marseille, Marseille, France
  Advisor: Dr. Suzanne Giorgio
  - Created iron oxide and cobalt oxide nanoparticles and characterized their size using transmission electron microscopy

- Calibration Technician
  Center for Advanced Product Evaluation, Westfield, IN (Aug. 2004 – May 2005)
  - Responsible for calibrating transducers such as accelerometers and potentiometers and Anthropomorphic Testing Devices (crash test dummies).

PUBLICATIONS

1. **J. Carvell**, R. Cheng, P. Ryan, and N. Leyarovska, "X-ray Analysis of the Interface Between Polyvinylidene Fluoride and Iron Thin Films" (2013), in process.

2. **J. Carvell**, R. Cheng, and P. A. Dowben, "Polymer Interface Induced Spin and Dipole Ordering" Physical Review Letters. (2013) submitted.

3. **J. Carvell**, and R. Cheng, "Study of electric polarization hysteresis in ferroelectric polyvinylidene fluoride films" Mater. Lett. **64**, 1992 (2010).

4. R. Cheng, **J. Carvell**, and F.Y. Fradin, "Room temperature electron transport properties of single C_{60} studied using scanning tunneling microscope and break junctions" J. Appl. Phys. **108**, 053720 (2010).

5. **J. Carvell**, E. Ayieta, A. Gavrin, R. Cheng, V.R. Shah, and P. Sokol, "Magnetic properties of iron nanoparticles" J. Appl. Phys. **107**, 103913 (2010).

6. E. Ayieta, **J. Carvell**, R. Cheng, and Y.B. Losovyj, "Angle resolved photoemission study of surface states on the Pt(997) vicinal surface" Phys. Lett. A **374**, 3080 (2010).

7. **J. Carvell**, E. Ayieta, M. Johnson, and R. Cheng, "Characterization of iron nanoparticles synthesized by high pressure sputtering" Mater. Lett. **63**, 715 (2009).

PRESENTATIONS

1. **"**Induced Spin and Dipole Ordering at Ferroelectric/Ferromagnetic Interface," J. Carvell, R. Cheng, P. A. Dowben, *12th Joint MMM/Intermag Conference,* Chicago, IL. January 2013.

2. "Tuning the Ferroelectric Properties Through a Magnetic Field," **J. Carvell**, R. Cheng, *American Physical Society 2012 March Meeting*, Boston, MA. February 2012.

3. "Ultra-high Vacuum Scanning Tunneling Microscope," **J. Carvell**, S. Carpenter, R. Cheng, *Indiana Microscopy Society Annual Meeting*, Indianapolis, IN. May 2010.

4. "Magnetic Properties of Iron Nanoparticle Films," **J. Carvell**, E. Ayieta, R. Cheng, V.R. Shah, P. Sokol, *IUPUI Research Day*, Indianapolis, IN. April 2009.

5. "Synthesis and characterization of iron nanoparticles by high-pressure sputtering," **J. Carvell**, E. Ayieta, R. Cheng, *American Physical Society 2008 March Meeting*, New Orleans, LA. March 2008.

TEACHING EXPERIENCE

- Physics 219 (Electricity, Magnetism, Optics and Modern Physics, Summer 2010 and Summer 2012)
  - Taught lecture and recitation for second semester introductory physics. Managed class, including preparing homework assignments, preparing exams, and grading for the entire course.
- Physics 201 (Mechanics, Fluids, and Heat, Summer 2011)
  - Taught lecture and recitation for a full class of over 100 students for first semester introductory physics. Managed each lecture, including preparing homework assignments and exams, and grading exams.

- Physics 152 and Physics 251 (Mechanics and Electricity, Magnetism, Optics, and Heat, 2009-2012)
  - Student mentor for calculus based physics recitations. Interacted with students, answered questions, provided guidance on assigned problems, and graded exams.
- Introductory Physics Labs (2006-2012)
  - Lab instructor for every level of introductory physics courses. Responsible for teaching material relevant to each lab, setting up experiments, and interacting with students during laboratory sessions. Graded all lab reports.
- Astronomy 105 (Spring 2007)
  - Graded all assignments and exams for the introductory astronomy course, as well as assisted course instructor whenever needed.
- Physics Tutor (2006-2012)
  - Offered tutoring to students for courses of all levels, up to 400 level, including advanced electricity and magnetism, optics, mechanics, and modern physics.

HONORS AND AWARDS

- Research Investment Fund (RIF) Fellowship (August 2010 – May 2013)
- IUPUI School of Science Physics Department Outstanding Graduate Student (May 2012)
- American Association of Physics Teachers Physics Department Outstanding TA (May 2007 and May 2012)
- GAANN (Graduate Assistance in Areas of National Need) Fellowship (August 2007 – May 2010)
- IUPUI School Of Science Outstanding Teaching Assistant (May 2008)
- IUPUI School Of Science Graduate Student Council Travel Grant (December 2007)
- IUPUI Graduate School Travel Grant (December 2007)
- IUPUI Undergraduate Research Opportunity Program Grant (May 2005)
- Butler University Seitz Award for international research (May 2005)

AFFILIATIONS AND MEMBERSHIPS

American Physical Society (APS)
American Association of Physics Teachers (AAPT)
American Vacuum Society (AVS)
IUPUI School of Science Graduate Student Council
Indiana Academy of Science